UNIVERSITÀ DEGLI STUDI DI MILANO-BICOCCA
Facoltà di Scienze Matematiche, Fisiche e Naturali

Doctorate in Nanostructures and Nanotechnologies

Resonance effects in the Raman analysis of SiGe nanostructures

Doctorate thesis of
Andrea Picco

Supervisor : Dott. Emiliano Bonera
Coordinator of the School: Prof. Gianfranco Pacchioni

Cycle XXIV

Contents

List of abbreviations **iii**

List of symbols **vi**

1 Introduction **1**

2 $Si_{1-x}Ge_x$ nanostructures **6**

2.1 $Si_{1-x}Ge_x$: basic properties 6

2.2 SiGe islands and dots 9

2.2.1 Growth mechanism 10

2.2.2 Composition inhomogeneity 17

2.2.3 Spatial ordering 18

2.2.4 Applications 21

3 Characterization techniques **24**

3.1 Electron microscopy (TEM) 25

3.2 Scanning probe microscopy (STM/AFM) 29

3.3 X-Ray diffraction (GID/GISAXS/AXRS) 31

3.4 Photoluminescence 36

3.5 Raman scattering 40

4 Raman efficiency of $Si_{1-x}Ge_x$ **46**

4.1 Theory of the Raman effect 46

4.1.1 Classical description 46

4.1.2 Effect of strain in FCC crystals 48

4.2 Raman efficiency and Raman resonance 49

4.3 Measurement of the Raman efficiency 53
4.3.1 From the theory to the experiment 53
4.3.2 Experiment 56
4.3.3 Experimental details 58
4.3.4 Experimental data and remarks 58
4.3.5 Data elaboration 61
4.4 Results 64
4.4.1 Comparison with the theory 68
4.4.2 Results of the approximated data elaboration 72
4.4.3 Single Raman mode analysis 72
4.5 Raman experiments on inhomogeneous samples 73
4.5.1 Multiwavelength analysis of SiGe islands 74
4.5.2 Strain induced by SiGe islands grown on patterned substrates 78
4.5.3 Strain in the Si cap layer 82

5 Raman analysis of inhomogeneous samples 87
5.1 Spectrum analysis 87
5.2 Composition profiling 89
5.3 Validation of the method 93
5.4 Application to SiGe islands 95
5.4.1 Measurements at 532 nm 95
5.4.2 Measurements at 458 nm 97
5.5 Limitations to the method 99

6 Conclusions 103

Acknowledgements 106

Bibliography 109

List of abbreviations

AFM Atomic Force Microscopy

A.R. Aspect Ratio

AXRS Anomalous X-Ray Scattering

B Barns

BF Bright Field

CCD Charge Coupled Device

CMOS Complementary Metal Oxide Semiconductor

CVD Chemical Vapour Deposition

D Domes

DF Dark Field

DFT Density Functional Theory

D.O.F. Depth Of Focus

EBL Electron Beam Lithography

FEM Finite Element Modelling

FM Frank-van der Merve

GID Grazing Incidence Diffraction

GISAXS Grazing Incidence Small Angle X-Ray Scattering

HAADF High Angle Annular Dark Field

HH Heavy Hole

HR High Resolution

LEPECVD Low Energy Plasma Enhanced Chemical Vapour Deposition

LH Light Hole

MBE Molecular Beam Epitaxy

ML Monolayer

MOSFET Metal Oxide Semiconductor Field Effect Transistor

MP Metastable Pyramids

NA Numerical Aperture

NP No Phonon

P Pyramids

PL Photoluminescence

RS Raman scattering or also Raman shift

SD Super Domes

SEM Scanning Electron Microscopy

SK Stranski-Krastanov

SO Split Off

SP Stable Pyramids

STEM Scanning Transmission Electron Microscopy

STM Scanning Tunneling Microscopy

TB Transition Barns

TEM Transmission Electron Microscopy

TO Transverse Optical (phonon)

UV Ultra Violet

VIS Visible range

VW Volmer-Weber

WL Wetting Layer

XRD X-Ray Diffraction

List of symbols

x SiGe alloy composition

a Lattice parameter

$\varepsilon_{\mu\nu}$ Element of the strain tensor

$\sigma_{k\lambda}$ Element of the stress tensor

$C_{\mu\nu}$ Elastic constant

Δ_0 Split off energy ($k = 0$)

Δ_1 Split off energy (along Λ)

$E_1/E_1 + \Delta_1$ Direct electronic transition. See section 2.1

$E_0/E_0 + \Delta_0$ Direct electronic transition. See section 2.1

E_0' Direct electronic transition. See section 2.1

E_2 Direct electronic transition. See section 2.1

h_c Critical Thickness (for plastic relaxation)

V_c Critical Volume (for island nucleation)

m_e Electron Mass at rest

ξ Phonon normal coordinate

χ Electrical susceptibility

$\mathbf{R}$ Raman tensor

d Element of the Raman tensor

$\mathbf{e}_i$ Polarization vector of the incident light

$\mathbf{e}_s$ Polarization vector of the scattered light

$\varepsilon_{//}$ In plane component of the strain

$\varepsilon_{\perp}$ Out of plane component of the strain

b_i Strain coefficient of SiGe Raman peaks

S Raman efficiency

Ω Collection solid angle

ω_q Phonon frequency

ω_s Scattered light frequency

ω_R Raman shift

$(n+1)$ Bose factor

$\varepsilon(\omega)$ Dielectric function

I_s Scattered intensity

I_0 Incident light intensity

T Trasmissivity

L Light penetration depth

D Sample (or layer) thickness

η Optical equipment efficiency

$d^{\lambda}_{\mu,\nu}$ Deformation potentials

ε^{+} Contribution to the dielectric function given by the $E_1+\Delta_1$ transition

ε^{-} Contribution to the dielectric function given by the E_1 transition

ϕ_x Raman spectra of relaxed SiGe with composition x

I_x Intensity of the Raman signal related to the composition x

a_x Spectral component related to the composition x

Chapter 1

Introduction

It has been known since a long time that the properties of nanostructured materials can be very different from those of the bulk. Quantum confinement, removal or changes in the symmetries of the system, and breaking of conservation rules are examples of the factors which can lead to dramatic modifications in the electronic, optical and mechanical characteristics when the physical dimensions are shrinked in the nanometer range. Not only, it must also be reminded that the reduced dimensions make nanostrustured systems sensitive to effects which are completely negligible (and thus inaccessible) at longer length scale. This can be both an opportunity or an hindrance, depending on which factors we are interested in. In any case, this new accessible world opens a wide range of new degrees of freedom in the investigation and application of fundamental physical phenomena by means of nanostructures.

The effects arising in nanostructured materials have been subject of theoretical studies since the beginning of quantum mechanics: very simple quantum mechanical models can be used to outline the behaviour of particles confined in a space with size in the nanometer length scale, starting from the didactic particle-in-a-box, and going up to more complicated potentials. Now, with the development of the growth and fabrication techniques, the simple systems which appeared just as academic simplifications can be realized in practice, with the possibility of creating artificial potentials: this enables us to confine the carriers in a controlled way, and possibly to exploit and tailor the new properties given by the nanometer scale miniaturization. This is nanotechnology.

In addition to the increased sensitivity to the tiniest physical interactions, nanostructures provide systems in which also the coupling between these interactions becomes stronger: this explains the interest in using nanostructures both for fundamental studies and possible new applications. But first of all, this explains the intrinsic multidisciplinary character of nanotechnology, in which knowledge is gathered from many different branches of science and put together in order to build, understand and engineer the properties of the system.

Semiconductor nanostructures in particular have gained increasing attention in the last decades: in addition to the general considerations given above, semiconductors (and especially silicon) are among the most studied materials, both from the fundamental and applicative point of view. The opportunity of taking advantage of the deep knowledge of the materials and the maturity of the fabrication technology explains the fast development of this branch of nanotechnology. In this thesis, we concentrate in particular on group IV semiconductors, and in particular Si, Ge and their alloy, $Si_{1-x}Ge_x$.

$Si_{1-x}Ge_x$ is a solid solution of Si and Ge: the atomic sites of a diamond crystalline structure, typical of both Si and Ge, are filled randomly by the atoms of the two elements, with the proportion specified by the Ge molar fraction x. Si and Ge are completely miscible: this means that the Ge molar fraction (also called Ge content, or alloy composition) can vary continuously between the values 0 (pure Si) and 1 (pure Ge). The key value of $Si_{1-x}Ge_x$ is that its structural, electronic and optical properties vary continuously with the composition, and are also affected by strain: these features bring additional degrees of freedom in the engineering of nanostructures. From the applicative point of view, the well known compatibility of $Si_{1-x}Ge_x$ with CMOS technology has naturally oriented the perspective of researchers towards a possible integration in microelectronics of devices based on $Si_{1-x}Ge_x$ nanostructures.

Nowadays, the fabrication of integrated circuits in microelectronics has a matter of fact already reached a point which fully stands within the domain of nanotechnology, with dimensions of the transistors lying in the range of few tens of nanometers. New concepts are elaborated and materials are introduced and optimized in the attempt to overcome or at least compensate the physical limitations due to the extreme miniaturization of the devices, which emerge more and more severely. Strain engineering, for example, is a well established building block for

the miniaturization of CMOS devices, and $Si_{1-x}Ge_x$ was already introduced many years ago for the fabrication of stressor structures. However, more ambitious objectives in the field of $Si_{1-x}Ge_x$ integrated structures in CMOS technology have been defined and pursued by researchers in the last decades: silicon based optoelectronics is one of these. Nanostructuring has been seen as a possible way to overcome the well known deficiency of the silicon emitting performances, mainly due to its indirect bandgap; $Si_{1-x}Ge_x$ based optoelectronic devices, like optical modulators [1], quantum well infrared photodetectors [2] and quantum cascade lasers [3] have been already demostrated. In more futuristic visions, spintronics and quantum computing by means of $Si_{1-x}Ge_x$ nanostructures are under investigation.

One advantage of $Si_{1-x}Ge_x$ nanostructures lies in the characteristic tendency to form self assembled aggregates during heteroepitaxy, driven mainly by the attempt of relaxing the elastic energy originated from the lattice mismatch. The impact on the applications is given by the fact that a bottom up approach for the fabrication of these structures seems to be possible. Many efforts were payed in the recent past in order to control this process and obtain nanostructures with uniform and tuned properties. Knowledge and comprehension of the mechanisms regulating the growth and influencing the internal properties of the structures have been deepened through a systematic study of the growth process under the variation of deposition techniques, experimental parameters, and substrates. Theoretical models and simulations have been developed in order to understand, reproduce and predict the behaviour of the nanostructures, in their structural, electronic and optical features. Last, but not least, several experimental techniques have been applied, optimized or even created in order to allow for the characterization of the structures.

Raman spectroscopy has been successfully applied to the characterization of semiconductors: in the case of pure Si, for example, it represents a unique tool for the characterization of stress in microelectronic devices. Stresses induced by oxide and nitride layers and strips, thermal processes, thermal mismatched materials, bonding, Through Silicon Vias (TSV) fabrication, etc. can be measured with sensitivity of few tens of MPa. In the case of $Si_{1-x}Ge_x$, Raman spectroscopy has been optimized in order to give a valid way to measure both the composition and the strain in the alloy. The method, originally conceived for the analysis of bulk

$Si_{1-x}Ge_x$ or heterostructures, has been extended also to the study of $Si_{1-x}Ge_x$ systems with low dimensions. This has made Raman spectroscopy a wide used tool in $Si_{1-x}Ge_x$ nanotechnology for a fast and non destructive characterization of the structures.

One of the most known and useful features of Raman spectroscopy of semiconductors is that the surface sensivity can be tuned by varying the excitation wavelength. Excitation light at higher energy is more strongly absorbed by the material: as a consequence, the depth of the illuminated volume (which is in fact the probed portion of the sample) is reduced. In the case of $Si_{1-x}Ge_x$, due to the dependence of the bands on the alloy composition, the absorption coefficients depends strongly also on x. Several examples of Raman experiments performed at different excitation light wavelengths on $Si_{1-x}Ge_x$ micro- and nanostructured systems can be found in the literature, but the effect of the variation in the absorption coefficients is always rather qualitative. Moreover, another important energy and alloy composition dependent parameter is represented by the Raman efficiency of $Si_{1-x}Ge_x$, which is expected to show resonances in corrispondence of the direct transitions in the material, in analogy with the well known cases of pure Si and Ge. Also this point, though already known in principle, is always treated in a qualitative way due to the absence in the literature of a systematic study of the $Si_{1-x}Ge_x$ Raman cross section as a function of both the alloy composition and the excitation light energy.

In this work, this systematic study will be presented. The resonant Raman effect in $Si_{1-x}Ge_x$ will be experimentally characterized and quantified, and the results will be discussed with reference to the theory. The impact of the resonance effects on several Raman experiments performed on $Si_{1-x}Ge_x$ nanostructures will be discussed with some examples.

Another point which is often only partially discussed in the literature is the effect of compositional distributions. As will be presented in the introductory chapter, substantial composition inhomogeity can be found in $Si_{1-x}Ge_x$ nanostructures, and in particular in self assembled ones, due to intermixing between Ge and Si coming from the substrate or the matrix surrounding the structures. Intermixing leads to the broadening of the bands in the Raman spectrum of the sample: this is generally attributed to "compositional disorder", and only average information about the nanostructures is usually extracted from the Raman spectra. In this

thesis, however, we want to go beyond and extract information about the composition distribution within the nanostructures by means of a quantitative analysis of the broadening of the peaks, with the aid of the knowledge of the $Si_{1-x}Ge_x$ Raman cross section previously measured. Hence, a novel approach for the analysis of Raman spectra of compositionally inhomogeneous $Si_{1-x}Ge_x$ samples will be presented, with the possibility (under several condition) of estimating the composition profile of $Si_{1-x}Ge_x$ nanostructures by means of a single Raman spectrum. Several case studies will be presented and the results will be compared to those obtained by means of other well established techniques.

In this thesis, a brief general introduction to $Si_{1-x}Ge_x$ nanostructures will be given in the first chapter: in particular, the case of self assembled $Si_{1-x}Ge_x$ islands will be treated. The growth mechanisms will be explained, and the mainstreams in the growth research will be outlined. The intermixing processes occurring during the growth, and influencing the electronic and optical properties of the nanostructures, will be addressed. Finally, some examples of applications of $Si_{1-x}Ge_x$ dots and islands in microelectronics and optoelectronics will be shown.

Chapter 3 will introduce the reader to several of the most used techniques for the characterization of $Si_{1-x}Ge_x$ islands. Raman spectroscopy will be presented as well.

In chapter 4, the resonant Raman effect in $Si_{1-x}Ge_x$ will be studied. After a brief theoretical introduction to the Raman effect and the origin of Raman resonance in $Si_{1-x}Ge_x$ alloys, the experiment will be presented, and the data elaboration will be treated in detail. The experimental results will be shown and compared to the results of a semiempirical calculation of the Raman cross section. Then, several Raman experiments performed with different illumination conditions on $Si_{1-x}Ge_x$ islands will be presented and discussed on the basis of the knowledge of the Raman resonance effects.

Chapter 5 will be dedicated to the explanation of the methodology for the analysis of the Raman spectra of compositionally inhomogeneous $Si_{1-x}Ge_x$ samples, and the determination of the internal composition profile. The method will be validated on a test sample and applied again to the study of $Si_{1-x}Ge_x$ islands.

Chapter 2

$\mathrm{Si_{1-x}Ge_x}$ nanostructures

2.1 $\mathrm{Si_{1-x}Ge_x}$: basic properties

$\mathrm{Si_{1-x}Ge_x}$ alloy consists of a random distribution of Si and Ge atoms on the sites of a diamond crystalline lattice, with an occupation probability specified by the relative molar fraction (x for Ge, $1-x$ for Si, where x, the Ge molar fraction, is also referred to as Ge content or alloy composition). The cubic cell is filled by 8 atoms: each atom is placed in the center of a tetrahedron formed by its 4 first neighbors atoms. The next nearest neighbors are twelve. The lattice parameter $a_{Si_{1-x}Ge_x}$ of the bulk (without deformation) material depends on the alloy composition x, and varies almost linearly [4] from the lattice parameter of Si (x=0) to that of Ge (x=1), which is 4.17% larger. The relationship between the alloy composition and the lattice parameter is given by the following relation, with accuracy to about 10^{-4} [1, 5, 6]:

$$a_{Si_{1-x}Ge_x} = 0.54310 + 0.01992x - 0.002733x^2 \tag{2.1}$$

Under the effect of an applied stress, the cubic cell is distorted: the lattice deformation is described by the strain tensor $\varepsilon_{\mu\nu}$ defined as:

$$\varepsilon_{\mu\nu} = \frac{1}{2}\left(\frac{\partial u_\mu}{\partial x_\nu} + \frac{\partial u_\nu}{\partial x_\mu}\right) \tag{2.2}$$

The relationship between the stress tensor $\sigma_{k\lambda}$ and the strain tensor is given by the generalized Hooke's law [7, 8]:

$$\sigma_{k\lambda} = c_{k\lambda\mu\nu}\varepsilon_{\mu\nu} \tag{2.3}$$

where the stiffness tensor $c_{k\lambda\mu\nu}$ can be described by only three distinct non-zero components (elastic constants), usually referred to as C_{11}, C_{12} and C_{44}: the complete form of the tensor is obtained by means of symmetry considerations [7]. In $Si_{1-x}Ge_x$, the elastic constants depend on the composition through the following relations (at the temperature of 300 K) [9]:

$$C_{11}(x) = 165.8 - 37.3x \quad \text{GPa} \tag{2.4}$$

$$C_{12}(x) = 63.9 - 15.6x \quad \text{GPa} \tag{2.5}$$

$$C_{44}(x) = 79.6 - 12.8x \quad \text{GPa} \tag{2.6}$$

Also the band structure of $Si_{1-x}Ge_x$ depends on the alloy composition, with a continuous variation from the band structure of Si to that of Ge. In both Si and Ge, the valence band edge ($k = 0$, Γ'_{25} symmetry) is given by two degenerate light hole (LH) and heavy hole (HH) bands plus another split-off (SO) band which is lower in energy by an amout Δ_0 (split-off energy), depending on x through the relation [10]:

$$\Delta_0(x) = 0.044 + 0.254x[eV] \tag{2.7}$$

In Si, the conduction band minima are sixfold degenerate, and they are found along the [100] directions close to the X points in the Brillouin zone; in Ge, the conduction minima are eightfold degenerate, and they are located at the L points in the Brillouin zone, along the [111] directions. Therefore the fundamental gap in both Si and Ge is indirect, and this is the major limiting factor to the emission properties of group IV semiconductors with respect to the direct gap materials of the III-V group. In $Si_{1-x}Ge_x$, the energy gap is also indirect, and it changes with the alloy composition, with a discontinuity in correspondence of the crossover from the silicon-like to the germanium-like band structure, which occurs at $x \approx 0.85$ (see figure 2.1). The relationship between the x and the energy gap in $Si_{1-x}Ge_x$ can be written as [12]:

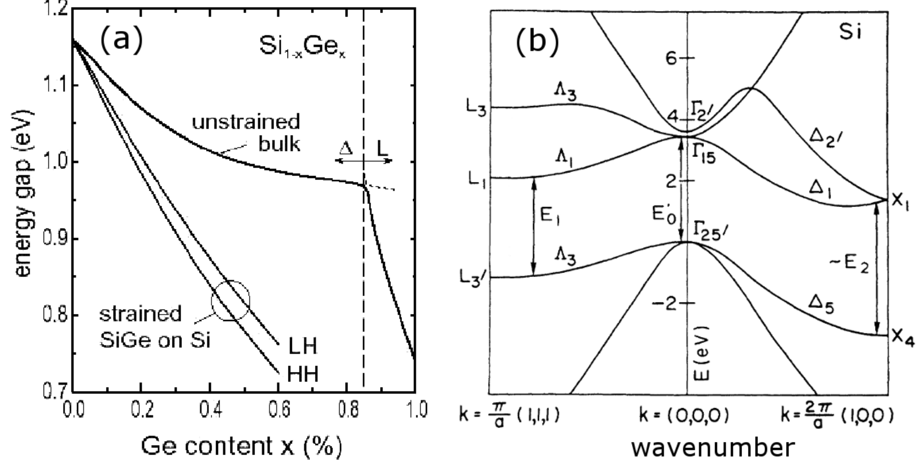

Figure 2.1: Panel (a): energy gap of $Si_{1-x}Ge_x$ as a function of the composition x, for the relaxed material and the alloy grown pseudomorphically on Si. From [11]. Panel (b): band structure of Si. The direct transitions E_1, E_0' and E_2 are shown in the diagram.

$$E_{gap}(x)[\text{eV}] = \begin{cases} 1.17 - 0.43x + 0.206x^2 & E_g^{(\Delta)}(x) \quad \text{for } x < 0.85 \\ 2.010 - 1.27x & E_g^{(L)}(x) \quad \text{for } x > 0.85 \end{cases} \tag{2.8}$$

Also the energy of the direct electronic transitions varies linearly with the composition. The transitions are defined in the following [13, 14] (also see panel (b) in figure 2.1):

$$\begin{cases} E_0/E_0+\Delta_0 & \Gamma_{25'} \to \Gamma_{2'} \\ E_0' & \Gamma_{25'} \to \Gamma_{15} \\ E_1/E_1+\Delta_1 & \Lambda_3 \to \Lambda_1 \ \left(\text{in the range } \frac{2\pi}{a}[\frac{1}{4}\,\frac{1}{4}\,\frac{1}{4}] \to \frac{2\pi}{a}[\frac{1}{2}\,\frac{1}{2}\,\frac{1}{2}]\right) \\ E_2 & \begin{cases} k = \frac{2\pi}{a}[\frac{1}{10}\,\frac{1}{10}\,\frac{9}{10}] \text{ in Si} \\ k = \frac{2\pi}{a}[\frac{3}{4}\,\frac{1}{4}\,\frac{1}{4}] \text{ in Ge} \end{cases} \end{cases} \tag{2.9}$$

where Δ_0 is the split-off energy and a is the lattice parameter. As will be shown, the direct electronic transitions play a crucial role in the origin of the Raman resonance: therefore, their behaviour with respect to the alloy composition will be analyzed in detail in chapter 4. We just list in the following the relations $E(x)$ for the E_0 and the $E_1/E_1+\Delta_1$ electronic transitions [6, 15]:

$$E_0 = 4.185 - 3.296x \quad [\text{eV}] \tag{2.10}$$

$$E_1 = 3.395 - 1.440x + 0.153x^2 \quad [\text{eV}] \tag{2.11}$$

$$E_1 + \Delta_1 = 3.428 - 1.294x + 0.062x^2 \quad [\text{eV}] \tag{2.12}$$

Finally, as can be seen in figure 2.1, also strain influences the band structure of $Si_{1-x}Ge_x$: in particular, the curves reported in figure 2.1 display the bandgap value in a $Si_{1-x}Ge_x$ alloy grown pseudomorphically on Si (i.e. mantaining the in-plane Si lattice parameter). The strain lowers the bandgap value and splits the light hole and heavy hole bands (due to the lowered symmetry of the deformed crystal). For small values of the strain, the band edges are proportional to the strain through linear coefficients called deformation potentials [16, 17]. For Si and Ge, the deformation potentials have been widely studied. In $Si_{1-x}Ge_x$, in principle, the deformation potentials depend again on the alloy composition; however, it seems from the literature that no relations have been determined for these quantities. Very few data are available in the literature, mostly as results of theoretical calculations [18].

2.2 SiGe islands and dots

The formation during heteroepitaxy of self-assembled 3D structures on the surface of the sample has been known for a long time: originally conceived as a detrimental effect on the quality of surfaces and interfaces in the fabrication of quantum wells, it was gradually accepted as a possible way to fabricate 3D $Si_{1-x}Ge_x$ nanostructures on Si. The detailed experimental and theoretical investigation of the assembling mechanisms have turned the surface roughening of the sample surface from a completely random and undesirable hindrance to high quality heteroepitaxy to a well understood and controllable growth process: also spatial ordering and narrow statistical distribution of the structural parameters of the structures have been obtained by means of substrate patterning. The growth mechanism of $Si_{1-x}Ge_x$ islands and dots will be now presented in its basic features. Remarks about the modellization of the growth will be given here, while the experimental aspects of the structure characterization will be treated in the next chapter.

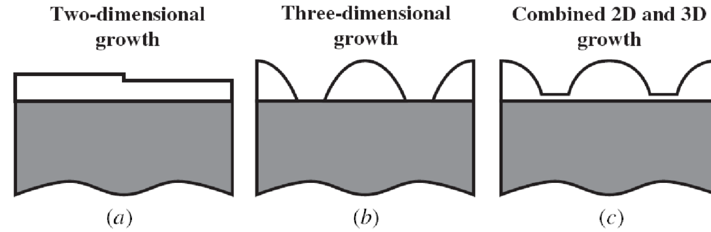

Figure 2.2: Growth modes in heteroepitaxy. Panel (a): Volmer-Weber; panel (b): Frank-van der Merve; (c): Stranski-Krastanov.

2.2.1 Growth mechanism

The possible growth modalities defined by the thermodynamic theory of heteroepitaxy are three (figure 2.2) [19]: in the so called Volmer-Weber (VW) process (a), the growth occurs layer by layer; in the Frank-van der Merve (FM) process (b), three dimensional islands are nucleated directly on the substrate surface; in the Stranski-Krastanov (SK) growth (c), a thin highly strained flat layer covers the substrate surface (wetting layer), up to a thickness of few monolayers, then 3D islands are formed on top of it. The driving forces of the growth are the internal energy of the epilayer (mainly represented by its elastic energy), the surface energy of the epilayer and the epilayer/substrate interface energy.

For values of the composition mismatch beyond 0.1, the self assembling of $Si_{1-x}Ge_x$ nanostructures on Si occurs through the Stranski-Krastanov process, due to a combined effect of the lattice mismatch and the small SiGe/Si interface energy [16]. In the first stages of the growth, it is energetically convenient for the epitaxial (wetting) layer to assume in the growth plane the same lattice parameter of the underlying material (pseudomorphic growth): as the WL thickness increases, the surface energy of the sample is lowered from the Si(001) surface energy to the Ge(001) surface energy. In the meantime, due to the lattice mismatch, the growing crystal accumulates elastic energy, which is proportional to the crystal volume and quadratic in the strain. As the epilayer thickness increases, mechanisms of lattice relaxation are activated in order to release the elastic energy. This is achieved by means of competing plastic and elastic relaxation processes.

In the first case, misfit dislocations are nucleated at the substrate/layer interface, locally restoring the natural lattice parameter of the bulk in the epilayer. This occurs when the epilayer thickness grows beyond a certain value, known as criti-

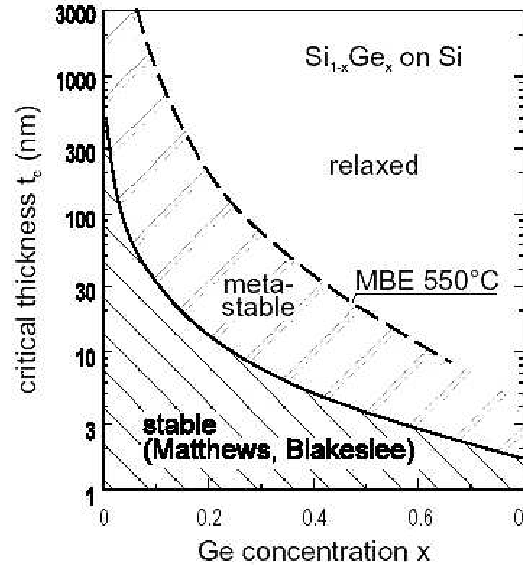

Figure 2.3: Plot of the critical thickness for $Si_{1-x}Ge_x$ layers grown pseudomorphically on Si. From [11].

cal thickness h_c. Many works were devoted to the modellization and calculation of this critical value [20, 21, 22, 23]. As a general result, h_c is found to be inversely proportional to the misfit strain in the epilayer: in the case of $Si_{1-x}Ge_x$ on Si, this means that the critical thickness is inversely proportional to the composition of the $Si_{1-x}Ge_x$ layer, since the lattice mismatch is linear in the alloy composition: this is illustrated in figure 2.3, where the solid curve describes the behaviour of h_c according to the calculations by Matthews and Blakeslee [20, 22]. Above the critical thickness curve a region of metastability is found, in which pseudomorphically grown films can be realized under particular growth conditions [24]. However, they are unstable and nucleate dislocations when subject to post growth annealing [25, 26].

In the Stranski-Krastanov growth, the plastic relaxation is preceeded by elastic mechanisms of strain relaxation: the formation of coherent (i.e. without dislocations) strained 3D islands is part of these processes. The first mechanisms, which occurs in the very first stages of the growth, is represented by the change in the surface reconstruction of Si. On the Si(001) surface, a 2x1 reconstruction is observed: with reference to figure 2.4, the topmost atoms are displaced from the position they usually assume in the bulk, in order to form dimers aligned to the

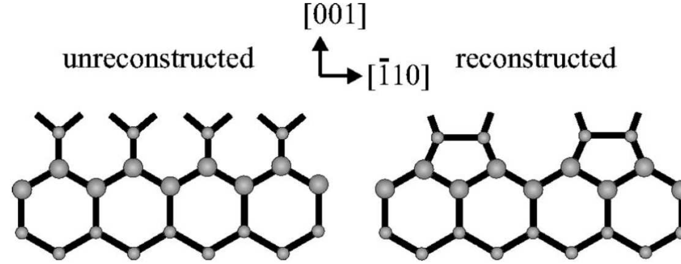

Figure 2.4: Scheme of the 2x1 reconstruction of a Si(001) surface. The topmost atoms share one of their dangling bonds in order to form a dimer aligned along the [1$\bar{1}$0] direction.

[$\bar{1}$10] direction. The formation of the dimer bond, though involving a local distortion of the lattice with respect to the bulk configuration, is actually favourable with respect to having two more dangling bonds at the surface. The dimers form lines parallel to the [110] direction. Real substrate surfaces, in practice, are not perfectly flat (i.e. they do not coincide perfectly with a crystallographic plane), due to a finite misorientation called angle of miscut; as a consequence, the surface of a real substrate is formed by a sequence of atomically flat terraces with monolayer steps: the dimer lines belonging to one terrace are perpendicular to those of the adjacent terraces.

When Ge is deposited on a 2x1 reconstructed Si(001) surface, the Ge atoms are incorporated in the Si surface by means of the formation of buckled dimers [27]; as the coverage increases, the WL surface switches to a periodic 2xN reconstruction, in which every N-th dimer line is missing. The period N of the reconstruction decreases with the Ge coverage [28]. Up to 2 MLs of Ge coverage, a periodical interruption of the dimer lines also appears, leading to a MxN reconstruction in which the wetting layer surface is given by a 2D distribution of rectangular patches.

Beyond 2 ML Ge coverage, 3D island formation becomes favourable with respect to WL thickening. Experimentally, shallow mounds (also referred to as prepyramids) appear first [29, 30] as direct evolution of the patches on the surface. Shallow mounds are characterized by an aspect ratio (defined as the ratio between the island height and the square root of the base area) below 0.1. As the Ge coverage increases, the mounds evolve into square based pyramids or rect-

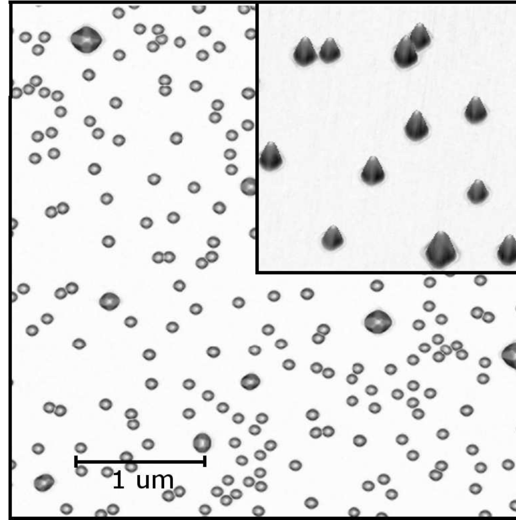

Figure 2.5: AFM image of $Si_{1-x}Ge_x$ islands grown on a flat Si substrate. Islands with different size and shape can be observed.

angular huts, with side walls oriented along the (105) crystallographic directions [31]; rectangular huts, in particular, are obtained at low temperature. The aspect ratio (A.R.) of the pyramids is equal to 0.1. Then, as the growth proceeds, a transition is observed beyond a critical value of the volume from the pyramidal shape to a multifaceted dome shape [32, 33, 34], characterized by the presence of (105),(113) and (15 3 23) facets, with a (001) top facet: the steeper facets lead to an higher value of the aspect ratio, between 0.22 and 0.26. Photoluminescence measurements (see section 3.4) interestingly demostrate that the material needed for the formation of the islands is not taken only from the incoming atoms on the substrate surface, but is also provided by a thinning of the WL. The surface of domes undergoes a further transformation with the Ge coverage, leading to the shape transition to even steeper barns [35], with A.R. in the range 0.26-0.32. If the deposition of Ge is carried on, the accumulation of material of the islands make plastic relaxation favourable, and dislocations are injected in the islands body: the islands become large dislocated superdomes [36, 37, 38], still exhibiting side walls aligned along crystallographic facets, but with a more irregular shape.

It must be pointed out that the shape transitions between the different island configurations (pyramids, domes, barns and superdomes) are usually not collective, and islands with different shapes can be observed at the same time on the

surface of the sample, leading to multimodal distribution of the size [34]. On flat surfaces, the nucleation is a random process, and therefore there is no spatial ordering of the structures on the substrate surface (see figure 2.5). The islands interfere one with each other: they exchange material (usually advantaging larger islands with respect to smaller ones) and they are repelled one from each other by the strain fields surrounding their base [39].

The mechanisms through which the islands are able to release part of the stress in the epitaxial system are mainly three. The first is a redistribution of the stress between the island and the substrate: the island sides pulls the substrate, inducing a compressive strain around the island base [40]. The stress into the island is then partially transferred to the substrate. The second mechanism is the elastic relaxation of the lattice at the island top [41], where the material is more free to expand: this process is more and more effective as the island aspect ratio increases. The last relaxation mechanism, namely intermixing, is strongly dependent on the growth conditions: Si atoms from the substrate surface are expelled from the area at the perimeter of the island base, and diffuse into the structures [42]. The alloying of Ge with Si, corresponding to a decrease in the lattice parameter of the material in the islands, is able to reduce the lattice mismatch and hence the strain. The expulsion of material around the island perimeter is facilitated by the high compression exerted by the nanostructure, and it is revealed by the creation of trenches around the islands [43, 44]. The exchange of Si atoms has been found to be limited to the surface and subsurface layers, while the bulk diffusion plays almost no role [45]. As will be seen in more detail, the intermixing process leads to a highly inhomogeneous composition profile in the islands, with average Ge content decreasing with the growth temperature.

The nucleation of islands, though reducing the elastic strain in the system, has a cost in terms of surface energy, i.e. the formation energy of the island facets. The critical point beyond which the 3D growth is favourable with respect to the thickening of the wetting layer is determined by a balance between volume and surface energy terms [46].

The energy difference Δ between the island and the (N+1) wetting layer, N being the number of Ge monolayers, can be written as [40]:

$$\Delta = V\left(\rho_{is} - \rho_t\right) + S\gamma_{is} - A\gamma_{WL} \tag{2.13}$$

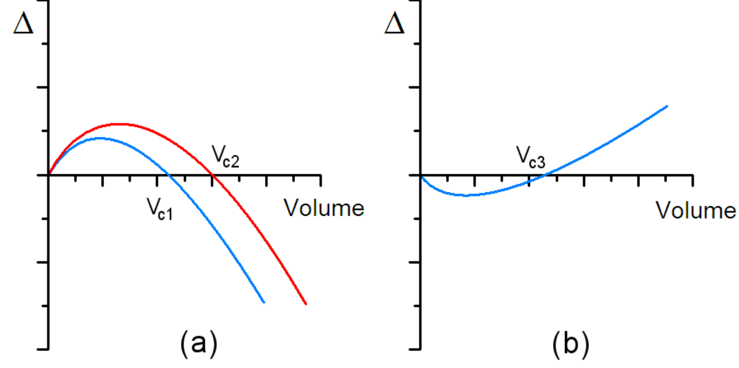

Figure 2.6: Panel (a): plot of the variation with the island volume of the quantity Δ defined in equation 2.13, for a stable island. For volumes larger than a critical value V_c, the growth of the islands is energetically favoured. The red curve corresponds to islands with higher aspect ratio. The critical volume increases with the aspect ratio: $V_{c1} < V_{c2}$. Panel (b): the same plot for unstable islands. The formation of 3D structures is allowed *below* the critical volume V_{c3}.

where ρ_{is} and ρ_t are the elastic energy density in the island and in the wetting layer respectively, V is the volume, S the surface and A the base area of the islands, γ_{is} is the surface energy density of the islands and γ_{WL} the surface energy density of the wetting layer. If $\Delta < 0$ for some values of the volume V, islands are nucleated with that volume. For an island growing without shape changes, $S = sV^{2/3}$ and $A = aV^{2/3}$, with s and a being geometrical parameters depending on the island shape. Therefore the following relation holds:

$$\Delta = DV + EV^{2/3} \tag{2.14}$$

where $D = (\rho_{is} - \rho_t)$ and $E = (s\gamma_{is} - a\gamma_{WL})$.

For large volumes, therefore, the signum of Δ is determined by the signum of D. D is usually negative, due to the capability of the islands to relax the elastic energy; for a positive surface energy term, as it happens if $\gamma_{is} \approx \gamma_{WL}$ the shape of the function $\Delta(V)$ is displayed in figure 2.6, panel (a). The curve shows a maximum, which corresponds to an activation energy for the island nucleation, and a critical value of the volume V_c, defined by the condition $\Delta(V_c) = 0$, beyond which the island formation starts. In panel (a) of figure 2.6, the two plotted curves correspond to facets with different inclination. In particular, the red curve is related to an island with higher aspect ratio [16]. This illustrates that islands with higher

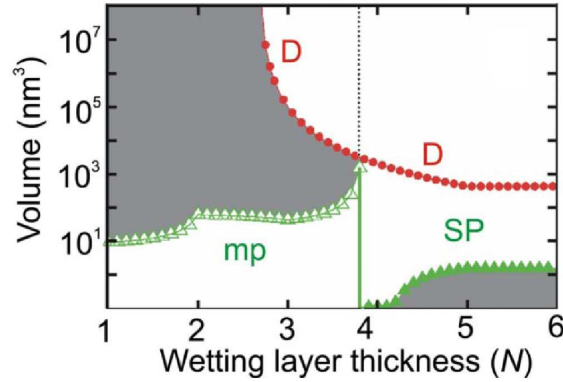

Figure 2.7: Stability diagram for $Si_{1-x}Ge_x$ islands grown on a flat Si substrate, displaying the curves of the critical volume as functions of the Ge coverage. (D: domes; SP: stable pyramids; MP: metastable pyramids). In the gray zones no islands can exist. From [40].

aspect ratio have also higher activation energy and critical volume. This explains the observed sequence of transitions between island shapes with increasing aspect ratio during the growth.

In the evaluation of equation 2.13, the energy density terms ρ and γ must be quantified for both the island and the wetting layer. This is usually achieved by means of theoretical calculations. For the surface energy terms, Density Functional Theory (DFT) is used. The surface energy of the WL can be calculated as a function of both the number N of deposited layers and the strain [47, 48, 49, 50], while the calculations for the crystallographic facets results more demanding due to the difficulty in modelling the strain field at the surface of the islands. Works about the (001), (105) and (113) facets, in particular, can be found in the literature [51, 47, 49, 50].

It must be pointed out that in equation 2.13 the surface energy of the wetting layer γ_{WL}, has been considered independent from N, i.e. the number of Ge monolayers in the WL. This is valid when N is beyond 3 MLs approximately, when the WL surface does not feel anymore the presence of the Si substrate interface. However, for $N < 3$, the surface energy of the WL decreases substantially with N: this changes the energy balance in equation 2.14, allowing the formation of small metastable islands [27]: the typical variation of the energy Δ in this case is plotted in 2.6, panel (b). As the Ge coverage increases, the metastable islands are desta-

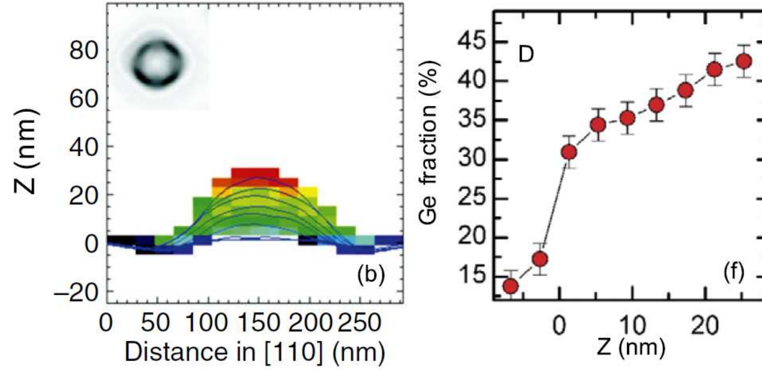

Figure 2.8: Experimental composition in a $Si_{1-x}Ge_x$ island obtained by AFM tomography. From [53].

bilized and dissolve. Small unstable pyramids have been actually observed by Atomic Force Microscopy (AFM) for coverages between 2 and 3.2 Mls [52], with experiments carried out at relatively low temperature (625 °C) in order to increase the lifetime of the metastable structures. A stability diagram resuming the results of the growth model is displayed in figure 2.7[40]: the curves describing the critical volume values of three different kinds of islands (MP: metastable pyramids; SP: stable pyramids; D: domes) are plotted as functions of the Ge coverage.

2.2.2 Composition inhomogeneity

In the above description, only the surface and volume energy contributions have been considered. As it was pointed out previously, however, another strain relaxation channel is given by the Si/Ge intermixing, leading to the formation of inhomogeneous $Si_{1-x}Ge_x$ islands. The incorporation of Si in the island body decreases the elastic energy and thus increases the value of the critical volume for the structure nucleation. Since the internal composition profile determines the shape of the confining potential for the carriers, its characterization is crucial for the applications. This is achieved by a number of different techniques, which will be discussed in the next chapter. In figure 2.8 we show the results given by one of the most sensitive techniques, namely AFM tomography [53] (see section 3.2 for details). The composition profile of a barn shaped island grown at 740 °C is displayed: the Ge content is found to increase toward the top of the island.

Several simulation techniques have been elaborated in order to calculate the

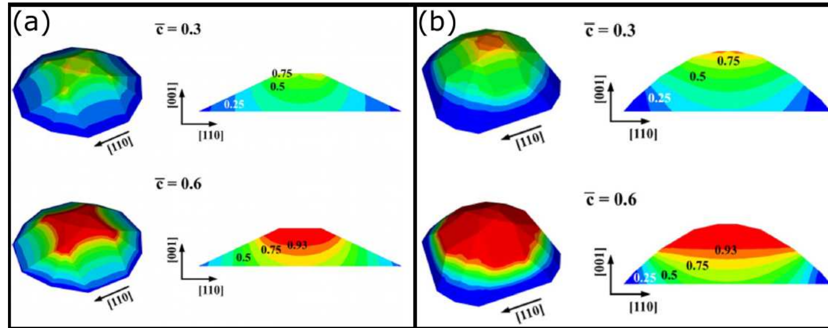

Figure 2.9: Simulation of the composition distribution in a dome (panel (a)) and a barn (panel (b)) shaped islands, for two values of the average composition $\bar{c}$ in the structure. From [54].

internal composition distribution in the islands: this is usually achieved by looking for the composition distribution which is able to minimize the internal free energy, given by the sum of the elastic energy due to the strain, an entropic term, and the Ge/Si enthalpy of mixing, keeping the average composition value in the island as a constraint for the minimization. The different methods give similar results in the prediction of the features of the internal compositional distribution. We show in figure 2.9 the results of the recent Finite Element Model (FEM) simulations elaborated in [54]: the composition profiles in a dome and a barn sahped island with two different values of the average Ge composition are plotted. Ge-richer alloy is correctly found at the top of the island, where the lattice parameter is closer to the bulk value; the Ge content decreases toward the bottom, where strain driven intermixing occurs during the growth.

The results of the simulations are in fair agreement with the experimental characterization of the islands for values of the average composition above 0.4 [55]; for an average composition below 0.4, on the contrary, the agreement is lost: in figure [54], too high values of the composition at the island top are found with respect to the experimental results. This has been attributed to the neglection of the kinetic barriers in the thermodynamic models [40].

2.2.3 Spatial ordering

In the perspective of using $Si_{1-x}Ge_x$ islands for electronic and optoelectronic applications, uniformity of their structural properties and ordered spatial arrange-

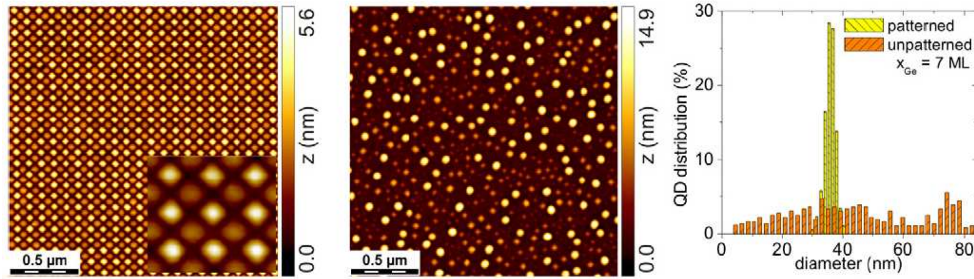

Figure 2.10: AFM images of $Si_{1-x}Ge_x$ islands grown on patterned (left) and flat Si substrates (center). Right: size distribution of the islands grown on the two substrates. From Dais [60].

ment must be achieved. In recent years, substrate patterning has been individuated as a reliable method to better control the growth of $Si_{1-x}Ge_x$ islands and dots. Ordered patterns of pits can be obtained in the Si substrate by lithography [27]; the pits are found to be preferential sites for the island nucleation: actually, in addition to reducing the exposed surface, the growth in the pits allows for a more efficient strain relaxation in the islands [56]. In the first steps of the growth, inverted islands are formed in the pits, with facets defined by the pit walls [57]. It was demonstrated by simulation of the elastic fields that this geometry allows for a higher redistribution of the stress between the inverted island and the substrate. Therefore, the lattice mismatch at the inverted island base is lower than it would be for the growth on a flat substrate. Moreover, the pit geometry also enhances the intermixing of Si and Ge, thus increasing the strain relaxation: it was demonstrated experimentally that lower average composition and smoother composition profiles are present in $Si_{1-x}Ge_x$ islands grown on patterned substrates with respect to those deposited on unpatterned surfaces. As a consequence of the more efficient strain relaxation, the nucleation of dislocations in the islands is delayed, and larger critical values are found for the onset of plastic relaxation [58, 59]. This allows creating coherent islands which are larger and with higher aspect ratio.

The growth on the pits creates a well controlled environment for the nucleation of the islands: the pattern defines separated capture areas for the Ge adatoms, which are attracted to the center of the pits where the chemical potential is minimum [61]. Islands nucleating in different pits do not interfere one with each other: this leads to the suppression of Ostwald ripening, which is a broadening factor for

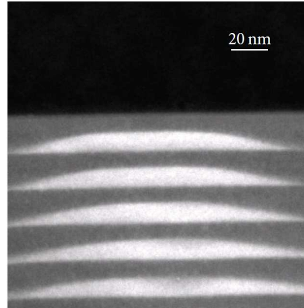

Figure 2.11: TEM image of a self aligned stack of $Si_{1-x}Ge_x$ islands with Si spacers. The spontaneous growth of one island on top of the other is due to the strain field induced by the structures in the overlaying Si spacer.

the size distribution of $Si_{1-x}Ge_x$ islands grown on flat [61]. Consequently, narrow and monomodal island size distributions are obtained on patterned substrates [60], differently from the flat on which the coexistence of differently shaped islands is observed with broader size dispersion (see figure 2.10). In addition, the composition profile homogeneity is substantially improved. The size, composition and relaxation of the islands can be addressed by varying the geometrical parameters of the pattern (pit size, spacing, depth, shape), the deposition parameters (Ge coverage and temperature), and postgrowth annealing [62].

Accurate vertical ordering of the islands can be also achieved, without any lithographic aligment procedure [16]. Multilayers of $Si_{1-x}Ge_x$ islands can be grown by alternating depositions of Ge and Si, in order to keep the island layers separated by thin Si spacers, whose thickness can reach several tens of nanometers [63]: the $Si_{1-x}Ge_x$ islands tend spontaneously to nucleate aligned to the structures below, as shown in figure 2.11. This is again an effect of the strain field induced in the Si spacer by the buried $Si_{1-x}Ge_x$ islands. The tensily strained Si above the islands exhibits in the growth plane a lattice parameter which is closer to the value of Ge: therefore, the lattice misfit for the Ge atoms being deposited is lower in correspondence of the buried islands. This creates a local minimum of the chemical potential and thus defines preferential sites for the structure nucleation. A dependence of this self aligning behaviour on the Si spacer thickness is observed [63]: for very thick Si layers, the influence of the buried islands is lost and the island nucleation at the top becomes again uncorrelated.

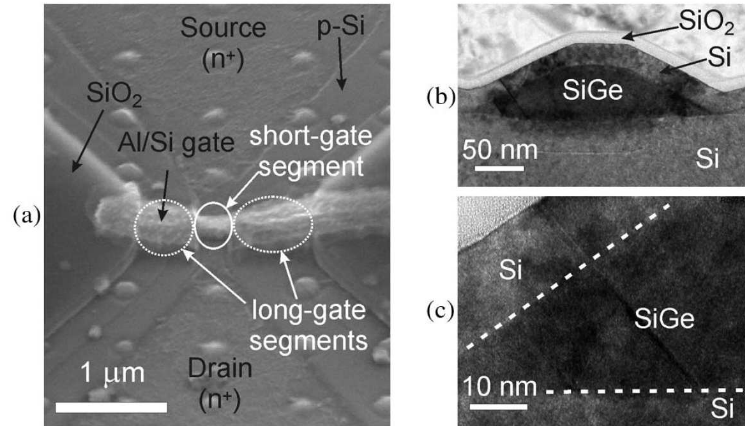

Figure 2.12: Panel (a): SEM image of the dotFET device fabricted in the work of Jovanovic et al. [65]. Panels (c) and (d): TEM details of the thin strained Si channel on the $Si_{1-x}Ge_x$ island stressor.

2.2.4 Applications

Several applications based on the properties of nanostructured $Si_{1-x}Ge_x$ have been proposed: we now report briefly three examples, in which $Si_{1-x}Ge_x$ islands are used as stressors in high mobility MOSFETs, as emitting centers for CMOS compatible optoelectronics, and as phonon barriers for thermoelectric applications. A thorough review can be found in [64].

The mobility of electrons and holes in silicon can be enhanced by means of stress [66]: hence, several solutions have been implemented in microelectronics in order to introduce strain in MOSFET channels [67, 68]. $Si_{1-x}Ge_x$ blocks in the source and drain regions are used to stress the channel compressively [69], while biaxial tensile strain can be achieved through the epitaxial growth of silicon on an embedded $Si_{1-x}Ge_x$ stressor [70, 71]. However, limits exist to the scalability of the structure and the maximum strain achievable in the channel. In order to overcome these limits, self assembled $Si_{1-x}Ge_x$ islands have been proposed as stressors elements both for introducing compressive [72] and tensile [73] strain in the channel. In the latter case, this means that a MOSFET should be built directly on the dots (the so-called dotFET): for this kind of application, the in-plane ordering of the $Si_{1-x}Ge_x$ islands is mandatory. The strain of a thin film of silicon pseudomorphically grown on $Si_{1-x}Ge_x$ islands was simulated [74] and character-

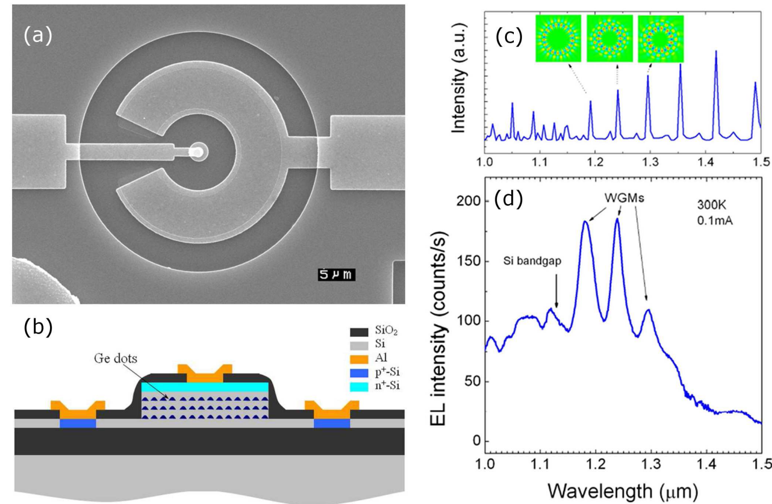

Figure 2.13: Panel (a): SEM image of the optoelectronic device presented in [78]. Panel (b): cross-view scheme of the device. Panels (c) and (d): theoretical and experimental electroluminescence spectra of the device. The narrow emission peaks are due to whispering gallery resonating modes in the cylindric optical cavity. The stationary fields of the resonating modes are shown in the insets.

ized by several techniques including X-Ray diffraction [75], and Raman scattering [76]; the variation of the strain with respect to the Si epilayer thickness was also investigated. As a result, it was found that $Si_{1-x}Ge_x$ islands are able to introduce higher levels of strain in the Si channel with respect to the previous techniques with a delayed nucleation of dislocations. A prototype of dotFET was recently demostrated [65, 77], in which a 100 nm channel MOSFET was fabricated on top of $Si_{1-x}Ge_x$ islands grown on a patterned substrate by Electron Beam Lithography (EBL): in figure 2.12, an image of the device is shown. In order to prevent the diffusion of Ge into the Si channel, all the process steps were kept below 400 °C after the islands formation. The Si epilayer thickness was set at 30 nm, with an maximum expected strain level about 0.7%. The electrical characteristics of the MOSFET were measured, evidencing an enhancement in the mobility up to 22% with respect to the reference devices grown on flat Si. In order to make this process compatible with the CMOS process flow, which includes also high temperature process steps, it has been proposed to remove the $Si_{1-x}Ge_x$ island after the MOSFET formation by selective chemical etch (disposable d-dotFET [77]).

$Si_{1-x}Ge_x$ islands have been used also in optoelectronics, as confining struc-

tures used in order to increase the poor recombination efficiency of silicon. We report here the fabrication of a photodiode in which a $Si_{1-x}Ge_x$ islands multilayer (with $N = 15$) has been embedded in a p-i-n junction [78]. The junctions allows injecting a carrier current through the islands multilayer: the confining potential inside and around the islands due to the tuning of the gap given by the alloy composition and strain brings electron and holes close in the direct space and relaxes the selection rules for momentum conservation. As a result, the radiative emission efficiency is expected to increase. The multilayer is shaped as a microdisk (see figure 2.13), in which resonating whispering gallery modes can be established: this solution is used in order to shape the emission spectrum of the dots, which are grown randomly in each layer. Electroluminescence from this device was actually observed, with emission peaks related to different resonating modes, as evidenced in figure 2.13. References to other solutions for increasing the radiative efficiency in optoelectronic devices through $Si_{1-x}Ge_x$ dots can be found in the same paper.

Multilayers of randomly arranged $Si_{1-x}Ge_x$ dots have been recently demonstrated to represent also efficient structures for stopping phonons in materials: the $Si_{1-x}Ge_x$ island layers act as diffusive barriers for the phonons and prevent their propagation [79]. This results in exceedingly low thermal conductance in stacks of $Si_{1-x}Ge_x$ island layers separated by Si spacers. Not only it was possible to obtain a thermal conductance below the amorphous limit, but also it was demonstrated that the thermal conductance can be precisely tuned by varying the thickness of the Si spacers. In [79], very small hut and pyramids islands were grown randomly on a flat Si surface in order to achieve a high density of nanostructures at the SiGe/Ge interfaces, and increase the scattering efficiency of the barriers. The growth parameters were chosen in order to prevent the formation of dislocations in the structure, which results to be completely crystalline. Even lower thermal conductivity is expected if a SiGe matrix is used instead of Si. These results are particularly interesting for applications in thermoelectricity [80], where the main issue lies in obtaining materials having simultaneously good electrical conductivity and poor thermal conductivity: this allows mantaining a good thermal gradient in the thermoelectric device while allowing carriers flowing easily from the hot to the cold area, thus increasing the thermoelectric figure of merit.

Chapter 3

Characterization techniques

In this chapter we will focus our attention on the experimental characterization of $Si_{1-x}Ge_x$ islands, with a review of the principal techniques used for the study of their physical features. The knowledge of the mechanisms linking the growth parameters to the structural properties (shape, size, internal distribution of alloy composition and strain) allows predicting and tailoring the electronic and optical properties of the sample, according to the desired application. The analysis of these nanostructured systems is achieved through the combination of several complementary methods, each one providing pieces of information about morphology, internal structure, and electronic and optical properties. We will consider in particular electron microscopy, scanning probe microscopy, X-Ray diffraction, and optical techniques such as photoluminescence (PL) and Raman scattering. It must be pointed out, however, that each one of these general categories includes usually a wide series of particular sub-techniques, each one characterized by a particular experimental setup. The description of all the different configurations which have been developed so far is beyond the scope of this work: each technique will be therefore exemplified by few most commonly employed versions. This will be enough to understand which kind of information is accessible, as well as the intrinsic powers and limitations of each technique. Examples of applications will be presented, in particular in the study of the $Si_{1-x}Ge_x$ islands introduced in the first chapter.

3.1 Electron microscopy (TEM)

Electron microscopy is a powerful tool, able to give information about the morphology and the internal structural properties of nanostructures. On the basis of the wave/particle relations given by de Broglie, a characteristic wavelength can be assigned to electrons travelling with kinetic energy E, according to the relation:

$$\lambda_e = \pi\hbar\sqrt{\frac{2}{m_e E}} \tag{3.1}$$

where m_e is the mass of the electron ($511\,\mathrm{keV}/c^2$). Electrons with energy in the order of 10 keV have an associated wavelenght in the order of 0.1 angstroms. This gives an indication of the power of using electrons for the analysis of the sample: in principle, they could probe physical properties and interactions with a resolution beyond the atomic length scale, if the resolution were only diffraction-limited.

In all electron microscopy tools, an electronic beam with well controlled energy E is sent to the sample by means of a so-called electron gun. Electrons are emitted from a thermoionic source; then, they are collected, collimated and accelerated by a sequence of anodes put at increasing levels of voltage. In order to drive, shape and focalize the electronic beam, electrostatic and magnetic fields are used (electron optics). The aberrations related to the electron optics are the limiting factor of the imaging resolution. Another factor which affects the actual resolution of the technique is the strong interaction between the electrons in the beam and the charges in the material, as well as among the electrons in the beam itself. This means that the actual resolution which can be achieved by the electrons is much below the diffraction limit. In order to have atomic resolution, the electrons must be accelerated to energies in the range of several hundreds of keV.

The electron beam interacts with the analysed material through several channels: the electrons can be partially transmitted through the sample, they can be elastically or inestically scattered, or even be subject to diffraction phenomena, due to their wave-like behaviour. A wide variety of tools has been created in order to extract information from the analysis of each one of these scattering mechanisms: each one individuates a different technique within the wide domain of electron microscopy. In particular, for the study of $Si_{1-x}Ge_x$ nanostructures, Transmission Electron Microscopy (TEM) is very commonly used. The diffrac-

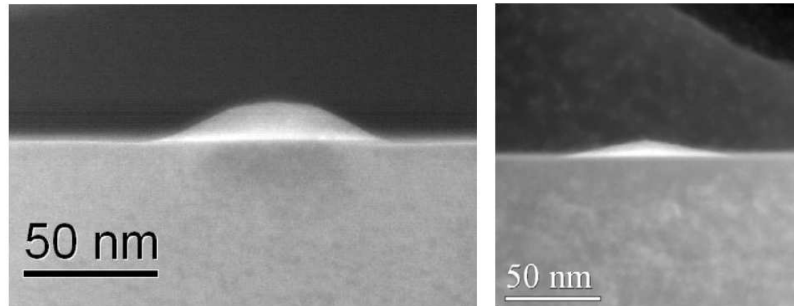

Figure 3.1: HAADF - STEM images of two self assembled SiGe islands grown by SK process on a flat Si substrate. Left: dome shaped island; right; pyramid shaped island.

tion pattern given by the transmitted electrons is propagated and recombined by the electronic optics in a focal plane, in order to reconstruct the image of the sample in the real space. Due to the strong interaction of the electrons with solids, leading to high stopping power, only very thin slabs of material can be analysed. Therefore, the sample must be cut in thin slices, several tens of nm thick, which can be parallel to the substrate surface (top view TEM) or perpedicular to it: in this case, a cross view of the sample is obtained. Conventional TEM is able to provide images with the resolution of several nm, providing information about the structure morphology; in High Resolution TEM (HRTEM), moreover, an accurate correction of the aberrations is able to give images with atomic resolution, which can be digitally elaborated in order to measure locally the lattice parameter and the unit cell distortion. In $Si_{1-x}Ge_x$ nanostructures, changes in the lattice parameter and unit cell symmetry are given by a combined effect of composition and strain. The separation of the two effects needs the support of finite element simulations of the structure; as a result, a mapping of the internal structure can be achieved.

A variation of the technique is given by Scanning Transmission Electron Microscopy (STEM), in which the beam is tightly focused on the slice surface with a spot diameter which can be smaller than 1 angstrom. The beam is driven in order to scan the sample in a rectangular field. The scattering of the transmitted electrons is partially coherent and partially incoherent, due to the fact that the atoms are enlighted at different times and scatter the electrons with random phase. Detectors placed at different angles with respect to the direction of the incident beam are able to detect signals in which the ratio between coherently and incoherently

scattered electrons is different. Bright field (BF), dark field (DF) and High Angle Annular Dark Field (HAADF) images are formed with detectors at increasing angles with respect to the direction of the incident electron beam. In particular, HAADF TEM signal is mostly given by incoherent Rutherford scattering, which is very sensitive to the Z number of the atoms: therefore, in $Si_{1-x}Ge_x$ nanostructures, the constrast is given by the variations in the alloy composition. STEM is able to individuate defects, composition inhomogeneities and discontinuities in $Si_{1-x}Ge_x$ nanostructures.

TEM or STEM characterizations of $Si_{1-x}Ge_x$ nanostructures are very commonly found in the works about $Si_{1-x}Ge_x$ islands; they provide very useful information about the morphology and the interdiffusion of Si and Ge during the growth and the capping of the islands. In figure 3.1, two HAADF-STEM images of one dome shaped island (left) and one pyramid shaped island (right) are shown (from [81]). TEM was used by Rastelli et al. in order to monitor the effect of temperature on the capping of $Si_{1-x}Ge_x$ islands with Si. Figure 3.2 shows one dome shaped island after three capping processes carried out at different values of the Si growth temperature T_S^i: at 300 °C, the TEM image evidences a sharp interface between the cap and the island, demonstrating the absence of intermixing at this temperature. At higher capping temperatures, Si and Ge do intermix and the island dissolves [82].

We report one last example of TEM images, taken from the work by Zhang et al. [83]: in this case, $Si_{1-x}Ge_x$ islands were grown on a pit-patterned Si substrate, and then covered at relatively high temperature (620 °C) by a thin (12 nm) Si spacer; then, another island growth was performed, obtaining a second layer of islands perfectly aligned with the first ones. The authors underline how this process is able to provide coherent islands at higher average composition values with respect to the case of structures directly grown on Si. The TEM image reported in figure 3.3 evidences the sensivity of the technique to the alloy composition: the difference between the Si and the $Si_{1-x}Ge_x$ alloy in the first and second island layer is evident. These structures have been proposed as high strain stressors for the fabrication of high mobility transistors.

TEM techniques, though very powerful for the imaging of nanostructured materials, present the obvious drawback of being destructive; they also require a long time and sophisticated tools for the preparation of the sample, which must be

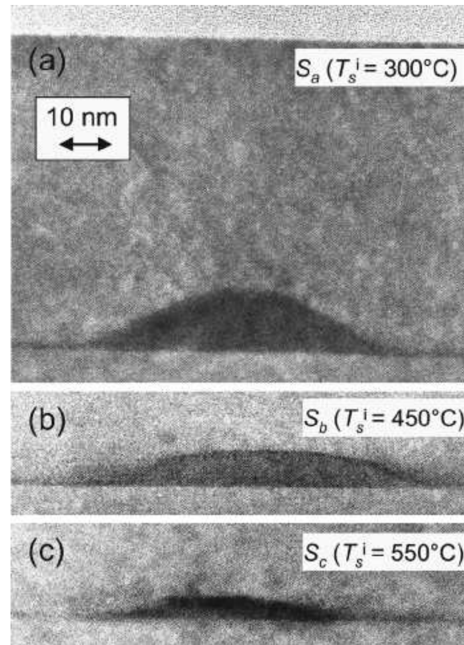

Figure 3.2: TEM images of one island capped with Si at increasing values of the temperature, indicated in the panels. Panel (a): no intermixing occurs; panel (b): partial intermixing modifies the shape of the island; panel (c): the island is mostly completely dissolved in the surrounding Si. From [82].

carefully thinned in order to permit the transmission of the electrons. The thinning process can represent also a perturbation of the sample itself, allowing a partial relaxation of the strain. Finally, TEM is able to give a very accurate description of one single structure, but it lacks the capability of performing statistics on the sample.

Figure 3.3: TEM image of two stacked SiGe islands, from [83].

3.2 Scanning probe microscopy (STM/AFM)

In scanning probe microscopy techniques, a sharp tip with radius in the order of 10 nm is put in the proximity of the sample surface. In Atomic Force Microscopy (AFM) the force acting between the atoms of the surface and the tip is retrieved by measuring the deflection of a cantilever (contact mode), or by monitoring the change in its resonance vibration frequency (tapping mode); in Scanning Tunneling Microscopy (STM), the tunneling current flowing between the sample and the tip is measured. An image of the surface is obtained by moving the tip from point to point, scanning a given area of the sample. Both AFM and STM are able to give an accurate description of the surface morphology. In addition, both techniques are non destructive and do not require any special preparation of the sample. In the study of $Si_{1-x}Ge_x$ islands, AFM images are usually taken after the deposition in order to characterize the shape and size of the grown structures: the capability of AFM of measuring relatively large areas (in the order of 100 μm $\times$ 100 μm) gives the possibility of performing statistic analysis. Its ease of use and speed makes it a routine characterization tool. Several AFM images will be reported throughout this work, and therefore will be not shown here. STM, on the other hand, is able to achieve atomic resolution, and it can also be used in order to perform in situ measurements during the growth: in the case of $Si_{1-x}Ge_x$ islands, STM measurements are able to monitor the evolution of the Ge wetting layer and give useful information about the onset of the structure formation [84]. An interesting STM image is shown in figure 3.4, taken from [82]: a dome shaped $Si_{1-x}Ge_x$ island is imaged before (panel (a)) and after (panel (b)) the growth of a 4 ML Si cap at 300 °C. The STM measurement evidences how the shape of the islands is mostly preserved during the capping at low temperature: this can be correlated to the absence of intermixing observed by means of the TEM measurements reported in the previous section.

It is important to mention a particular application of the AFM technique, implemented by Rastelli et al. in order to study the internal composition profile of the islands. After the growth, the islands are progressively removed by mean of wet etching in a chemical bath in a solution of NH_4OH and H_2O_2. For $Si_{1-x}Ge_x$, the solvent has a characteristic etching rate which strongly depends on the alloy composition [85], while it is independent from the strain. By alternating

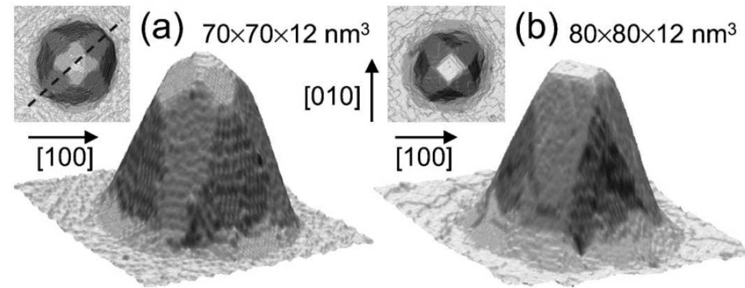

Figure 3.4: STM images of a dome island uncapped (a) and capped (b) with 4 ML of Si grown at 300 °C, as reported in [82]. The shape is almost preserved, meaning that no intermixing occurred. The island facets are mapped with atomic resolution.

etching steps with fixed time and AFM measurements, it is possible to closely monitor the removal of the alloy from the islands. Then, from the relationship between the alloy composition and the etching rate, it is possible to directly obtain a three-dimensional description of the compositional variations inside the structures (AFM tomography). Figure 3.5 shows the result of this kind of analysis on three self assembled islands with different size and shape (D = dome; TB = transition barn; SD = superdome). AFM tomography was applied also to the study islands grown on pit patterned substrates, evidencing the differences with the growth on flat substrates. In general, the growth on patterned substrates leads to more uniform composition profiles in the islands, and increases the average Ge content of the structures [86], [83]; higher uniformity of the size, shape and composition profile is also achieved. Collective shape oscillations between dome and barn configurations were observed for islands growing on patterned substrates [87]: AFM tomography was able to characterize the correlation between the shape change and the modifications in the internal Ge distribution. Deeper information about the islands shown in figure 3.3 was extracted with the same technique [83]. The different behaviour of the WL on flat and patterned substrates was also investigated [88]. The technique is therefore very powerful since it gives 3D information with a thickness resolution in the order of 1 nm; statistic analysis on a large ensemble of structures is possible; the drawback is that it is destructive and quite time requiring.

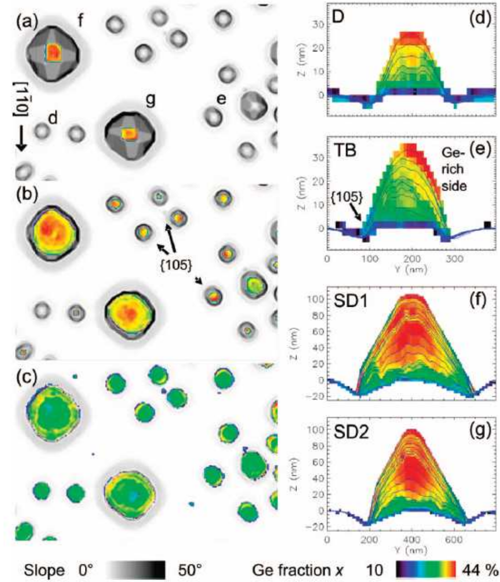

Figure 3.5: Application of AFM tomography (from [53]). 3D compositional profiles for different nanostructures are extracted by measuring the etching rate of the islands, alternating wet etching steps and AFM measurements.

3.3 X-Ray diffraction (GID/GISAXS/AXRS)

X-Ray diffraction (XRD) is diffusely used as a bulk technique, in order to investigate the structure of crystalline materials. However, several techniques based on XRD have been developed in order to allow for the study of surfaces and nanostructures. The surface sensitivity is usually achieved by illuminating the sample with very low incidence angle (grazing incidence). The probing depth can be tuned by varying the incidence angle and the beam energy. X-Ray photons interact quite weakly with matter with respect to other probes, like electrons, which feel strongly the presence of all the charges in the sample. This represents simultaneously a limit and a unique advantage of the technique: on one hand, the signal which carries information about the sample surface is quite weak, and synchrotrons are needed in order to have an intense x-ray illumination; on the other hand, the technique does not influence the growth of the sample, and can be used therefore *in situ*: moreover, it is compatible with any growth environment (gas, vacuum, even liquids), and does not require any particular sample preparation. A very high 3D resolution can be achieved, and quantitative interpretation of the

experiments can be obtained through relatively simple (kinetic) treatment of the scattering process. Differently from electrons, the technique does not suffer from the presence of non-conductive materials in the sample.

Among the several techniques based on X-Ray, we consider in particular three cases, namely Grazing Incidence Diffraction (GID), Grazing Incidence Small Angle X-Ray Scattering (GISAXS), and Anomalous X-Ray Scattering (AXRS) [27]. A combination of the three techniques was able to give a rather complete characterization of the mechanisms occuring during the Stranski-Krastanov growth of $Si_{1-x}Ge_x$ on Si: the modification of the surface reconstruction, the growth of the wetting layer, the onset of the 3D island formation, and the shape change of the structures with increasing Ge coverage can be observed in real time during the growth. Moreover, information about the internal distribution of Ge in the islands can be obtained. Several experiments were carried out in MBE and CVD growth tools coupled to syncrothrons facilities: the limited availability of such special instrumentations represents the major drawback of this experimental approach.

In X-Ray diffraction, no image in the direct space is obtained: the intensity distribution of the scattered radiation is recorded instead in the reciprocal space. We consider a plane wave with wavevector $\mathbf{k}_i$ incident on an ensemble of N scatterer centers located at positions $\mathbf{r}_j$: the intensity of the scattered wave, with wavevector $\mathbf{k}_s$, is given by the following time averaged expression:

$$I = \left\langle \left| \sum_{j=1}^{N} A_j e^{i\left(\mathbf{k}_f - \mathbf{k}_i\right)\cdot \mathbf{r}_j} e^{i\omega t} \right|^2 \right\rangle_t = \left| \int \rho(\mathbf{r}) e^{i\mathbf{Q}\cdot\mathbf{r}} \right|^2 \tag{3.2}$$

where $\mathbf{Q} = \mathbf{k}_f - \mathbf{k}_i$ is the momentum transfer, $\rho(\mathbf{r})$ is the scattering density defined as $\sum A_j \delta\left(\mathbf{r} - \mathbf{r}_j\right)$, and the brackets $\langle\,\rangle_t$ denote the time average. Equation 3.2 shows that the intensity of the scattered radiation is the Fourier transform of the scattering density in real space. With reference to the graphical representation given in figure 3.6 (from [89]), we see that for infinite crystals the density of electrons in the solid can be written as the convolution of the electron density of one atom with the crystal lattice (panels (a) and (b)). From the properties of the Fourier transform, the scattering intensity is given by:

$$I = f_{at}(\mathbf{Q}) \sum e^{i\mathbf{Q}\cdot\mathbf{r}} \tag{3.3}$$

where $f_{at}(\mathbf{Q})$ is the Fourier transform of the atomic electronic density (scattering form factor) and $\mathbf{Q}$ is a vector of the reciprocal space, corresponding to the crystal

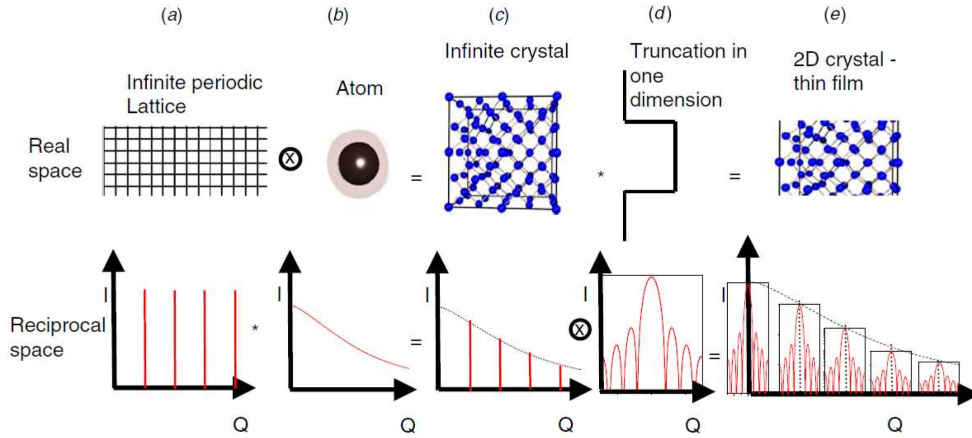

Figure 3.6: Construction in real space (top) and reciprocal space (bottom) of a crystalline thin film. From [89].

lattice described by the coordinate **r**. For thin films and nanostructures, the crystal lattice in real space is truncated at some point: this can be described in real space by the multiplication of a step function which cuts the lattice outside the nanostructure (panel (c), (d) and (f) in figure 3.6). In the reciprocal space, this is equivalent to convoluting the Fourier transform of the infinite lattice with the Fourier transform of the step function.

From the properties of the Fourier transform, the points in the reciprocal space become broadened in k, with a width Δk which is given by:

$$\Delta k \Delta x \approx 1 \tag{3.4}$$

where Δx is the thickness of the thin film in the real space. For a single atomic monolayer ($\Delta x \approx 0$), the points in reciprocal space become infinitely extended (lines, or streaks) in the direction perpendicular to the truncation surface. For a Si(Ge) surface, a portion of the reciprocal space is shown in figure 3.7. Both the points of the reciprocal space corresponding to an infinite crystal and the streaks due to the truncation in the (001) direction are displayed. Morever, additional streaks are reported (red lines) due to the additional symmetry given by the 2x1 reconstruction of the (001) surface of Si(Ge). The points related to Si and Ge are located differently in the reciprocal space due to the different lattice parameter of the two crystals. Strain also modifies the position of the reciprocal space points, by deforming the crystalline unit cell.

Figure 3.7: Illustration of the reciprocal space for a Si(Ge) bulk (solid spheres) and a Si surface (rods). From [89].

In Grazing Incidence X-Ray Diffraction (GID), the intensity of the scattered radiation is mapped along one direction in the reciprocal space. For instance, if the reciprocal space is probed along the (110) direction between (000) and (220) on a 2x1 reconstructed surface, four peaks given by the intersection with the four streaks located in the path will be observed. During the deposition of Ge on Si, the change in the surface reconstruction and the formation of terraces can be monitored by following the modifications of the peaks. The transition to 2xN reconstruction brings additional streaks, while the width of the peaks gives quantitative data about the spatial extension of the terraces. As far as Ge grows pseudomorphically on Si, it keeps the same lattice parameter of the substrate and the (220) peak remains unchanged; when the Stranski-Krastanov 3D growth begins, a partial relaxation of the strain occurs, leading to the broadening of the (220) peak. This can be directly observed during the GID experiments for Ge coverages beyond 4 ML.

In Grazing Incidence Angle Small Angle X-Ray Scattering, the reciprocal space is probed close to the (000) point (forward scattering). Information about the morphology of the nanostructures can be achieved by means of GISAXS during the growth. Streaks perpendicular to the island facets appear, whose orientation can be straightforwrdly obtained; the width of the streaks, moreover, bring information about the size of the facets. Figure 3.8 reports two example of GISAXS

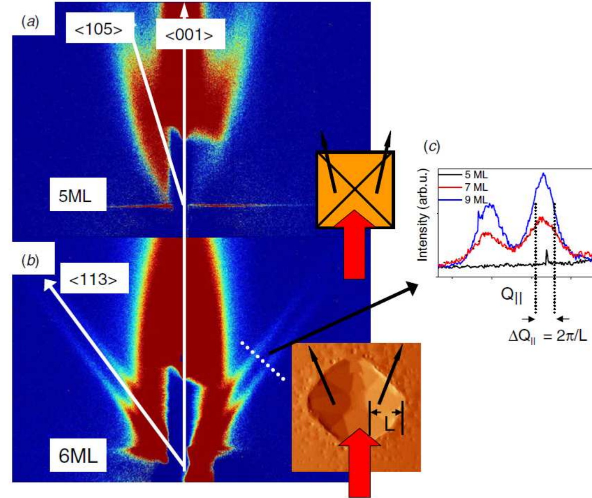

Figure 3.8: Panel (a): the typical GISAXS pattern of pyramid shaped islands; streaks perpendicular to the (105) facets are evidenced. Panel (b): GISAXS measurement of dome islands; in this case the streaks evidence the presence of (113) oriented facets. In the inset (c) a profile of the streak intensity is reported: the size L of the facet can be inferred from the streak width $Q_{//}$. From [89].

measurements taken in the (110) plane at two different stages of the growth of $Si_{1-x}Ge_x$ islands on a (001) Si substrate. In the top panel, two streaks are detected, related to two (105) oriented surfaces, which are known to be characteristic of pyramid shaped islands. As the growth proceeds, other streaks appear, now related to the (113) facets of dome shaped islands. In the figure, the intensity of one streak is plotted in order to obtain its width $\Delta Q_{//}$, which is linked to the size L of the (113) facet through the relation $\Delta Q_{//} = 2\pi/L$.

In Anomalous X-Ray Scattering (AXRS), the chemical dependence of the x-ray atomic scattering factor is exploited in order to obtain information about the Ge content in a $Si_{1-x}Ge_x$ nanostructure. In particular, the energy of the x-ray photons is tuned close to the K absorption edge of Ge (anomalous dispersion): in proximity of the edge, the atomic form factor of Ge $f_{at}(\mathbf{Q})$ depends strongly on the photon energy E:

$$f_{at}(\mathbf{Q}) = f_0(\mathbf{Q}) + f'(E) + if''(E) \tag{3.5}$$

where the two terms $f'(E)$ and $f''(E)$ express the real and imaginary parts of the energy dependent correction due to the absorption given by the core K electrons.

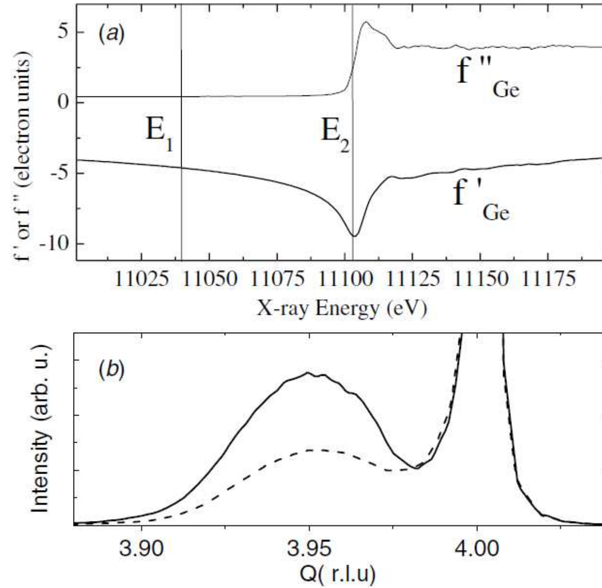

Figure 3.9: Panel (a): X-Ray form factor of Ge in proximity of the *K* absorption edge. Panel (b): intensity of a diffraction curve close to the (400) point in the reciprocal space, for two different energy of the X-Ray beam. From [89].

The two functions are plotted in panel (a) of figure 3.9. As a consequence, a variation of the intensity of the diffraction curves recorded with x-ray energies close to the *K* edge is observed when Ge is present in the sample (panel (b) in figure 3.9). Since Si does not exhibit absorption edges in the same energy range, its scattering power can be considered constant; this means that the change in the diffraction curve intensity in proximity of the absorption edge is only due to Ge. The composition inside the islands can be obtained directly from the ratio of the intensities of two diffraction curves taken at different values of the energy.

3.4 Photoluminescence

In photoluminescence [90], the charge carriers in the sample are excited by the absorption of photons with energy above the gap (typically in the visible and UV range). Electron-hole pairs are created, and the carriers first lose energy by means of scattering with the phonons (thermalization) until they reach a stationary point in the respective bands (a minimum in the conduction band, for electrons; a max-

imum of the valence band, for holes). Then, part of the e-h pairs recombine radiatively, with the emission of a photon. The emitted photon thus brings information about the energy of the transitions between states close to the band edges. Indirect transitions (i.e. requiring the exchange of momentum) can occur with the participation of phonons. Indirect recombination is intrinsically less efficient than direct recombination, since it involves one more particle (three particle process): this explains why indirect gap materials (for instance Si, Ge and $Si_{1-x}Ge_x$) exhibit lower photoluminescence efficiency with respect to direct gap compounds (III-V semiconductiors). Time-resolved photoluminescence experiments investigate the decay with time of the PL signal, after an impulsive excitation: deeper insight in the radiative emission mechanism can be achieved by the individuation of competing radiative processes with different decay time.

Other recombination mechanisms exist which do not involve the creation of a photon (non-radiative recombination): in the case of nanostructures grown on the surface of Si, the most important site of non radiative recombination lies at the surface of the sample. For the study of $Si_{1-x}Ge_x$ nanostructures, therefore, the sample is usually capped with a thin layer of Si in order to reduce the quenching of the photoluminescence due to the surface recombination.

The energy of the bands (and consequently of the PL signal) is affected by several factors: for $Si_{1-x}Ge_x$, the energy of the indirect and direct electronic transitions is strongly dependent on the alloy composition [12, 15]; the indirect band gap is also very sensitive to the strain. In $Si_{1-x}Ge_x$ nanostructures, the effect of quantum confinement must be also considered: in the case of $Si_{1-x}Ge_x$ islands, the holes are confined inside the islands due to the type-II band alignment with Si [91] while the electrons are confined in the tensily strained Si around the islands. The confinement of the carriers in a small volume of the real space corresponds to a higher uncertainty in the k-space, thus increasing the probability of optical transitions without the participation of phonons. As a consequence, the radiative efficiency is increased: this effect has been considered as a possible way to overcome the poor emitting properties of IV type semiconductors, in the perspective of merging Si/Ge/$Si_{1-x}Ge_x$ emitters in the standard CMOS technology, which is fully compatible. The compositional gradients, the shape and the size of the islands determine the carrier confinement, and have a deep impact on the optoelectronic properties of the nanostructures. Therefore, many studies of the link

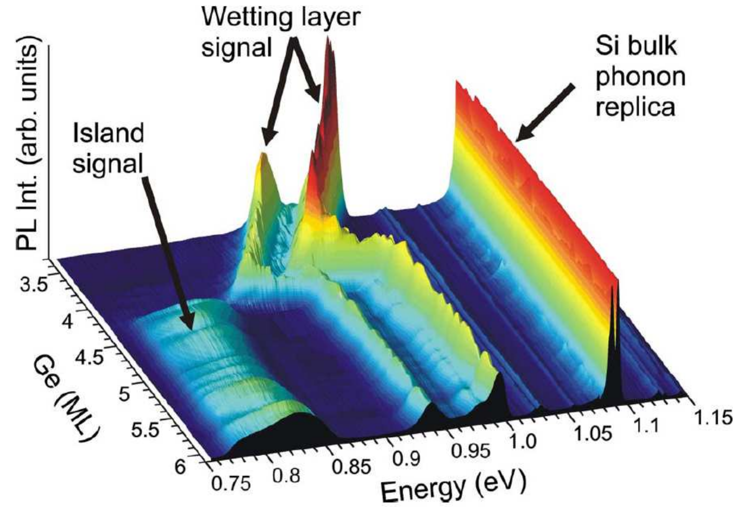

Figure 3.10: Evolution of the PL spectrum of randomly nucleated self assembled $Si_{1-x}Ge_x$ islands grown on a flat Si substrate, as illustrated in [52].

between the structural properties of the islands and their emission features were achieved in the last years.

A very good description of the island nucleation onset can be found in [52], in which the growth of self assembled $Si_{1-x}Ge_x$ island was closely followed by recording PL spectra of the sample at different coverage levels with very high resolution (0.025 MLs). As shown in figure 3.10, in the first steps of the island growth, the PL signal of the WL appears first, with two peaks (the No Phonon (NP) emission and the Transverse Optical (TO) phonon assisted emission) located about 0.1 eV below the Si bulk phonon replica [92, 27]. As the Ge coverage rises, the WL signal redshifts due to the increasing thickness, which lowers the confinement energy. After a critical value of the Ge coverage, which depends on the temperature, the island signal appears as a band between 0.75 and 0.85 eV, while the energy of the WL related band blueshifts in the meantime, which corresponds to the thinning of the wetting layer: this indicates the transfer of material from the WL to the islands. The NP and TO peaks in the island signal cannot be resolved due to the band broadening caused by the dispersion in the composition and size of the randomly nucleated islands [93, 27].

The connection between the island composition and the PL spectrum was investigated by several authors (see [95, 93, 96] and the references therein); as the

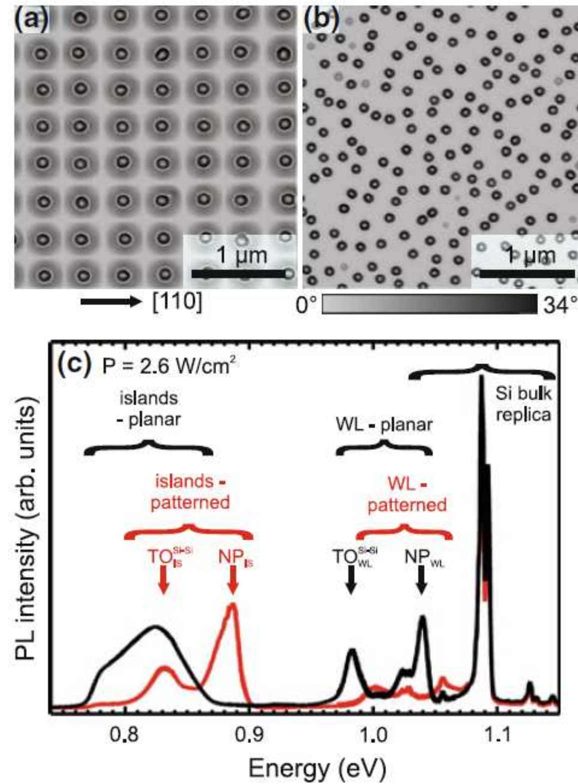

Figure 3.11: From [94]. Panel (a) and (b): AFM images of two $Si_{1-x}Ge_x$ island samples, grown on patterned and flat Si substrate respectively. Panel(c): PL emission of the two samples. Islands grown on pits exhibit two distinct peaks in the PL band (NP and TO transitions); the signal from the WL (in the range 0.85 - 1.05 meV) is lower with respect to the randomly nucleated islands, due to the fact that the material transfer from the WL to the islands is more efficient on the patterned substrate.

average composition in the islands is raised, the energy of the PL band is lowered: this gives the possibility of tailoring the emission energy range of the islands. The effect of the internal inhomogeneity of the Ge content in the islands was investigated, [96, 97], by comparing the experimental PL data to the results of theoretical simulations of the carrier distribution in and around the nanostructures. Effect of capping with Si and intermixing was also studied for various deposition temperatures [98, 93, 99]: coherently with the observations given by other techniques, at high capping temperatures the PL emission efficiency decreases and the broadening increases, due to the partial loss of confinement caused by the intermixing of

Si and Ge at the island boundaries. Tuning of the PL emission position and bandwidth of randomly nucleated islands between two tensily strained Si thin films depending on the Si thickness and temperature was studied in [100] and [101].

The increased uniformity in size, shape and composition achieved by ordered growth of $Si_{1-x}Ge_x$ islands on patterned Si substrate finds correspondence in the emission properties of the islands [102]: a comparison between the PL emission of $Si_{1-x}Ge_x$ islands grown on flat and patterned substrates can be found in figure 3.11: the NP and TO contributions to the photoluminescence emission are substantially sharper for islands grown on patterned substrates with respect to random nucleated islands, so that they can be resolved [60]. The evolution of $Si_{1-x}Ge_x$ islands grown on patterned substrates under variations in the pattern and annealing conditions was studied by means of PL in [103]; the quenching effect of plastic relaxation in the islands was also investigated in [104].

3.5 Raman scattering

In this section some introductory and phenomenological remarks will be given about the Raman effect in SiGe: only the aspects strictly needed to understand the method for the Raman characterisation of $Si_{1-x}Ge_x$ nanostructures will be presented. A more systematic treatment of the Raman effect will be introduced in the next chapter.

The first order Raman spectrum of a SiGe alloy presents three well defined structures, each one related to the vibration of a different pair of first neighbors atoms in the material: Ge-Ge, Si-Ge and Si-Si atom pairs [105, 106]. The three modes are located around 300 cm^{-1}, 400 cm^{-1} and 500 cm^{-1} respectively. The difference in the atom pair reduced mass is the main responsible for the separation in energy of the three bands. Figure 3.12 shows three typical Raman spectra of relaxed SiGe for three different alloy compositions: $x = 0.16$ (top), 0.46 and 0.85 (bottom). The Ge content x (also called composition) of the alloy has a strong influence on the aspect of the Raman spectrum. With x going from 0 (pure Si) to 1 (pure Ge), the Si-Si peak intensity decreases according to the lower number of Si-Si pairs in the material, while the Ge-Ge band rises correspondingly. On the other hand, the Si-Ge band has a symmetrical behaviour, having its relative maximum around $x = 0.5$. An accurate discussion of the intensity ratios of the

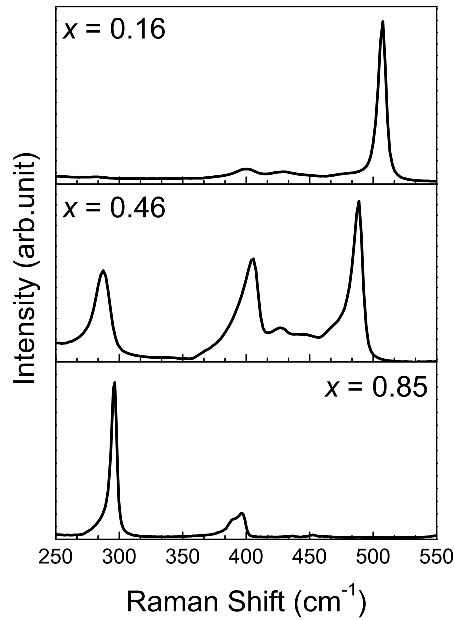

Figure 3.12: Three Raman spectra of relaxed $Si_{1-x}Ge_x$ alloys for different values of the composition x, as indicated in the panels. Three peaks are observed near 300, 400 and 500 cm^{-1}, related to Ge-Ge, Si-Ge and Si-Si vibrations respectively. Their spectral position and relative intensities clearly depend on the alloy composition.

peaks as a function of composition can be found in [107]. The spectrum at $x = 0.46$ also evidences an extended band between the Si-Si and the Si-Ge peak, whose presence can be individuated already at $x = 0.16$. A comprehensive treatment of the fine structures of the spectrum can be found in [108].

Finally, it is also evident from figure 3.12 that the frequency of the peaks changes with the composition. The origin of this effect is explained in detail in [110]. Measurements of the variation of the $Si_{1-x}Ge_x$ Raman peaks frequencies depending on the alloy composition were performed by several authors in the literature [111, 105, 106, 112, 109, 113], while theoretical calculations can be found in [114, 109]. In figure 3.13 the results from the most recent work are reported [113]. The variation is linear for the Si-Si and Ge-Ge mode, while the

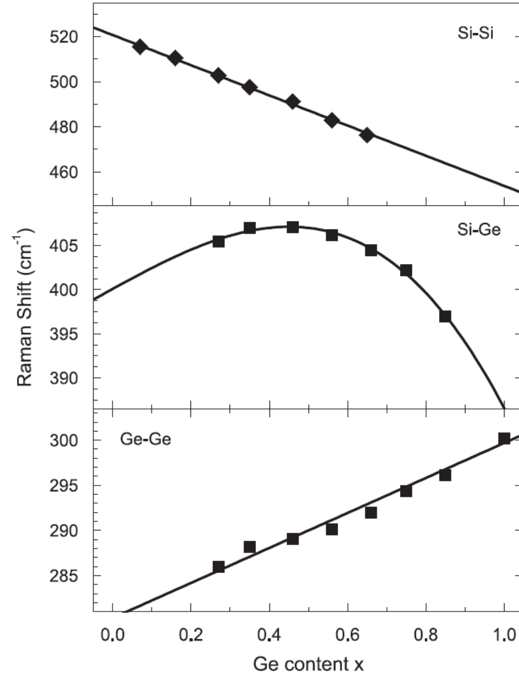

Figure 3.13: The frequency of each SiGe Raman peak is plotted as a function of the Ge content x, for a strain-free alloy. From [109].

Si-Ge peak exhibits a non linear behaviour. The fit of the data (solid lines) gives:

$$\begin{aligned} \omega_{Si-Si}(x,\varepsilon=0) &= 520.7-66.9x \\ \omega_{Si-Ge}(x,\varepsilon=0) &= 400.1+24.5x-4.5x^2-33.5x^3 \\ \omega_{Ge-Ge}(x,\varepsilon=0) &= 280.3+19.4x \end{aligned} \tag{3.6}$$

The presence of strain also gives a contribution by changing the bond spring constants, and shifting all the peaks in frequency [115, 116]. Since all the components of the strain tensor contribute to the shift of the Raman modes, the mathematical relations which describe the effect of strain can be generally very complicated [117], except in some particular cases in which the problem is simplified by the presence of particular symmetries in the system. As an example, for symmetrical biaxial strain in the (001) plane (which is very commonly encountered in the heteroepitaxy of $Si_{1-x}Ge_x$ due to the reticular mismatch between alloys with different composition) we have that the only nonzero components of the strain tensor are $\varepsilon_{11}=\varepsilon_{22}=\varepsilon_{||}$, and $\varepsilon_{33}=\varepsilon_{\perp}$: they are the parallel and perpendicular components of strain with respect to the [001] direction. In this case, the shift of the

Raman peaks in the strained alloy with respect to their frequency in the strain free material is simply proportional to $\varepsilon_{||}$, with a different linear coefficient b_i (called phonon strain coefficient) for each one of the three $Si_{1-x}Ge_x$ Raman modes. Many studies in the literature were devoted to the precise measurement of the strain coefficients b_i [116, 111, 118, 119, 120, 121, 122]. From [113] the three values of the strain coefficients are -730 cm^{-1}, -570 $cm^{-1}$and -470 $cm^{-1}$for the Si-Si, Si-Ge and Ge-Ge peaks respectively. The frequencies of the three $Si_{1-x}Ge_x$ Raman peaks as functions of both composition and strain are given therefore by:

$$\begin{aligned} \omega_{Si-Si}(x,\varepsilon_{||}) &= 520.7 - 66.9x - 730\varepsilon_{||} \\ \omega_{Si-Ge}(x,\varepsilon_{||}) &= 400.1 + 24.5x - 4.5x^2 - 33.5x^3 - 570\varepsilon_{||} \\ \omega_{Ge-Ge}(x,\varepsilon_{||}) &= 280.3 + 19.4x - 470\varepsilon_{||} \end{aligned} \tag{3.7}$$

The values of the strain coefficients given by Pezzoli et al. [113] are independent from the alloy composition, consistently with the predictions of a theoretical calculation performed by the same authors [123]. However, discussion in the literature about this point is still open [121, 122].

A method was proposed by Tsang [107] aimed at determining the composition and strain of an unknown $Si_{1-x}Ge_x$ sample from the frequencies of the Raman peaks. When the Raman spectrum of a sample is taken, the values of the frequency in equations 3.7 are fixed. A system of three equations in two unknown parameters (i.e. x and $\varepsilon_{||}$) is obtained. It is usually convenient to solve it graphically: each equation defines a curve in the x-$\varepsilon_{||}$ plane (figure 3.14), given by the ensemble of couples (x,$\varepsilon_{||}$) for which the equation is solved. If the peak frequencies and the calibration were determined without errors, the three curves would cross in a single point in the x-$\varepsilon_{||}$ plane, corresponding to the properties of the sample. In practice, due to the uncertainties in the method, the three curves are replaced by bands with finite width in the x-$\varepsilon_{||}$ plane. The intersection of the curves will be a finite area rather than a single point (see the inset in figure 3.14): its centroid gives the expected value of the sample properties, while its extension in the x-$\varepsilon_{||}$ plane gives an estimation of the experimental uncertainty on the obtained values.

Even if the calibration was obtained on bulk samples, the method was successfully applied also to nanostructured alloys, and in particular to self assembled $Si_{1-x}Ge_x$ islands and dots [124, 125, 126, 127, 128, 129, 95, 130]. We report the results from [127], in which $Si_{1-x}Ge_x$ islands were grown randomly on a flat Si

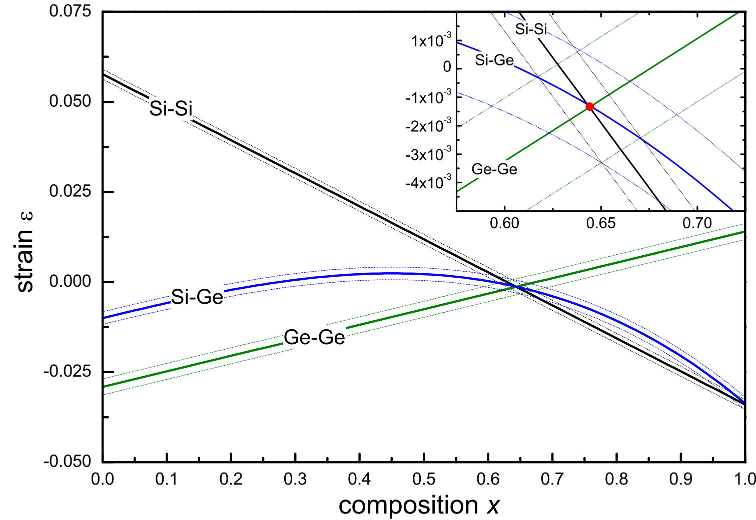

Figure 3.14: $x - \varepsilon$ plot for the determination of the composition and strain state of an unknown SiGe alloy from a single Raman measurement. The three curves are related to the three SiGe Raman peaks. The bands represent the uncertainty on the position of the curves: they are due to the uncertainties which affect both the measurement of the peak frequencies and the calibration reported in 3.7. In the inset, the crossing point of the three curves is plotted in detail: it represents the couple of values (x,ε) which are able to simultaneously give the observed positions of the three Raman peaks.

substrate and progressively etched in a wet chemical bath. The Raman spectrum of the nanostructures was taken after several etching steps, the shift of the Raman peaks was recorded and the method explained above was applied in order to obtain the average composition and strain of the material at the surface. The results are averaged because the laser spot on the sample includes many structures with different morphology, dimensions, and composition. In figure 3.15 the experimental data are shown.

It's worth noting that only two peaks (Ge-Ge and Si-Ge) are used in this work, due to the fact that the third peak (Si-Si) belonging to the island signal is completely covered by the Si-Si signal coming from the Si substrate (see the inset in figure 3.15, left panel). The presence of the intense signal coming from the substrate is almost always present in the Raman analysis of $Si_{1-x}Ge_x$ nanostructures grown on Si [131].

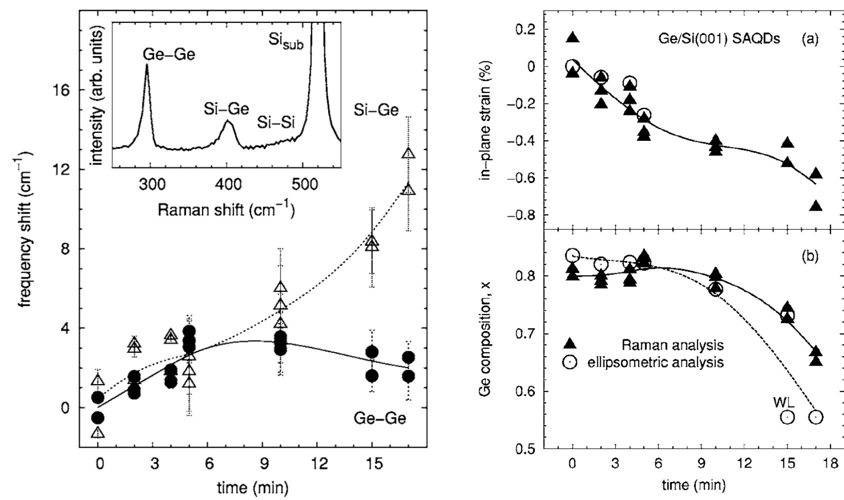

Figure 3.15: Results of the Raman analysis of Ge-rich self-assembled islands, as reported in [127]. Left: variation of the Ge -Ge and Si-Ge Raman peaks position as the etching of the islands proceeds. The typical Raman spectrum of the nanostructures is displayed in the inset. Right, panel (a) and (b): composition and strain of the nanostructured alloys, obtained from the Raman peak positions (black dots) and from ellipsometry measurements (white dots)

Chapter 4

Raman efficiency of $Si_{1-x}Ge_x$

In this chapter, a brief introduction to the basic features of the Raman effect in $Si_{1-x}Ge_x$ will be given. The origin of the Raman resonance in $Si_{1-x}Ge_x$ will be explained, and the results from the literature related to the two particular cases of pure Si (x=0) and Ge (x=1) will be reported. Then, in section 4.3 the experimental method for our measurement of the SiGe Raman efficiency will be presented; the experiment and the elaboration of the data will be described in detail. The results will be shown in section 4.4, and they will be compared to the theory. Finally, several experiments on SiGe nanostructures will be presented and the influence of Raman resonance effects dependent on the alloy composition will be highlighted in the interpretation of the results.

4.1 Theory of the Raman effect

4.1.1 Classical description

The Raman effect is originated from the inelastic scattering of the incident photons due to the interaction with the vibrations of the crystal. A classical picture of this interaction is given in the following. The vibrations of the crystal are described in terms of collective motions of the atoms, called normal modes or phonons: each normal mode j is characterized by a wavevector $\mathbf{q}_j$ and a frequency ω_j. At position $\mathbf{r}$, the amplitude ξ_j of the vibration is given by:

$$\xi_j = A_j e^{[\pm i(\mathbf{q}_j \cdot \mathbf{r} - \omega_j t)]} \tag{4.1}$$

where A_j is a constant. ξ_j is called normal coordinate of the phonon. The incident photon, with wavevector $\mathbf{k}_i$ and frequency ω_i, is described as an oscillating field $\mathbf{E}_i$ expressed as:

$$\mathbf{E}_i = \mathbf{E}_0 e^{[\pm i(\mathbf{k}_i \cdot \mathbf{r} - \omega_i t)]} \quad (4.2)$$

The polarization $\mathbf{P}$ induced by the electric field related to the incident photon is given by:

$$\mathbf{P} = \varepsilon_0 \chi \mathbf{E}_0 e^{[\pm i(\mathbf{k}_i \cdot \mathbf{r} - \omega_i t)]} \quad (4.3)$$

where χ is the electrical susceptibility tensor. This tensor depends on the frequency of the radiation, and expresses the response of the material to the incident field.

The presence of the phonons introduces a distortion of the crystal lattice: as a consequence, the electrical susceptibility tensor may be affected. We expand χ in powers of the phonon normal coordinate ξ_j:

$$\chi = \chi_0 + \frac{\partial \chi}{\partial \xi_j} \xi_j + \dots \quad (4.4)$$

where χ_0 is the susceptibility of the unperturbed crystal. The quantity defined as:

$$\mathbf{R}_j = \frac{\partial \chi}{\partial \xi_j} \xi_j$$

is a second rank tensor, called Raman tensor, related to phonon j. The substitution of this equation in the expression of the polarization gives immediately:

$$P = \chi_0 \varepsilon_0 \cdot \mathbf{E}_0 e^{[\pm i(\mathbf{k}_i \cdot \mathbf{r} - \omega_i t)]} + \varepsilon_0 \mathbf{E}_0 \frac{\partial \chi}{\partial \xi_j} A_j e^{[-i(\omega_i \pm \omega_q)t]} e^{[i(\mathbf{k}_i \pm \mathbf{q}_j) \cdot \mathbf{r}]} + \dots \quad (4.5)$$

The above expression shows that the scattered photons have three components, with different frequencies: one (Rayleigh scattering) has the same frequency of the incident radiation, while the other two have lower or higher frequency with respect to the incident photons. The amount of gained or lost frequency is equal to the frequency of the phonon involved in the scattering. The first case is referred to as Stokes process, while the second is usually called Anti-Stokes process. Exchange of more phonons is possible, and this can be included in the theory by considering the higher order terms in the expansion of the susceptibility.

Equation 4.5 includes the conservation of momentum:

$$\hbar \mathbf{k}_s = \hbar \mathbf{k}_i \pm \hbar \mathbf{q}_j \quad (4.6)$$

and energy:

$$\hbar\omega_s = \hbar\omega_i \pm \hbar\omega_j \tag{4.7}$$

As a consequence of the momentum conservation, it can be directly seen that the only phonons which can be involved in a first-order inelastic scattering are those located in the vicinity of the phonon Brillouin zone.

The scattered intensity, I, is linked to the polarization vectors of the incident and the scattered fields, $\mathbf{e}_i$ and $\mathbf{e}_s$, through the following relation:

$$I \propto \sum_j |\mathbf{e}_i \cdot \mathbf{R}_j \cdot \mathbf{e}_s|^2 \tag{4.8}$$

where $\mathbf{R}_j$ is the Raman tensor related to the phonon j. The shape of $\mathbf{R}_j$ has been obtained by Loudon [132] for all the 32 crystal classes. In Si, Ge and SiGe, three distinct Raman tensors exist, related to each one of the three optical phonons at the center of the Brillouin zone. In the basis given by the unit vectors [100], [010] and [001], their are represented as:

$$\mathbf{R}_1 = \begin{pmatrix} 0 & 0 & 0 \\ 0 & 0 & d \\ 0 & d & 0 \end{pmatrix} \quad \mathbf{R}_2 = \begin{pmatrix} 0 & 0 & d \\ 0 & 0 & 0 \\ d & 0 & 0 \end{pmatrix} \quad \mathbf{R}_3 = \begin{pmatrix} 0 & d & 0 \\ d & 0 & 0 \\ 0 & 0 & 0 \end{pmatrix} \tag{4.9}$$

4.1.2 Effect of strain in FCC crystals

In the relaxed material, the three phonons are degenerate in energy, due to the symmetry of the crystal. When strain is present, the degeneracy is partially or completely lifted due to the loss of symmetry of the deformed crystal [115]. The frequencies of the three optical modes can be obtained from the autovalues λ_j of the following matrix (secular equation) [115, 133]:

$$\begin{pmatrix} p\varepsilon_{11} + q(\varepsilon_{22} + \varepsilon_{33}) & 2r\varepsilon_{12} & 2r\varepsilon_{13} \\ 2r\varepsilon_{12} & p\varepsilon_{22} + q(\varepsilon_{33} + \varepsilon_{11}) & 2r\varepsilon_{23} \\ 2r\varepsilon_{13} & 2r\varepsilon_{23} & p\varepsilon_{33} + q(\varepsilon_{11} + \varepsilon_{22}) \end{pmatrix} \tag{4.10}$$

where the $\varepsilon_{\mu\nu}$ are the components of the strain tensor, and p, q, and r are material related constants, called deformation potentials [134]. The frequencies ω_j of the optical modes are given by:

$$\lambda_j = \omega_j - \omega_{j0} \tag{4.11}$$

where ω_{j0} is the frequency of the phonons in the unstrained material. This can be approximated by:

$$\Delta\omega_j = \frac{\lambda_j}{2\omega_{j0}} \tag{4.12}$$

For biaxial strain in the (001) plane ($\varepsilon_{11} = \varepsilon_{22} = \varepsilon_{||}$; $\varepsilon_{33} = \varepsilon_{\perp}$; other components null), the solution of the secular equation gives:

$$\lambda^{[100],[010]} = (p+q)\varepsilon_{||} + q\varepsilon_{\perp} \tag{4.13}$$

$$\lambda^{[001]} = 2q\varepsilon_{||} + p\varepsilon_{\perp} \tag{4.14}$$

which leads to:

$$\Delta\omega^{[100],[010]} = \frac{1}{2\omega_0}\left[p + q\left(1 - 2\frac{C_{12}}{C_{11}}\right)\right]\varepsilon_{||} = b^{[100],[010]}\varepsilon_{||} \tag{4.15}$$

$$\Delta\omega^{[001]} = \frac{1}{\omega_0}\left(q - \frac{C_{12}}{C_{11}}p\right)\varepsilon_{||} = b^{[001]}\varepsilon_{||} \tag{4.16}$$

where the $C_{\mu\nu}$ are components of the stiffness tensor. Equation 4.16 describes the proportionality between the biaxial strain and the shift of the [001] phonon, which was mentioned in section 3.5, and included in equations 3.7 for accounting for the presence of the strain.

In the deformed material, the polarization dependent selection rules change as well [117]. This is again described by means of the Raman tensors, which are modified according to the following equation:

$$\mathbf{R}_j^{'} = \sum_k \beta_{jk}\mathbf{R}_k \tag{4.17}$$

where the $\mathbf{R}_k$ are the Raman tensors of the unstrained material given in equation 4.9, and β_{jk} is the k-th component of the j-th eigenvector of matrix 4.10.

4.2 Raman efficiency and Raman resonance

Returning to equation 4.8, we better specify the relation of proportionality by expliciting the expression of the Raman scattering *differential cross section* [135]:

$$I \propto \frac{\partial S}{\partial\Omega\partial\omega_R} = \frac{{\omega_s}^4}{(4\pi)^2c^4}\left|\mathbf{e}_s\cdot\frac{d\chi}{d\xi}\cdot\mathbf{e}_s\right|^2(n+1)\frac{\hbar}{2\omega_q}\Delta(\omega_R - \omega_q) \tag{4.18}$$

where ω_s is the frequency of the scattered photon, ω_q is the frequency of the phonon involved in the scattering process, and ω_R is the Raman shift. $\mathbf{e}_s$ and $\mathbf{e}_i$ are the polarization unit vectors of the scattered and the incident light, $(n+1)$ is the Bose factor related to the phonon frequency ω_q, and $\Delta(\omega_R - \omega_q)$ is a function with unitary area which gives the shape of the Raman spectrum. For pure Si and Ge, it is a Lorentzian shape function. The link between the differential Raman shift and the measured intensity of the Raman signal is given by the properties of the material and the experimental apparatus, and will be discussed in section 4.3.1.

A detailed treatment of the theory of resonant Raman can be found in [135]: for our purposes it is enough to give some simple introductory remarks. From equations 4.5 and 4.18 it is evident that all the physics of the first order Raman effect is embedded in the derivative of the susceptibility χ with respect to the phonon normal coordinate ξ. In a very simplified picture we can think about a center zone phonon as a homogeneous ($k = 0$) deformation which changes the symmetry of the crystal and shifts the energy E of the electronic transitions in the material, so we write:

$$\frac{\partial \chi(\omega)}{\partial \xi} \propto \frac{\partial \varepsilon(\omega)}{\partial \xi} = \frac{\partial \varepsilon(\omega)}{\partial E}\frac{\partial E}{\partial \xi} = \frac{1}{\hbar}\frac{\partial \varepsilon(\omega)}{\partial \omega}\frac{\partial E}{\partial \xi} \tag{4.19}$$

where ε is the dielectric function of the material. The term $\partial E/\partial \xi$ is the definition of deformation potential, which is a material constant. The other term shows that the Raman scattering is large when the derivative of the dielectric function with respect to E is large: this occurs in the proximity of peaks of the dielectric function, due to the electronic transitions. In Si, Ge, and SiGe, the most prominent structures in the dielectric functions are due to the direct electronic transitions, as shown in figure 4.2.

It is evident from the figures that the energy of the direct electronic transitions is strongly dependent on the SiGe alloy composition. Figure 4.1 plots this dependence for four transitions, namely the $E_1/E_1+\Delta_1$, $E_0/E_0+\Delta_0$, $E_0^{'}$, and E_2. It is clear from figure 4.1 that Raman resonance effects are expected for Si, Ge and SiGe if the energy of the excitation light lies in the visible and near UV ranges. This was experimentally verified in Si and Ge by Renucci [136] and Cerdeira [137]. The Raman efficiency for Si and Ge as a function of the excitation light energy is reported in the two figures 4.3.

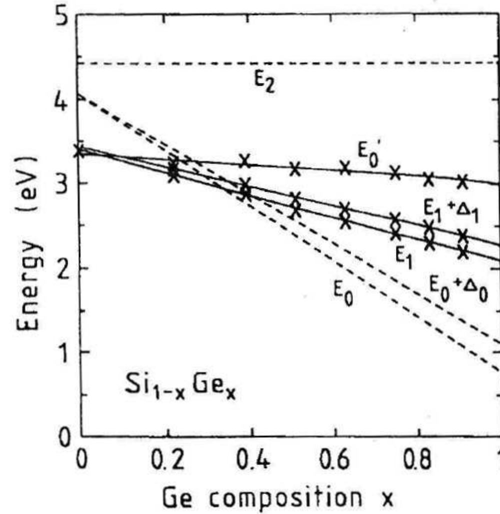

Figure 4.1: Energy of the direct electronic transitions in SiGe as a function of the alloy composition, from [6].

For $Si_{1-x}Ge_x$, the resonance conditions depend on the alloy composition x, as direct consequence of the curves plotted in figure 4.1. This opens an interesting problem: for a given excitation wavelength, the resonance conditions are met for some values of the composition and not for others: also the region of the compositional range in which the resonance is expected to occur depends on the used wavelength. This becomes particularly interesting in inhomogeneous $Si_{1-x}Ge_x$ samples, in which regions of alloy characterized by different values of the composition are probed *together*. In such systems, depending on the used excitation light energy, we can expect that some parts of the sample will be resonating and will contribute more to the Raman signal than others in which the resonance conditions are not fulfilled. By changing the excitation light energy, it could be also possible to selectively probe different parts of the sample.

These experimental approaches require the knowledge of the Raman efficiency of $Si_{1-x}Ge_x$ as a function of both the alloy composition x and the excitation light energy E. However, very few data are available in the literature. Some scattered measurements of the Raman efficiency in bulk $Si_{1-x}Ge_x$ as a function of the excitation energy (which is the most common approach) can be found for x = 0.77 in the range 2.4 eV - 2.6 eV (at room temperature) [138], and for x = 0.6 in the range 2.0 eV - 3.0 eV (at 100 K) [139]. All the data that can be retrieved in the

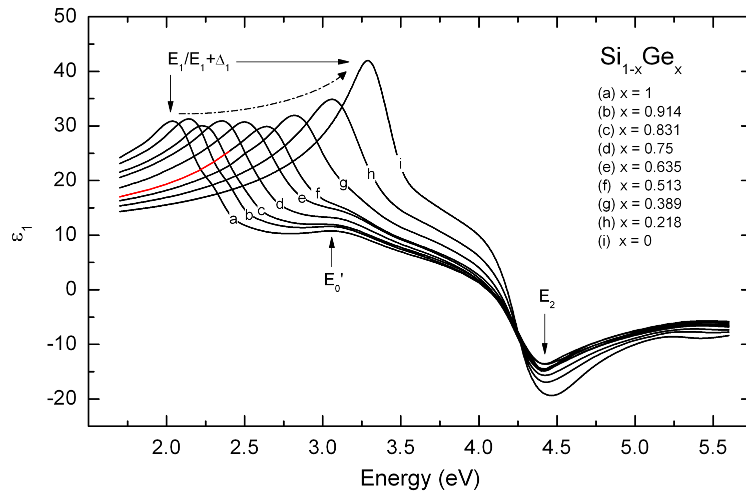

(a) *Real part*

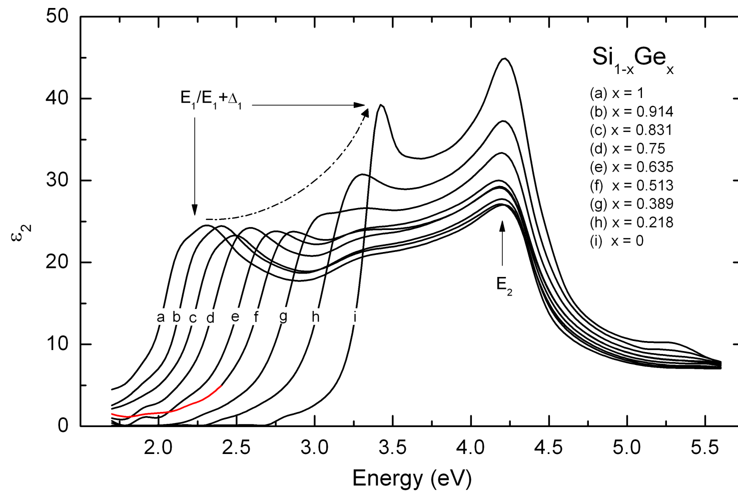

(b) *Imaginary part*

Figure 4.2: Dielectric function of $Si_{1-x}Ge_x$, as a function of frequency, for several values of the alloy composition. The direct transitions responsible for the structures in the dielectric function are evidenced. The data are taken from the work by Humlicek et al. [15]. The red parts of the curves for $x \approx 0.5$ are regions of unreliable data.

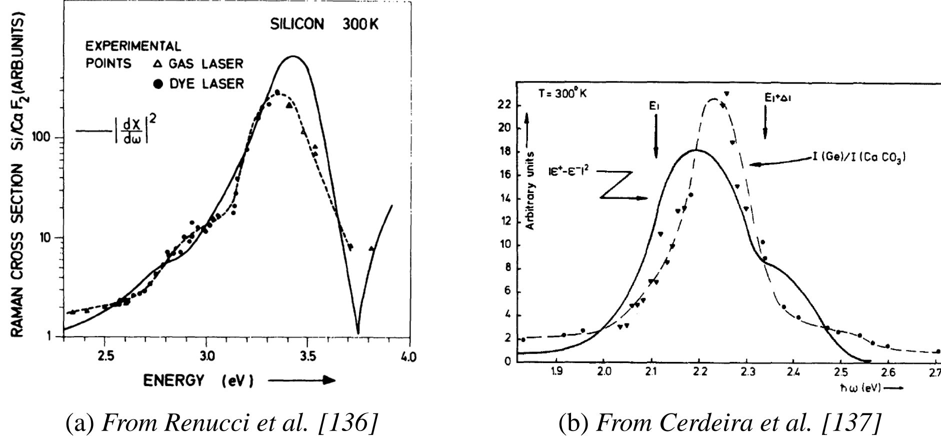

(a) *From Renucci et al. [136]* (b) *From Cerdeira et al. [137]*

Figure 4.3: Raman cross section in Si (a) and Ge (b), measured as a function of the excitation light frequency. A resonance peak is observed, corresponding to the energy of the $E_1/E_1+\Delta_1$ transitions in Si and Ge respectively.

literature are incomplete and cannot be directly compared. Our first purpose is therefore to bridge the gap between the existing data for pure Si and pure Ge, by means of a systematic measurement of the $Si_{1-x}Ge_x$ Raman efficiency over all the compositional range, for several excitation light energies.

4.3 Measurement of the Raman efficiency

4.3.1 From the theory to the experiment

The physical quantity which can be immediately determined in a Raman experiment is the intensity I of the Raman spectrum. In order to obtain the Raman efficiency, it is necessary to link the expression of the differential Raman efficiency, which we report again in the following:

$$\frac{\partial S}{\partial\Omega\partial\omega_R} = \frac{{\omega_s}^4}{(4\pi)^2c^4}\left|\mathbf{e}_s\cdot\frac{d\chi}{d\xi}\cdot\mathbf{e}_s\right|^2(n+1)\frac{\hbar}{2\omega_q}\Delta(\omega_R-\omega_q) \tag{4.20}$$

to the experimentally measured intensity. Both the properties of the sample and the experimental configuration must be taken into account. First of all, we set the polarizations of the scattered and incident intensity: with reference to our

experiment, $\mathbf{e}_s = \mathbf{e}_i = [1\bar{1}0]$. Under this geometrical configuration, we have:

$$\begin{aligned} \mathbf{e}_s \cdot \mathbf{R}_1 \cdot \mathbf{e}_i &= 0 \\ \mathbf{e}_s \cdot \mathbf{R}_2 \cdot \mathbf{e}_i &= 0 \\ \mathbf{e}_s \cdot \mathbf{R}_3 \cdot \mathbf{e}_i &= d \end{aligned} \tag{4.21}$$

where the Raman tensors of the relaxed material, given in equations 4.9, have been used. The justification of this choice will become clear in section 4.4. From equations 4.21, it turns out that only the phonon along the [001] direction is visible in the adopted experimental configuration, and the term $|\mathbf{e}_s \cdot \frac{d\chi}{d\xi} \cdot \mathbf{e}_s|^2$ can be substituted in equation 4.20 simply by $|d|^2$.

Equation 4.20, integrated over a Raman shift range R which completely includes the lineshape function $\Delta(\omega_R - \omega_q)$ (with unitary area) and over the collection solid angle Ω, gives the Raman efficiency S, defined as the ratio between the scattered and the incident photons per unit length inside the material. The collection angle Ω_0 outside the sample is constant: it is defined by the numerical aperture of the optical element used for collecting the signal. In our experiment, a microscope objective was used. The collection angle *inside* the sample, which is the correct parameter Ω to insert in the previous equation, is different from Ω_0 due to the light refraction at the sample surface, ruled by the Snell's law. Due to the high index of refraction of SiGe (about 4 in the optical range) the solid angle Ω inside the material is quite small even for a N.A. equal to 0.75 (typical of our microscope objectives) and the integral can be approximated well by the simple multiplication by Ω.

The scattered observable intensity, i.e. the number of scattered photons emerging from the sample, is limited by the optical absorption inside the material and the trasmissivity of the sample surface. In our experimental configuration (backscattering), the number of observable photons dI_s^* coming from a thin slab with thickness dz and located at depth z beneath the sample surface is given by the following expression:

$$dI_s^* = S \cdot I_0 \cdot T^2 \cdot e^{-2\frac{z}{L}} dz \tag{4.22}$$

where I_0 is the incident light intensity, L is the penetration depth of the light inside the material, and T is the optical trasmissivity of the sample surface. Both the

trasmissivity and the optical absorption are counted twice, once for the incoming light and once for the backscattered signal. The total observable intensity of the Raman signal is obtained from the integration of the above equation with respect to dz:

$$I^* = I_0 \cdot S^* = I_0 \cdot \left(S \cdot \frac{\left(1 - e^{-2D/L}\right)}{2} L \cdot T^2 \right) \tag{4.23}$$

where D is the physical thickness of the sample. The dimensionless ratio S^* between the total observable Raman intensity and the incident excitation light intensity I_0 is called observable Raman efficiency.

Finally, the *measured* signal intensity I is related to the observable intensity through the efficiency η of the optical system used for the collection of the signal (lenses, mirrors, filters, monochromator, detector): $I = \eta I^*$.

Two cases are particularly interesting: in the first, which applies to opaque bulk samples, $L << D$. The intensity is given by the expression:

$$I = I_0 \cdot \eta \cdot S^* = I_0 \cdot \eta \cdot \left(S \cdot \frac{L}{2} \cdot T^2 \right) \tag{4.24}$$

In this case, the measured intensity of the scattered signal is simply proportional to the penetration depth of the light and the Raman efficiency, while the sample thickness plays no role. The second situation is given by the opposite limit, $L >> D$, corresponding to samples in which the penetration depth of light is much longer than the sample thickness; after taking the series expansion of the exponential at the numerator of equation 4.23, we obtain:

$$I^* = I_0 \cdot \eta \cdot S^* = I_0 \cdot \eta \cdot \left(S \cdot D \cdot T^2 \right) \tag{4.25}$$

where the series expansion has been truncated after the linear term in D/L. The intensity of the scattered signal is now simply proportional to the Raman efficiency and the sample thickness.

In order to measure the Raman cross section of $Si_{1-x}Ge_x$, a series of Raman spectra of the alloy must be recorded for different values of the composition x and the excitation light frequency ω. The intensity of the Raman signal must be found by properly integrating the Raman spectra with respect to the Raman shift, and then corrected for all the factors which appear in the above equations.

However, there is a way to reduce the number of parameters which must be estimated. This is achieved by means of *relative* measurements of the Raman efficiency [135]. A reference sample with known Raman efficiency is measured under the same experimental conditions used for the sample under study. When the ratio between the intensities of the Raman signals of the sample and the reference is taken, several common factors are canceled out: in particular, the excitation light intensity I_0, the optical system efficiency η, the fourth power of the scattered light frequency ω^4 and all the constants appearing in expression 4.20. This brings a substantial simplification in the elaboration of the experimental data.

In the literature, high bandgap materials like calcite ($CaCO_3$) and fluorite (CaF_2) are commonly used as reference samples. This choice is based on the fact that the energy of the electronic transitions in these materials (about 5 and 10 eV respectively) is well above the energy of the excitation light in the visible and UV range (2 - 4 eV): due to the absence of structures in the dielectric function in the entire visible and near UV spectrum range, the Raman efficiency remains constant (though small) over all the energy range. This holds also for the optical constants entering the expression of the Raman intensity. As a consequence, the use of the same reference for all the measurements with different excitation energies allows comparing directly the results.

4.3.2 Experiment

The experimental strategy for the determination of the $Si_{1-x}Ge_x$ Raman efficiency for several excitation wavelengths over the whole compositional range is based on the use of a *single* sample, which consists of a thick (20 μm) graded $Si_{1-x}Ge_x$ buffer grown on a flat (001) Si wafer by Low Energy Plasma Enhanced Chemical Vapour Deposition (LEPECVD) [140, 141, 142]. During the growth the fluxes of silane (SiH_4) and germane (GeH_4) in the reactor chamber were varied in order to obtain a linear variation of the alloy composition x with respect to the film thickness, between 0 (pure Si) and 1 (pure Ge). The compositional gradient in the graded buffer is therefore constant and equal to 0.05/μm. An additional micron of pure Ge was finally added at the surface of the sample, so that the total thickness of the sample is 21 μm. In figure 4.4 an optical microscope image of the sample, cleaved and observed in cross section, is reported, together with the

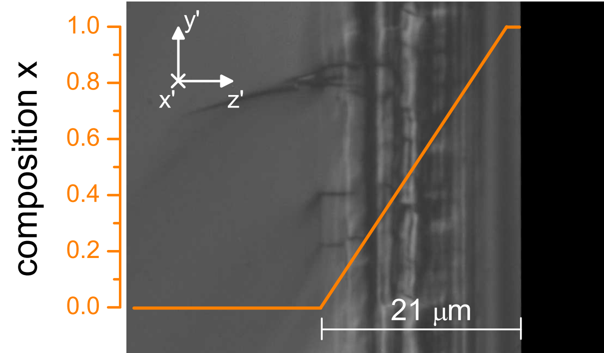

Figure 4.4: Microscope image of the cleaved lateral surface (110) of the sample. Superimposed to the optical image, the composition profile along the growth direction is shown.

plot of the internal alloy composition with respect to the thickness.

The $\mathbf{x}'$, $\mathbf{y}'$, and $\mathbf{z}'$ vectors in the figure represent the [110], $[1\bar{1}0]$ and the [001] crystallographic directions respectively. The roughness of the cleaved surface is indicative of the high density of dislocations inside the graded buffer, whose thickness is well beyond the critical value for plastic relaxation. The Raman spectra of $Si_{1-x}Ge_x$ at different composition values can be directly measured by scanning the graded buffer along the growth direction with a Raman spectrometer in micro configuration, i.e. in which the laser light used for the excitation is focused on the sample surface by means of a microscope objective. For a typical microscope objective with a numerical aperture equal to 0.75, and for wavelengths in the optical range, the diameter of the laser spot is in the range of 1 μm.

The Raman experiments are enormously simplified: actually, all the measurements over the whole compositional range for a given excitation wavelength are carried out in only one run. This also makes sure that the experimental conditions (focus, sample orientation) are the same for all the values of the composition. Moreover, the resolution of the sampling is a free parameter, which can be set directly by choosing the scanning step Δz along the growth direction: the Raman efficiency vs alloy composition x is sampled with intervals in composition given by $\Delta x = 0.05\mu\text{m}^{-1} \cdot \Delta z$. The uncertainty on the value of the composition x at position z is given by the composition interval included in the diameter of the spot; for a diameter around 1 μm, the uncertainty is about 0.05. Finally, it is worth noting that this experimental approach naturally leads to give the variation of the

$Si_{1-x}Ge_x$ Raman efficiency with respect to the alloy composition, thus providing a direct picture of how the Raman resonance plays its role in presence of composition inhomogeneities. The same scans, performed with different excitation energies, give a complete view of the variations of the $Si_{1-x}Ge_x$ alloy resonance behaviour under different illuminations. In this work, the experiments were carried out for 6 different excitation energies in the UV and optical range: 3.40 eV (364 nm), 3.08 eV (402 nm), 2.71 eV (458 nm), 2.54 eV (488 nm), 2.33 eV (532 nm) and 1.96 eV (633 nm).

4.3.3 Experimental details

The graded buffer, cleaved along the [110] crystallographic direction, was kept vertical by means of a sample holder mounted on a piezoelectric xyz stage (Physik Instrumente NanoCube). The piezoelectric stage had a maximum travel range of 100 μm along the xyz directions, with a spatial resolution of 10 nm. The scans were performed along the $\mathbf{z}'$ direction with steps of 0.3 μm, corresponding to intervals of about 0.015 in the alloy composition. The starting point of the scan was placed in the Si substrate region; the line scan ended several microns outside the sample, after crossing all the graded buffer. The laser intensity was always limited in order to prevent the sample from heating, since the thermal conduction of a $Si_{1-x}Ge_x$ graded buffer is known to be quite poor [109]: a laser intensity at the sample surface in the order of 1 mW was found to be low enough. The geometrical configuration of the Raman measurement was $\mathbf{x}'(\mathbf{y}',\mathbf{y}')\bar{\mathbf{x}}'$ in Porto's notation [143].

The Raman spectra were recorded with a Jasco R800 double additive spectrometer with a notch filter to reject the laser light, and with a Horiba Jobin-Yvon T64000 triple spectrometer with the first two monochromators in subtractive mode when a notch filter was not available (in particular, at 402 nm). The entrance slit of the monochromators was set at 100 μm. Both instruments were equipped with a Charge Coupled Device (CCD) for multichannel acquisition.

4.3.4 Experimental data and remarks

Figure 4.5 shows the result of one line scan, performed with 2.33 eV excitation energy. Only 21 spectra are plotted for clarity, shifted along the y-axis in order

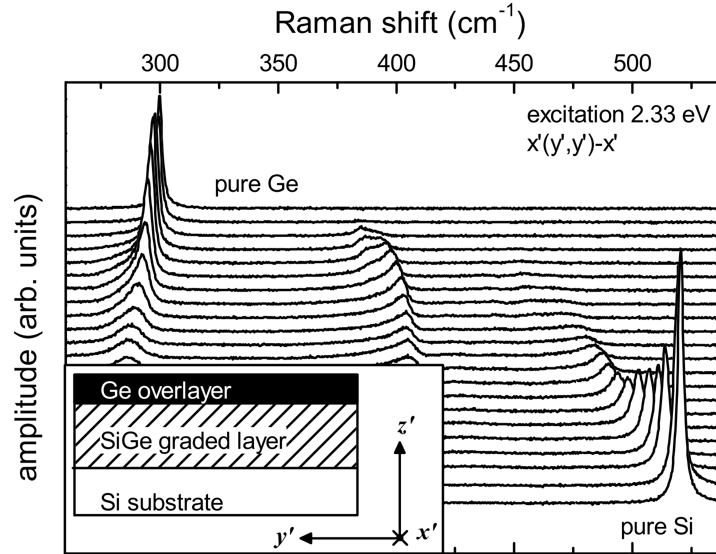

Figure 4.5: Series of spectra taken on the graded buffer with an excitation energy of 2.33 eV. The variation of the position and the intensity of the SiGe Raman peaks depending on the alloy composition are well visible and finely traced. The spectra shown in the figure are sampled with steps of 0.05 in the Ge content. The three curves plotted in figure 3.13 can be directly individuated in the sequence of the spectra. It is worth noting that the intensity of the signal in pure Ge is of the same order of magnitude than in Si, even if the penetration depth (and consequently the scattering volume) is about 50 times lower (see equation 4.24). This is due to the resonance effect in Ge, which actually occurs at this excitation energy.

to highlight their variation with respect to the position in the graded buffer. In the inset, the geometrical configuration of the experiment is reported. The Raman spectra exhibit the typical shape of a crystalline $Si_{1-x}Ge_x$ alloy; the Raman peaks change in intensity and frequency along the line scan, following the variation of the local composition. It can be noted that the maxima of the Raman bands nicely draw the curves plotted in figure 3.13, describing the variation of the Raman frequency versus the alloy composition in the relaxed material. The alloy composition and strain in each point can be directly extracted from the Raman spectra, by means of the calibration reported in section 3.5: actually, as it was shown in section 4.3.1, the phonons considered in the calibration are the same probed in our experimental configuration.

In figure 4.6, panel (a), the values of the alloy composition $x(z)$ obtained from

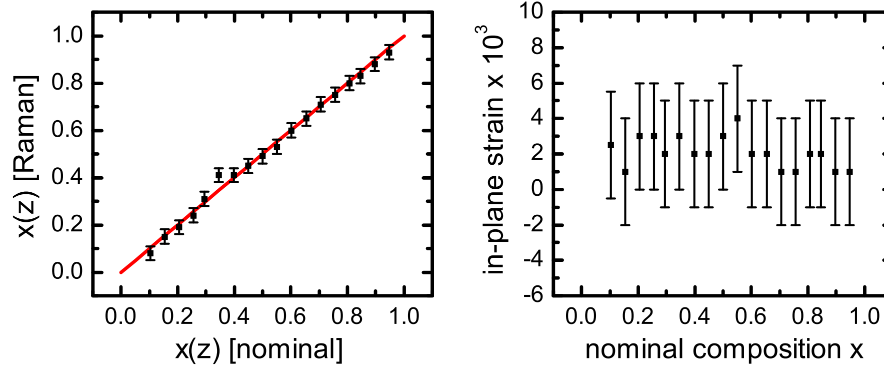

Figure 4.6: Panel (a): comparison between the measured (y-axis) and nominal (x-axis) composition profiles $x(z)$ in the graded buffer. Each point relates to the same value of z. The red line gives the condition x=y. Panel (b): residual strain in the graded buffer, measured from the Raman spectra. The strain is always compatible with zero within the experimental uncertainty.

the Raman spectra are plotted versus the expected composition values (i.e. inferred by the nominally constant composition gradient inside the graded buffer); the red line displays the $x = y$ condition. The linear behaviour of the composition profile inside the buffer is confirmed by the Raman data. In panel (b), the in-plane strain found in the buffer is plotted vs the position along the line scan: the strain is always compatible with 0 over the entire buffer, as expected from the fact that the thickness of the sample is far beyond the critical value for plastic relaxation. This suggests the use of the Raman tensors for the relaxed material (see section 4.3.1. The tendency to slightly tensile strain values could be explained by the thermal strain induced by the post growth cooling of the sample, due to the dependence of the thermal expansion coefficient of $Si_{1-x}Ge_x$ on the alloy composition [9].

A source of random errors is given from the variations in the focus conditions on the sample caused by the surface roughness. It was chosen to perform several line scans starting from different point in the sample, in order to directly estimate the intensity fluctuations caused by the randomly varying focus conditions and local strain. The integrated intensity of the spectra was found to be repeatable within 5%.

4.3.5 Data elaboration

According to section 4.3.1, the Raman spectra collected along the graded buffer are integrated in order to obtain the total intensity $I(x,\omega)$, where x is the alloy composition and ω is the frequency of the excitation light. This point is not straightforward and requires a discussion. In section 4.3.1 a single phonon with frequency ω_q was considered (see equation 4.20), with an associated spectral shape function $\Delta(\omega_R - \omega_q)$, with unitary area, where ω_R is the Raman shift, or the abscissa of the spectrum; ω_q enters also the Bose factor $(n+1)$. For a $Si_{1-x}Ge_x$ alloy the framework is a bit more complicated because three "phonons"are present, each one located at different Raman shift values. This means that a different value of the Bose factor $(n+1)$ and phonon frequency ω_q in equation 4.20 is associated to each one. Then, the three peaks must be integrated separately, over three distinct spectral ranges: their intensities are corrected for the respective Bose factor and phonon frequency, and then summed again. For each phonon i (i.e. Si-Si, Si-Ge and Ge-Ge), the correcting factor will be given by the reciprocal of:

$$\frac{(n_i+1)}{\omega_i} = \left(\frac{1}{e^{\omega_i(x)/200cm^{-1}}+1}+1\right)\cdot\frac{1}{\omega_i(x)} \tag{4.26}$$

where the functions $\omega_i(x)$ are given by equations 3.6, and where kT at room temperature (0.025 eV) has been expressed as 200 cm^{-1}. A quick estimation of the correcting factor for each phonon can be obtained by considering the typical frequencies of 500, 400 and 300 cm^{-1} for the Si-Si, Si-Ge and Ge-Ge phonons respectively: the related correcting factors are about 465, 360, 250 cm^{-1}. When the correction is taken separately for each distinct phonon, therefore, there is an enhancement of the contribution of the Si-Si mode with respect to the Ge-Ge mode.

An approximated treatment is given by neglecting the difference in the Bose factors and phonon frequencies, directly integrating all the Raman peaks together. Though less rigorous, this approach gives results which are more easily usable for the practical applications that will be presented in Chapter 5. A comparison of the results given by following the two procedures will be presented in section 4.4.2.

The remaining corrections are the same for both cases. As was introduced in section 4.3.4, a sample of CaF_2 was used as reference for the Raman efficiency for all the used excitation energies. In particular, a 3 mm-thick synthetically grown single crystal of CaF_2, cleaved along the (110) plane, was measured under the

same experimental conditions used for the graded buffer. Since the Raman tensors of fluorite have the same form than in Si, Ge and $Si_{1-x}Ge_x$ [135], the same polarization selection rules hold. In order to obtain the intensity of the CaF_2 Raman signal, therefore, the same equations given in section 4.3.1 can be applied.

We write in the following the intensities of the $Si_{1-x}Ge_x$ and the CaF_2 samples (they are meant to have been already corrected for the respective Bose factors):

$$I(x,\omega) = \frac{\hbar\omega^4}{(4\pi)^2c^4} d^2(x,\omega)\Omega(x,\omega)\frac{L(x,\omega)}{2}T^2(x,\omega)\eta(\omega) \tag{4.27}$$

$$I_{CaF_2}(x) = \frac{\hbar\omega^4}{(4\pi)^2c^4} d^2_{CaF_2}\Omega_{CaF_2}D_{CaF_2}{T_{CaF_2}}^2\eta(\omega) \tag{4.28}$$

The dependence of all the factors appearing in the two above equations on the $Si_{1-x}Ge_x$ composition x and the excitation light frequency ω has been explicited: as introduced previously, all the optical functions of fluorite can be considered constant in the visible and near UV range. In equation 4.27, condition 4.24 was used, while for CaF_2, which is transparent, equation 4.25 was included. In equation 4.28, finally, it must be pointed out that the CaF_2 Raman signal is limited by the microscope objective depth of focus (D.O.F.) rather than by the CaF_2 sample thickness D_{CaF_2}. The D.O.F. can be estimated through the following expression:

$$D.O.F. = \frac{\lambda_0 n}{NA^2} \tag{4.29}$$

For λ_0 in the visible range, a numerical aperture equal to 0.75, and the index of refraction of CaF_2 taken equal to 1.43, the D.O.F. is in the range of 1.3 μm. This is much less than the thickness of the CaF_2 sample (3 mm). So we substitute D_{CaF_2} in equation 4.28 with the quantity $DOF(\omega,NA)$.

The ratio between equations 4.27 and 4.28 gives:

$$\begin{aligned}\frac{I(x,\omega)}{I_{CaF_2}} &= \frac{1}{2\Omega_{CaF_2}T^2_{CaF_2}}\frac{d^2(x,\omega)}{d^2_{CaF_2}}\frac{\Omega(x,\omega)L(x,\omega)T^2(x,\omega)}{DOF(\omega,NA)} = \\ &= K\cdot\frac{\Omega(x,\omega)L(x,\omega)T^2(x,\omega)}{DOF(\omega,NA)}d^2(x,\omega)\end{aligned} \tag{4.30}$$

where all the common factors have been canceled out, and the terms independent from x and ω have been grouped into a single *constant* K.

The denominator in equation 4.30 can be calculated through equation 4.29; the other parameters, i.e. the $Si_{1-x}Ge_x$ surface trasmissivity, the collection solid

angle and the penetration depth of the light in the material, are determined from the $Si_{1-x}Ge_x$ optical constants through the following expressions:

$$T(x,\omega) = \frac{(n(x,\omega)-1)^2 + k^2(x,\omega)}{(n(x,\omega)+1)^2 + k^2(x,\omega)} \quad (4.31)$$

$$\Omega(x,\omega) = 2\pi(1 - \sqrt{1 - \frac{NA^2}{n(x,\omega)^2}}) \quad (4.32)$$

$$L(x,\omega) = \frac{4\pi k(x,\omega)}{\lambda} \quad (4.33)$$

where $n(x,\omega)$ and $k(x,\omega)$ are the real and imaginary part of the $Si_{1-x}Ge_x$ index of refraction, while λ, the excitation light wavelength, is related to ω by the relation $\lambda = 2\pi c/\omega$, c being the speed of light in vacuum.

In order to perform these corrections, the values of $n(x,\omega)$ and $k(x,\omega)$ have to be known. Many works dedicated to the measurement of the optical constants of $Si_{1-x}Ge_x$ can be found in the literature (see [15, 144, 145] and the references therein). The optical constants were usually measured by means of ellipsometry and reflectometry in the visible and UV range. The data available in the literature were collected and discussed in two reviews which can be found in [146, 147], which were taken as our source of values for the $Si_{1-x}Ge_x$ index of refraction. In particular, the data from [15] and [144] are in good agreement and are listed in the review, while discrepancies with the data from [145] exist, due mainly to the preparation of the sample surface. However, no data are told to be reliable for $Si_{1-x}Ge_x$ for low values of the absorption coefficient α: below 0.01 nm^{-1} no values are reported, except for Si.

In figure 4.7, the available values of the penetration depth of light are displayed as a function of the alloy composition x. The black spots are the data: the lack of points for low excitation energy is evident. However, in order to correct the Raman intensity $I(x,\omega)$ for the penetration depth $L(x,\omega)$ we need values throughout all the compositional range. The spaces between the experimental points have been filled by a shape-preserving interpolation with MatLab (Piecewise Cubic Hermite Interpolating Polinomial). For the upper excitation energies (3.40 eV, 3.08 eV, 2.71 eV and 2.54 eV), the interpolation of the data is able to fill easily the space between the known values of the penetration depth. For 2.33 eV and 1.96 eV, the curves found with this interpolation are somehow more arbitrary; in lack of alternatives, we decided anyway to proceed with these data. In section 4.4.1 it will

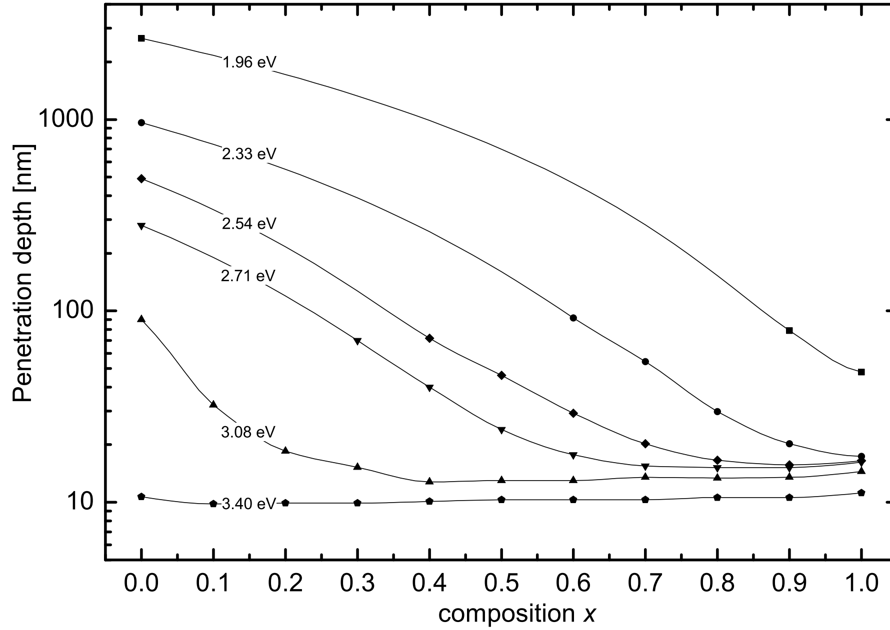

Figure 4.7: Penetration depth of light as a function of the SiGe composition x and the excitation light energy. The black dots are the values extracted from the data given by [146], while the continuous lines show the interpolation of the data.

be shown that the results turn out to be consistent with a semiempirical calculation of the behaviour of the Raman efficiency with respect to the alloy composition, for all the excitation energies.

4.4 Results

The results of the data elaboration depicted in the previous sections are displayed in figure 4.8. Six curves of efficiency are obtained, one for each value of the excitation light energy, from the UV (3.40 eV, panel (a)) to the red (1.96 eV, panel (f)). Due to the overall constant K in equation 4.30, the y-axes have the same scale, though in arbitrary units, and the curves are directly comparable. A strong modulation of the $Si_{1-x}Ge_x$ Raman efficiency actually exists depending on the alloy composition and excitation energy. A main resonance peak with half width at half maximum between 0.10 and 0.15 in composition is observed, its maximum moving toward Ge-richer composition values as the excitation light energy

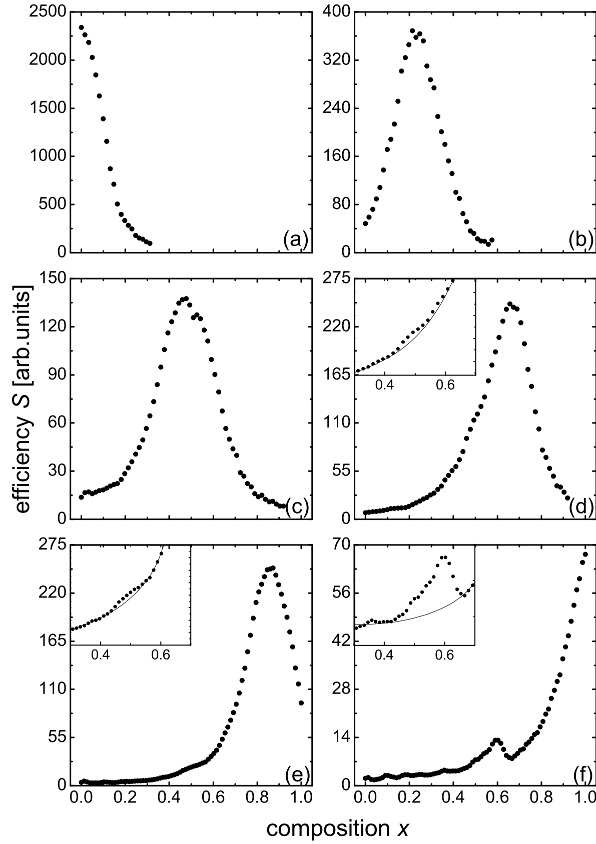

Figure 4.8: Raman efficiency of SiGe as a function of the alloy composition x, for different values of the excitation energy: (a) 3.40 eV, (b) 3.08 eV, (c) 2.71 eV, (d) 2.54 eV, (e) 2.33 eV and (f) 1.96 eV. The insets in panels (d)-(f) put into evidence the minor resonance peak due to the $E_0/E_0 + \Delta_0$ direct electronic transitions: the lines are guides to the eye.

decreases. At 3.40 eV, the maximum of the resonance peak is exactly located at x = 0; at 1.96 eV, the maximum of the resonance peak seems to fall outside the compositional range. The maximum width of the peak is obtained for 2.71 eV, in correspondence of which the resonance peak is in the middle of the compositional range. This suggests that the broader width is connected to the alloy disorder in the material, which is maximum for $x = 0.5$. In the insets of the three last panels, the presence of a secondary resonance is highlighted, in the form of a little shoulder on the main peak at 2.54 and 2.33 eV, and of a well defined secondary peak at 1.96 eV excitation wavelength. Also this secondary peak drifts toward Ge-richer

Energy [eV]	Main peak	Secondary peak
3.40	0	-
3.08	0.23	-
2.71	0.51	-
2.54	0.67	0.46
2.33	0.86	0.49
1.96	-	0.59

Table 4.1: Position of the main and secondary resonance peaks vs the energy of the excitation light used for the experiment

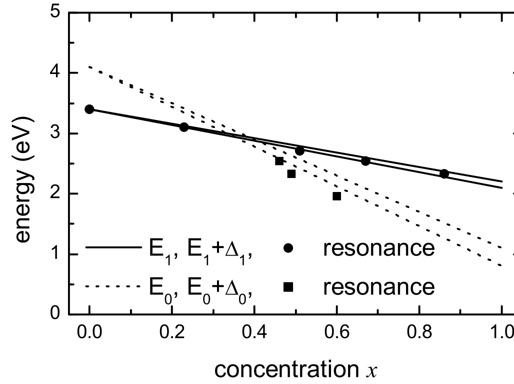

Figure 4.9: Comparison of the position of the Raman resonance peaks in SiGe, depending on the excitation energy, and the behaviour of the $E_1/E_1+\Delta_1$ and $E_0/E_0+\Delta_0$ direct electronic transitions in SiGe.

composition values with decreasing excitation energy. All these observations are directly related to the properties of the dielectric function of $Si_{1-x}Ge_x$, which was discussed in section 4.1.1, as we show in detail in the following. In table 4.1, the position of the resonance structures (main and secondary) along the composition axis are listed with respect to each value of the excitation light energy:

The data listed in table 4.1 can be directly compared to the energy of the direct transitions in $Si_{1-x}Ge_x$ depending on the alloy composition, as reported in figure 4.1: the data are summarized in figure 4.9. The agreement between the position of the main resonance peak and the behaviour of the $E_1/E_1+\Delta_1$ transitions is very good, while the secondary peak seems to follow the curves related to the $E_0/E_0+\Delta_0$ direct electronic transitions. In this case the agreement is evidently worse, but the attribution to the $E_0/E_0+\Delta_0$ transition can be considered valid.

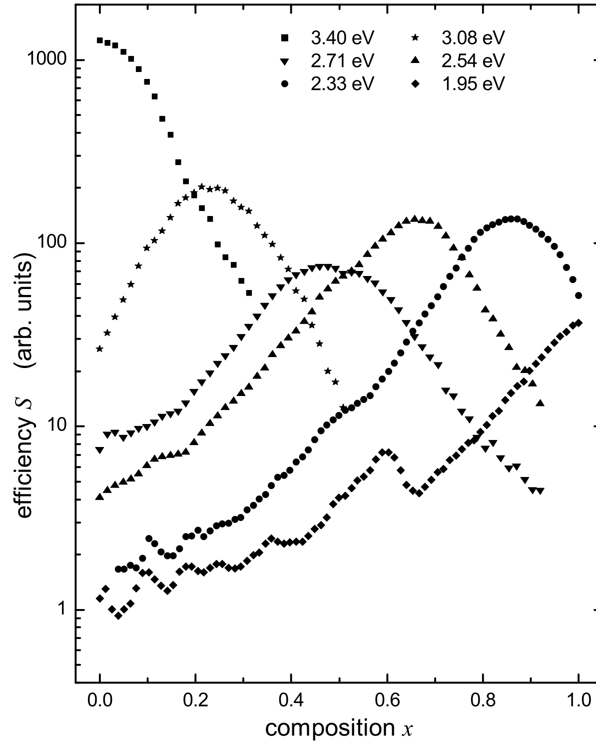

Figure 4.10: Raman efficiency of SiGe, as a function of the alloy composition x and excitation light energy, in logarithmic scale. The highest modulation is found for an excitation energy equal to 3.40 eV (3 orders of magnitude throughout the entire compositional range), while the lowest effect is found for 1.96 eV.

The vicinity of the $E_1/E_1+\Delta_1$ and $E_0/E_0+\Delta_0$ transitions for $x < 0.5$ explains why it is not possible to observe the secondary peak for energies equal or higher than 2.71 eV. Moreover, the lower height of the secondary peak with respect to the main one is fully explained by the lower oscillator strength of the $E_0/E_0+\Delta_0$ transitions, as can be directly understood from figure 4.2. The good matching with the $E_1/E_1+\Delta_1$ transitions in the bulk gives also a direct confirmation that the residual strain in the graded buffer is low enough to not change the energy of the bands, as it was guessed from the estimation of the strain given in figure 4.6.

By plotting all the curves in logarithmic scale on the same graph (figure 4.10) it is possible to more easily visualize the relationships existing between the Raman efficiency curves. The height of the Raman resonance peak is not constant throughout the compositional range: it presents a maximum in pure Si for 3.40 eV, and a minimum for 2.71 eV. A factor 10 exists between the resonance peak heights

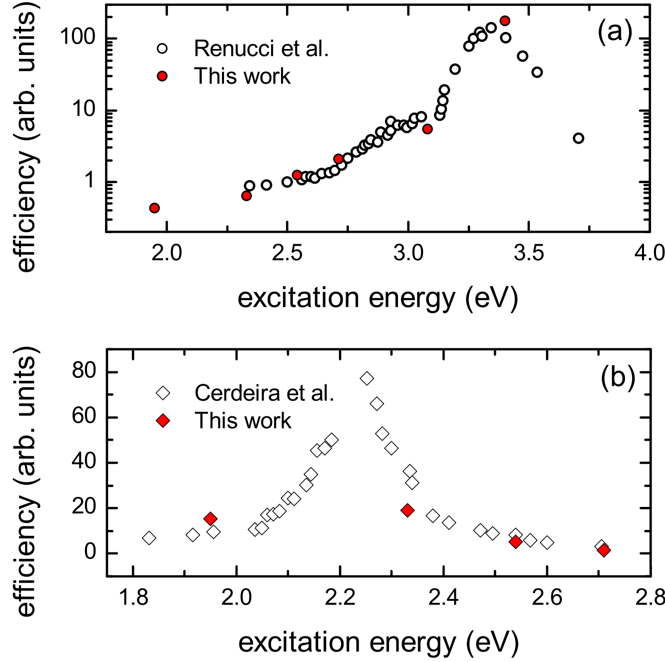

Figure 4.11: Comparison between the Raman efficiency values of Si (panel (a)) and Ge (panel (b)) found in this work and the results from the literature ([136], [137]).

in Si and Ge (see the curve related to 2.33 eV excitation energy). The efficiency varies up to 2 orders of magnitude with varying composition for a given excitation energy; on the other hand, the variation with respect to the excitation energy for a fixed composition is between 2 and 3 orders of magnitude (the maximum effect is seen for $x = 0$). A doublecheck on the validity of our results can be provided by the comparison of our data for pure Si and Ge, expressed vs the excitation energy, to the results from the literature plotted in figures 4.3. Figure 4.11 demonstrates a good agreement between our data (red spots) and the results in the literature.

4.4.1 Comparison with the theory

In order to understand the principal features of the Raman resonance effect in $Si_{1-x}Ge_x$ (i.e. position and height of the main resonance peak), it is useful to consider the indications coming from the theory of the Raman resonance given by the $E_1/E_1 + \Delta_1$ direct electronic transitions. The theory applied to the cases

of Si and Ge can be found in [136] and [137], while a more general treatment is given by [135]. The matrix element d which appears in the Raman tensors given in equations 4.9 is proportional to the quantity:

$$\partial\chi \propto \frac{\sqrt{2}}{\sqrt{3}} d^5_{3,0} \left[\frac{2(\chi^+ - \chi^-)}{\Delta_1} \right] + \frac{d^5_{1,0}}{2\sqrt{3}\hbar} \frac{d\chi}{d\omega} \tag{4.34}$$

which expresses the variation of the susceptibility under the deformation induced by the phonon. In the above equation, $d^5_{3,0}$ and $d^5_{1,0}$ are deformation potentials, χ^+ and χ^- are the contributions to the susceptibility function given by the $E_1 + \Delta_1$ and E_1 transitions respectively, Δ_1 is the split-off energy and $d\chi/d\omega$ is the derivative of the susceptibility function with respect to the frequency. The first term involves electron and hole transitions among three bands (the two split-off valence bands and the conduction band), while the second term is given by a two band process, in which only one interband transition occurs (from valence to conduction) together with another transition in the same band [148]. The susceptibility is related to the dielectric function by the relation $\varepsilon = \varepsilon_0(\chi + 1)$. Therefore, in the two above equations the susceptibility can be directly substituted by the dielectric function. From theoretical calculations [137], in Ge the first term is dominating on the second one due to the ratio between the deformation potentials ($d^5_{3,0}/d^5_{1,0} \approx 5$). By neglecting the second term, the Raman efficiency data can be interpreted by means of the comparison to the quantity $|\varepsilon^+ - \varepsilon^-|^2$. This was done in [137]. The two functions ε^+ and ε^- must be available: in the case of Ge, they were experimentally determined by Sell and Kane [149] by means of piezoreflectance measurements. In Si, on the other hand, the split-off energy Δ_1 is small enough to allow approximating also the first term with the derivative of the susceptibility, so that we obtain:

$$\partial\chi \propto \left(\frac{\sqrt{2}}{\sqrt{3}} d^5_{3,0} + \frac{d^5_{1,0}}{2\sqrt{3}} \right) \frac{d\chi}{d\omega} \tag{4.35}$$

and the variation of the susceptibility is simply proportional to its derivative with respect to the frequency. The dielectric function of Si as a function of frequency has been accurately measured by means of optical ellipsometry: its derivative can be easily calculated from the experimental data, and its square modulus can be used to interpret the Raman resonance data, as it was done in [136].

In $Si_{1-x}Ge_x$ we can reasonably expect an intermediate situation between the two above cases: the two terms in equation 4.34 will progressively change their

respective weight, depending on the alloy composition. An accurate treatment of how these modifications occur is however extremely difficult, and would require a specific investigation which is beyond the scope of this work.

An approximated evaluation of equation 4.34 was carried out, through the relation:

$$\varepsilon^{+}(\omega) = \varepsilon^{-}(\omega + \Delta_1)$$

similarly to what Sell and Kane state in their work [149]. Under this assumption, a second approximation follows:

$$\frac{2(\varepsilon^{+}(\omega) - \varepsilon^{-}(\omega))}{\Delta_1} \approx \frac{2(\varepsilon^{-}(\omega + \Delta_1) - \varepsilon^{-}(\omega))}{\Delta_1} \approx \frac{d\varepsilon}{d\omega}$$

so that we come back to a form similar to equation 4.35. Therefore, within this approximation, we only need the dielectric function $\varepsilon(x,\omega)$ of $Si_{1-x}Ge_x$ and the deformation potentials. We finally choose to directly compare our experimental results with the square modulus of the dielectric function, neglecting the composition dependent modulation given by the deformation potentials. The values of the real and imaginary part of the dielectric function were taken from the work of Humlicek et al. [15]. In figure 4.12 the Raman efficiency data are again plotted in logarithmic scale, with the solid curves representing the semiempirical quantity $|d\varepsilon/d\omega|^2$. All the solid curves are rescaled to the experimental data with the same factor.

Figure 4.12 shows that this approximated approach still gives a satisfactory explanation of the observed features in the Raman efficiency: the position of the peaks is satisfactorily reproduced, as well as the ratios between the resonance peak heights in Si and Ge-rich alloys, while a major difference is observed for 2.71 eV. All the discrepancies are within a factor 2, which is reasonable when considering the uncertainties on the plotted quantities and the approximations taken in this treatment. Similar discrepancies can be observed also in the work about Si by Renucci et al. [136]. The larger resonance effect in Si is well explained now by considering again the plots of the dielectric function reported in figure 4.2: the structure due to the E_1 and $E_1 + \Delta_1$ direct electronic transitions simply shifts in energy with varying alloy composition up to $x \approx 0.2$, then it becomes higher and sharper. This leads to an increase in the square modulus of the derivative of the dielectric function which gives a good description of the change in the Raman resonance peak height.

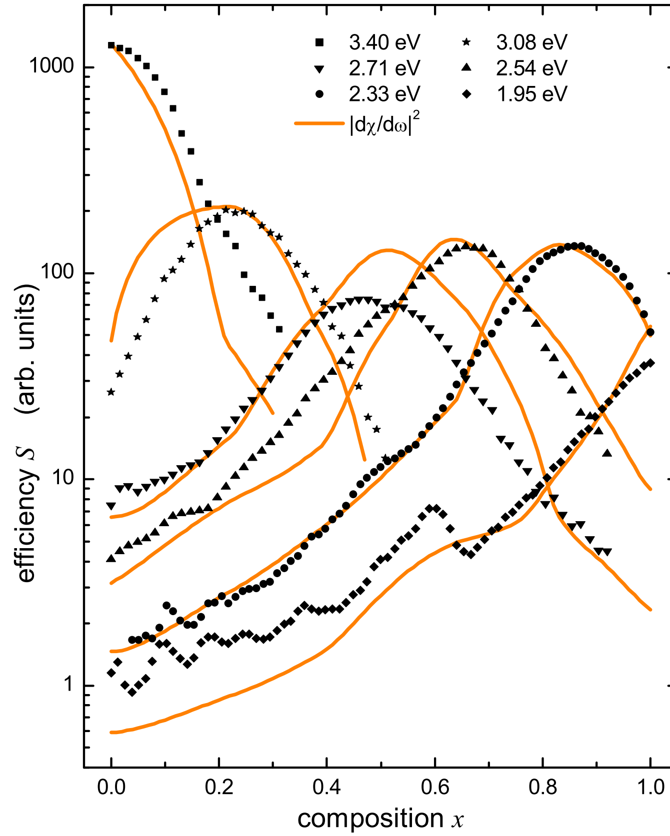

Figure 4.12: Raman efficiency of SiGe as a function of the alloy composition x and the excitation light energy, together with the semiempirical calculation of $|\partial\chi/\partial\omega|^2$ (solid lines), which approximates the square modulus of the quantity given by equation 4.34. The solid lines are rescaled to the experimental data by the same factor.

Finally, the comparison with the theory is able to give a confirmation of the validity of the procedure for the data elaboration, with particular reference to the correction for the penetration depth of the light in the alloy (especially at low values of the composition and low energy, see section 4.3.5): actually, the resonance curves follow quite well the theoretical behaviours for $x < 0.5$ for mostly all the values of the excitation light energy. The agreement at 2.33 eV is remarkable. This confirms the validity of the fitting curves plotted in figure 4.7.

4.4.2 Results of the approximated data elaboration

In this section the results of the approximated data elaboration mentioned in section 4.3.5 are shown and compared to the data reported above. We remind that the approximation lies in neglecting the presence of a different Bose factor and phonon frequency for each of the three $Si_{1-x}Ge_x$ phonons, which is equivalent to considering each $Si_{1-x}Ge_x$ Raman spectrum as a lineshape function with unitary area multiplied by a overall intensity factor. This intensity, corrected for the parameters listed in section 4.3.5, gives the results displayed in the following figures. Figure 4.13 shows the resonance curves in logarithmic scale, analogously to figure 4.12, with the same theoretical curves. As a consequence of neglecting the difference between the correcting factors for each different phonon, the experimental curves are raised for Ge-rich alloys and lowered for Si-rich ones. The matching between theory and experiment is still satisfactory: the ratios between the resonance peak heights do not change considerably, while the positions of the resonance bands do have a small variation. The matching with the $E_1/E_1+\Delta_1$ direct electronic transitions is still very good.

4.4.3 Single Raman mode analysis

So far, the analysis of the Raman efficiency has been carried out by considering the sum of the intensities of the three $Si_{1-x}Ge_x$ Raman peaks; it is also interesting to see the behaviour of each single peak: we report here, as an example, the measurement of the Raman efficiency at 2.71 eV excitation light energy. The intensity of each Raman mode is considered separately and corrected for the factors listed in section 4.3.5: in figure 4.14, panel (a), the obtained Raman efficiency is plotted separately for each Raman mode, together with the sum of the three, giving the total Raman efficiency. Each Raman mode exhibits a resonant behaviour: however, the resonance occurs at slightly different values of the alloy composition. Actually, the intensity of each mode depends on the alloy composition through the number of the respective atom pairs which can be found in the material: the Si-Si, Si-Ge and Ge-Ge mode intensities are then proportional to $(1-x)^2$, $2x(1-x)$ and x^2 respectively. Panel (b) of figure 4.14 shows the same resonance curves reported in panel (a), divided by the three factors listed above. As expected, the maxima of the curves are found at the same value of the alloy composition.

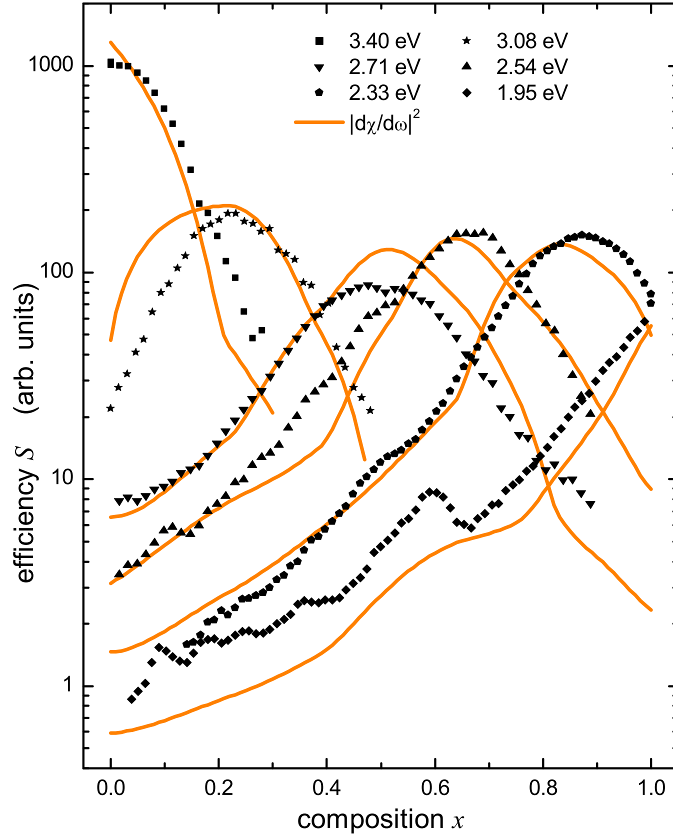

Figure 4.13: Raman efficiency of SiGe as a function of the alloy composition x and the excitation light energy, as given by the approximated approach which neglects the difference in the Bose factor for the three Raman peaks of SiGe. The solid curves give again the semiempirical calculation of $|\partial\chi/\partial\omega|^2$ (solid lines).

4.5 Raman experiments on inhomogeneous samples

In the following sections we will show and examine the results of several Raman experiments carried out on inhomogeneous nanostructured $Si_{1-x}Ge_x$ samples, in particular $Si_{1-x}Ge_x$ islands grown with different growth parameters and substrates. The effect of the Raman resonance in these systems will be highlighted: it will be shown how the knowledge of the Raman efficiency can help the experimenter have a deeper understanding of the Raman spectra and individuate which information can be extracted.

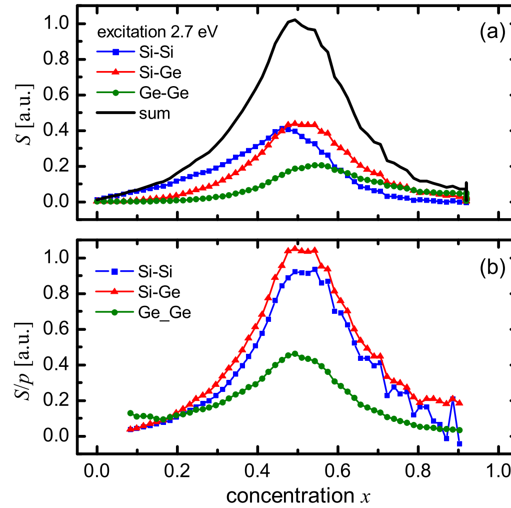

Figure 4.14: Panel (a): Raman efficiency for the three SiGe Raman modes, considered separately. Panel (b): the curves reported in panel (a) are corrected for the probability p of finding Si-Si, Si-Ge or Ge-Ge atom pairs in the material, as a function of the composition: $p_{Si-Si} = (1-x)^2$; $p_{Si-Ge} = 2x(1-x)$; $p_{Ge-Ge} = x^2$.

4.5.1 Multiwavelength analysis of SiGe islands

The first case study is given by an ensemble of $Si_{1-x}Ge_x$ islands grown randomly on a flat p-Si (001) substrate by Stranski-Krastanov process (see section 2.2.1). The substrate was cleaned and covered by a 100 nm thick Si buffer grown by MBE. Then 8.7 monolayers of pure Ge were deposited by MBE at 700 °C: dome-shaped islands were obtained with diameter about 150 nm, height 35 nm, and a density on the sample surface of 10 islands per square micron circa. Finally, the sample was exposed to a sequence of chemical baths in a selective etchant solution of NH_4OH and H_2O_2 (according to the recipe given in [85]): the $Si_{1-x}Ge_x$ islands were therefore progressively etched, as it is shown by the AFM profiles displayed in panel (a) of figure 4.15.

Raman spectra were measured on the freshly grown sample and after each etching step, with excitation light at four different wavelengths: 364 nm (3.40 eV), 458 nm (2.71 eV), 532 nm (2.33 eV), and 633 nm (1.96 eV). The Raman spectra are shown in panels (b), (c), (d) and (e) of figure 4.15. Same colours in figure 4.15 are related to the same etching time.

The spectrum of the sample changes noticeably under the variation of the ex-

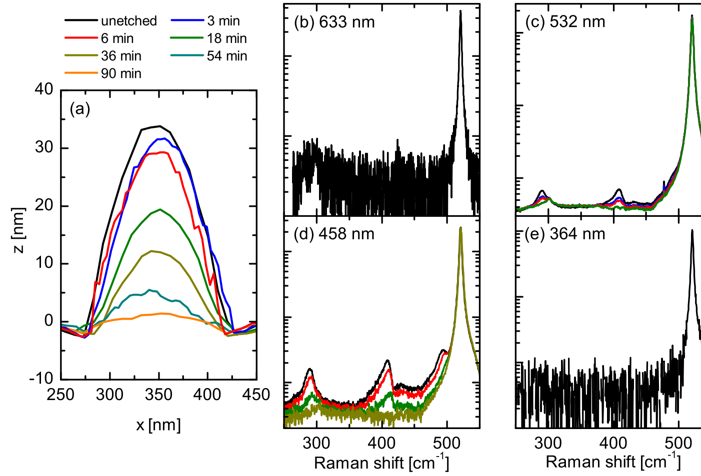

Figure 4.15: Raman experiments on self assembled SiGe islands. Panel (a): AFM profiles of the islands after several etching steps. Panels (b)-(d): Raman spectra of the sample taken at four different wavelengths. Same colours in the figure refer to the same etching step.

citation light wavelength. An intense peak located at 520.7 cm^{-1} is present in all the spectra: this is the signal coming from the Si substrate. The first important observation is that the signal from the islands is visible only under 532 and 458 nm excitation light: three peaks can be individuated, located as usual near 300, 400 and 500 cm^{-1}. Their amplitude is between 2 and 3 orders of magnitude lower than the substrate signal (note the logarithmic scale on the y-axis); however, the ratio between the two signals is clearly higher at 458 nm than at 532 nm. In the first case, actually, it is also possible to resolve the two Si-Si peaks belonging to the island and the substrate Raman spectra: at 532 nm, the Si-Si peak coming from the islands is only a shoulder on the more intense Si bulk peak. On the other hand, no contributions to the Raman spectrum coming from the $Si_{1-x}Ge_x$ islands are observed both at 633 and 364 nm, even on the unetched sample. Only two very feeble peaks might be individuated near 300 cm^{-1} in panel (b), but the s/n ratio is too bad to give safe considerations. In any case, the difference with respect to panels (c) and (d) is evident.

A second source of information is the change in the Raman spectra as the etching proceeds. Obviously, only the spectra taken with 458 nm and 532 nm excitation light wavelength will be considered. In general, as can be expected, the

intensity of the island Raman signal decreases as the etching proceeds. However, the decay of the signal seems to be faster with the excitation at 532 nm than with the 458 nm. Moreover, it is not proportional to the decrease of the volume of the islands: this could be due to a variation of the composition inside the island.

From the direct observation of the position of the peaks, an average alloy composition about 0.4 is obtained. The inspection of the Raman efficiency curves reported in section 4.4 gives an immediate qualitative explanation of the major features in the signal intensities. Actually, at $x \approx 0.4$, the maximum efficiency corresponds exactly to the 458 nm excitation; then, the 532 nm follows, but with almost one order of magnitude of difference. The 633 nm excitation wavelength gives a Raman efficiency even lower, and not so different from pure Si; finally, at 364 nm, the efficiency in pure Si is much higher than at $x = 0.4$, for two orders of magnitude: this suggests that the signal from the Si substrate will be much more intense with respect to the islands one.

More quantitative considerations, in which all the factors listed in section 4.3.1 are taken into account, can be given by the simulation of the Raman spectra, considering the data presented in the previous sections. Figure 4.16 shows the comparison between the experimental and the simulated spectra of the structures: the simulation is carried out with the method which will be explained in detail in section 5.2. In order to have a realistic simulation of the sample, the size and surface density of the islands were taken into account: they were obtained from the AFM images of the sample. About the internal composition profile of the islands, we make an anticipated use of the results which will be presented in detail in sections 5.4.1 and 5.4.2. The spectra are simulated both for the entire and the etched islands: this can be numerically achieved just by removing the topmost layers in the simulated structure. The agreement between the experimental and the simulated data is quite good: the absence of detectable signal from the islands at 633 and 364 nm is explained, and the difference between the signals at 458 and 532 nm wavelength is well reproduced. This gives a confirmation of the validity of our data: a further discussion on the internal composition profile and the etching process will be given in section 5.4.2.

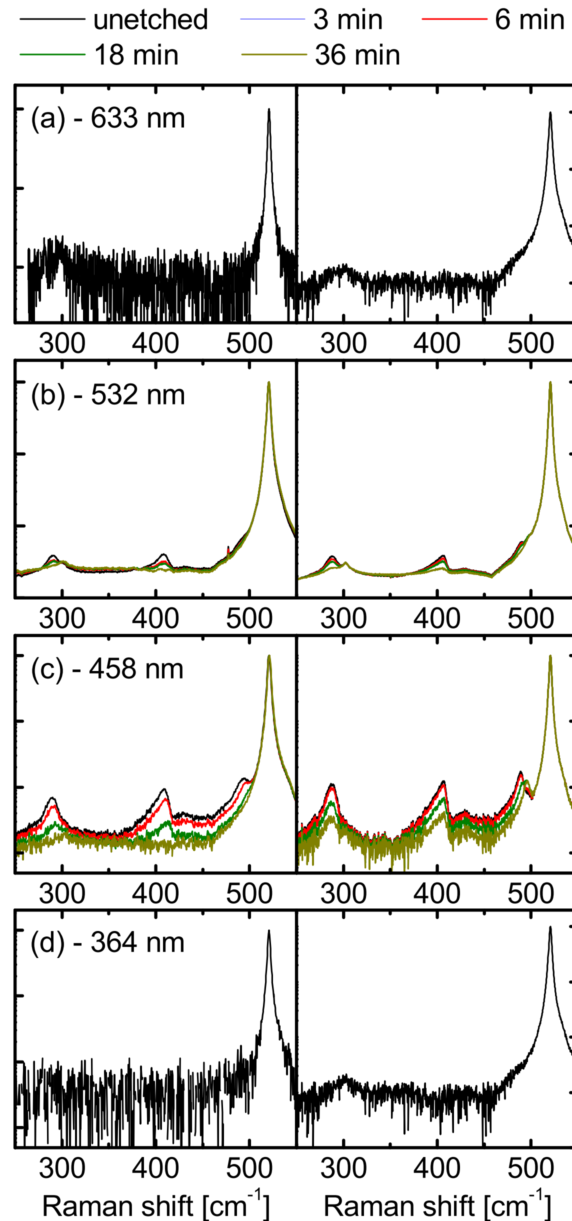

Figure 4.16: Experimental (left) and simulated (right) Raman spectra of self assembled SiGe islands, with diameter, height and surface density given by the AFM measurements of the sample. The internal composition profile of the islands obtained in chapter 5 has been used. All the spectra are normalized in order to allow a direct comparison. The noise in the calculated spectra is given by the fact that *experimental* spectra of $Si_{1-x}Ge_x$ are weighted and summed in the spectral simulation (see section 5.2).

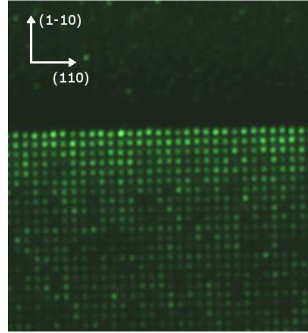

Figure 4.17: Optical image of the sample of SiGe islands grown on a pit patterned Si substrate.

4.5.2 Strain induced by SiGe islands grown on patterned substrates

Another interesting case is a sample of ordered $Si_{1-x}Ge_x$ islands grown on a patterned Si substrate. Squared patterns of pits (figure 4.17) were fabricated by electron beam lithography (EBL) followed by wet etching on a (001) Si substrate [150]. The distance between the pits was 800 nm. The pits were smoothed with the growth of 22 nm of pure Si; then, 12 MLs of pure Ge were deposited by MBE at 700 °C. On the basis of the growth parameters, the $Si_{1-x}Ge_x$ alloy on the islands is expected to be about 0.4 in composition.

In this case, several 2D Raman mappings of the sample were performed, with excitation at two different wavelengths, namely 458 nm and 364 nm. The use of these wavelengths allows probing selectively different parts of the sample, which we can individuate on the basis of the knowledge of the Raman efficiency. The first excitation (458 nm), as it was confirmed by the results of the previous section, is able to enhance the signal coming from the islands, thus providing useful structural information. The second excitation (364 nm) is able to probe a very thin layer of the Si substrate, while suppressing the signal coming from the islands: actually, the $Si_{1-x}Ge_x$ islands are out of resonance and they do not contribute to the Raman signal. Therefore, from these measurements, it was possible to measure the compressive strain in the Si substrate induced by the presence of the islands in the pits. The short penetration of the UV light in silicon provides a high sensitivity to the strain in the surface layers.

The Raman maps measured with the 458 nm excitation light wavelength are

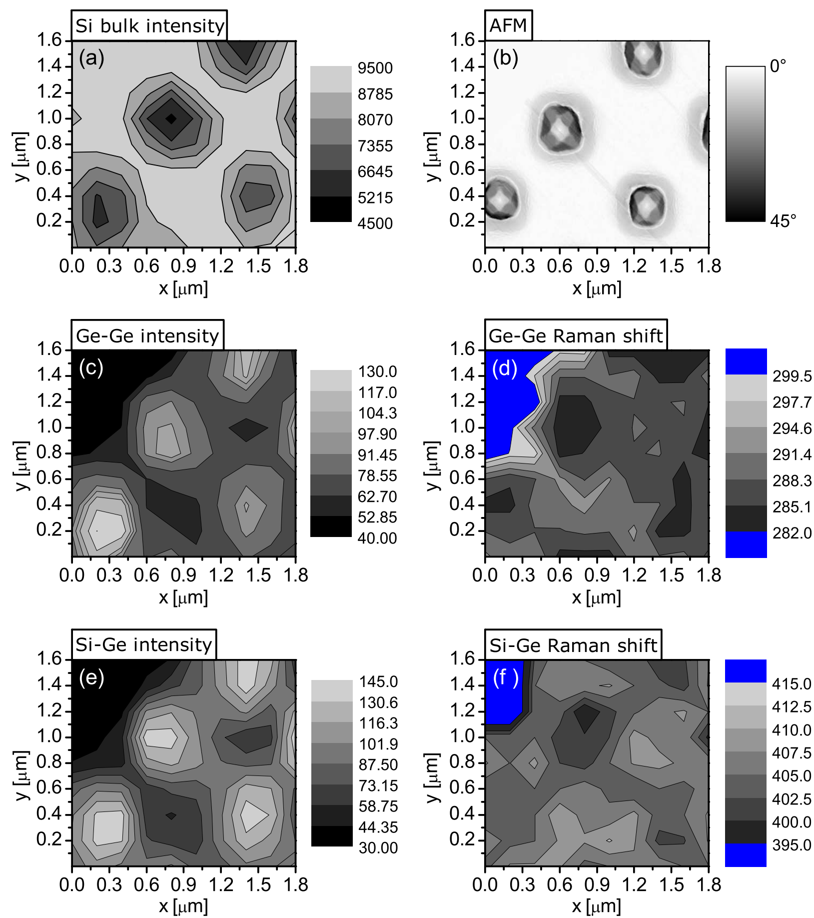

Figure 4.18: Raman maps of SiGe islands grown on a pit patterned substrate, illuminated with 458 nm excitation light. Panel (a): intensity of the Si bulk Raman peak; panel (b): AFM image of a region of the sample with the same dimensions of the Raman maps. Panels (c), (d) and (e), (f): intensity and frequency of the Ge-Ge (Si-Ge) Raman peaks related to the islands.

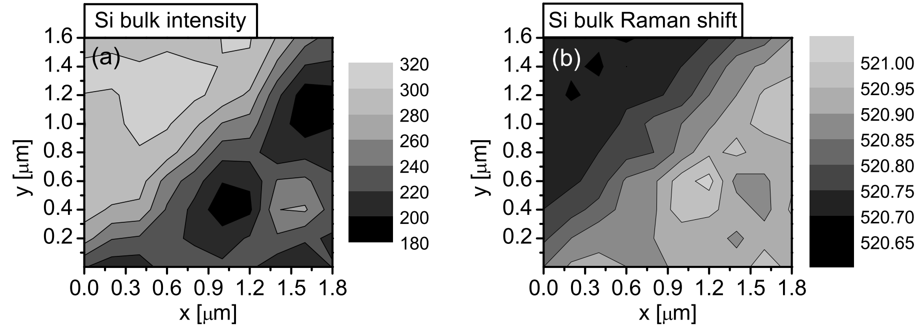

Figure 4.19: Raman maps of SiGe islands grown on a pit patterned substrate, illuminated with 364 nm excitation light. Only the signal coming from the Si substrate is visible in this case, due to the resonance conditions. In particular, a very thin (10 nm) layer of the Si substrate contributes to the Raman emission. Corresponding modulations of the intensity and frequency of the bulk Si Raman mode are clearly visible. The frequency of the Raman peak was obtained by a fitting procedure which allows detecting very small variations of the peak frequency (down to 0.02 cm^{-1}).

displayed in figure 4.18. The scanning step was 200 nm. The sample was rotated and analyzed in HV polarization configuration in order to suppress the contribution from the 2TA Raman mode of the Si substrate [151]. In figure 4.18 the Raman maps obtained from the plot of the intensity and the position of the main Raman peaks found in the spectra are compared to the AFM image of the sample, in panel (b). Minima in the signal from the Si substrate correspond to maxima in the signal from the islands, due to the optical absorption in the islands. Figure 4.18 demonstrate the possibility of spatially resolving the islands on the substrate surface, and this gives the opportunity of studying separately each single dot by Raman spectroscopy. From the frequency of the island Raman peaks, a composition value about 0.36 ± 0.03 is obtained, and a strain value compatible with 0 within the experimental uncertainty.

Figure 4.19 shows the Raman map of the sample illuminated with UV excitation light: the probed area is close to the border of the patterned zone. In this case no signal from the islands was detected, and their presence is revealed by the minima in the Raman signal from the Si substrate (panel (a)). In panel (b), a map obtained by plotting the position of the Si bulk Raman peak is shown: a

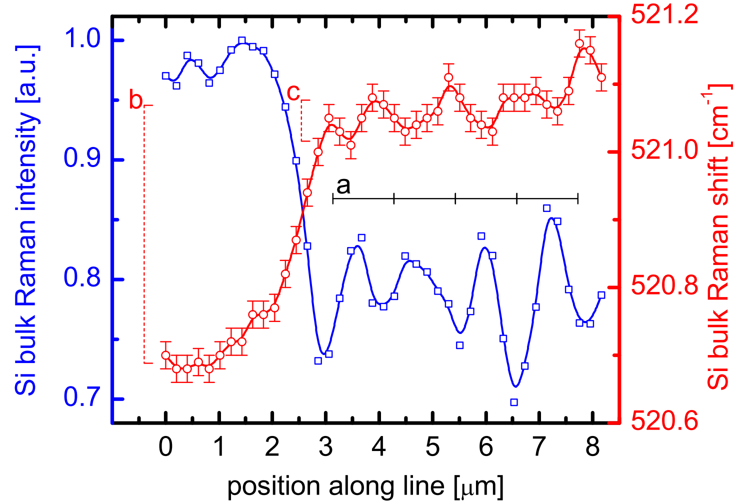

Figure 4.20: Raman line scan of the sample, along the [100] direction, entering the patterned zone. The Raman peak of the bulk Si shifts toward higher Raman shift values, which is indicative of the presence of compressive strain around the islands. The bar named (a) gives the distance between the islands given by the pattern lattice parameter along the [100] direction; the red and blue points are the experimental data about the Raman shift and the intensity of the Si bulk peak. The lines (b) and (c) are interpolations of the experimental data.

modulation of the Si Raman peak frequency exists, with maximum displacements placed in correspondence to the positions of the islands. The small differences in the peak frequency (in the order of 0.05 cm^{-1}) were detected by fitting the Si-Si peak with a Voigt function. The shift of the Si bulk peak in the patterned area is toward higher values of the Raman shift, corresponding to compressive strain.

A more quantitative information is given in figure 4.20, which displays a line scan performed on the same sample with 364 nm excitation light, taken along the [100] direction: the line started from the unpatterned region and ended in the area occupied by the islands. The frequency of the Si bulk peak outside the patterned area corresponds to null strain. An average compressive strain around 0.05% is present in the pattern, with the tendency to increase as we move inside. As usual, the strain is considered symmetric and biaxial in the growth plane. The corresponding stress $\sigma_{xx} + \sigma_{yy}$ is in the order of 180 MPa. The islands give an additional contribution to the strain in their immediate neighborhood about 0.007%, corresponding to a stress about 25 MPa.

4.5.3 Strain in the Si cap layer

The Raman resonance in Si at 3.40 eV, together with the short penetration depth ($\approx$ 10 nm) allows also characterizing the strain of a thin Si cap layer deposited on top of self assembled $Si_{1-x}Ge_x$ islands. A sample of randomly nucleated $Si_{1-x}Ge_x$ islands grown by MBE deposition of 6.7 MLs Ge at 620 °C on a flat Si(001) substrate was capped by 5, 10, and 20 nm of pure Si: the cap was also grown by MBE, at low temperature (300 °C) in order to prevent intermixing. The islands are domes with base diameter about 90 nm, and height about 20 nm; 10 structures are probed simultaneously for a laser spot diameter in the range of 1 μm.

The Raman spectrum of the sample (panel (a) in figure 4.21) is dominated as usual by a strong Si bulk peak coming from the relaxed regions of the Si cap: in particular, these regions correspond to the free areas of the substrate between the islands. Differently from the patterned sample analyzed in the previous section (4.5.2), here the islands are small and distanced enough to allow relaxing the strain in the substrate regions around them. In addition to the bulk peak, a minor structure is observed at substantially lower Raman shift (see the inset in figure 4.21 for details): this minor band progressively moves toward the Raman peak of Si as the cap thickness increases. According to the resonance conditions and the cap thickness, it is clear that this band at lower Raman shift cannot be related to the $Si_{1-x}Ge_x$ alloy of the islands: a confirmation to this consideration comes also from the spectrum of the uncapped sample (labelled as 0 nm in figure 4.21): no differences with respect to the bulk Si signal are detected, as it was expected. Therefore, it is evident that the $Si_{1-x}Ge_x$ alloy in the island is not responsible for the existence of the small band in the spectra of the capped samples.

Therefore, the only explanation for the presence of the secondary Raman band relies in the presence of highly stressed areas in the Si cap. In particular, the strain seems to be tensile, which is consistent with the predicted effect of the buried $Si_{1-x}Ge_x$ island. In order to better put in evidence the signal from the cap, the spectrum of a bulk Si sample was subtracted: the results of the spectral subtraction are plotted in panel (b) of figure 4.21. As the thickness increases, progressive elastic relaxation in the Si cap shifts the Raman signal towards the Si bulk Raman frequency. In the subtracted spectra, some subtraction artifacts appear in the

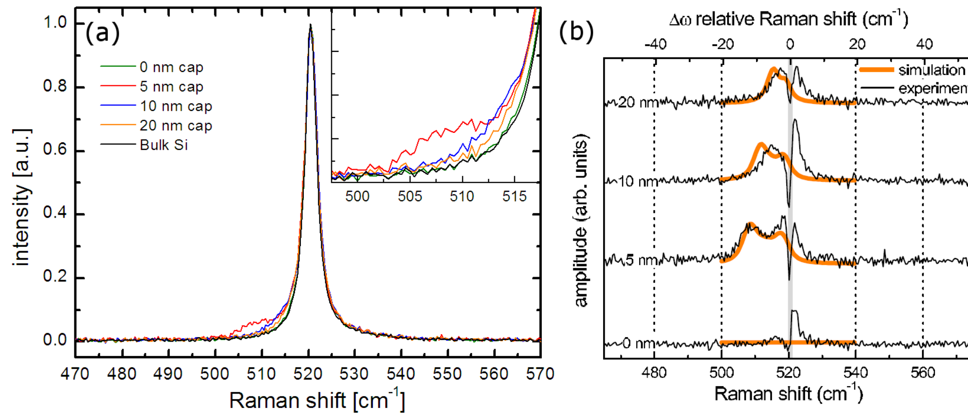

Figure 4.21: Panel (a): Raman spectra of self assembled $Si_{1-x}Ge_x$ islands capped with a thin Si cap, with different thickness. The 0 nm label refers to uncapped islands. A Raman band (details in the inset) is observed at lower Raman shift with respect to the Si bulk, coming from tensily strained areas in the cap. Panel (b): the Si bulk spectrum was subtracted from the spectra in panel (a), evidencing the Raman signal of the cap. High strain is obtained in the 5 nm Si cap. The orange lines show the results of the Finite Element Model simulation of the strain in the cap (see the text).

vicinity of 520.7 cm^{-1}: they are generated by very small differences in the intense signal from the Si bulk. Though very small compared to the intensity of the Si bulk, they result comparable to the intensity of the strained Si areas on top of the islands. Therefore, the spectral structures in the vicinity of the original position of the Si bulk peak should be not considered meaningful. In particular, the spectral region of the artifacts was estimated to be in the range 520.7 ± 5.0 cm^{-1}. Outside this range, the observed spectral structures can be safely considered as real. For the 5 nm cap thickness, the Raman band is located at 508 cm^{-1}: if the calibration given in section 3.5 is used (planar and uniform strain approximation), this shift corresponds to a really high strain value about 0.017. However, this approximation can be rigorously applied only on the (001) top facet, which contributes to the total area only for a small fraction. In a more realistic picture, also the other facets contribute to the spectrum with their Raman spectra: a complex strain distribution is found on these facets, and also a change in the Raman selection rules is expected due to the different facet inclination. Actually, due to the facet orientation, the eigenvectors of the matrix representing the secular equation

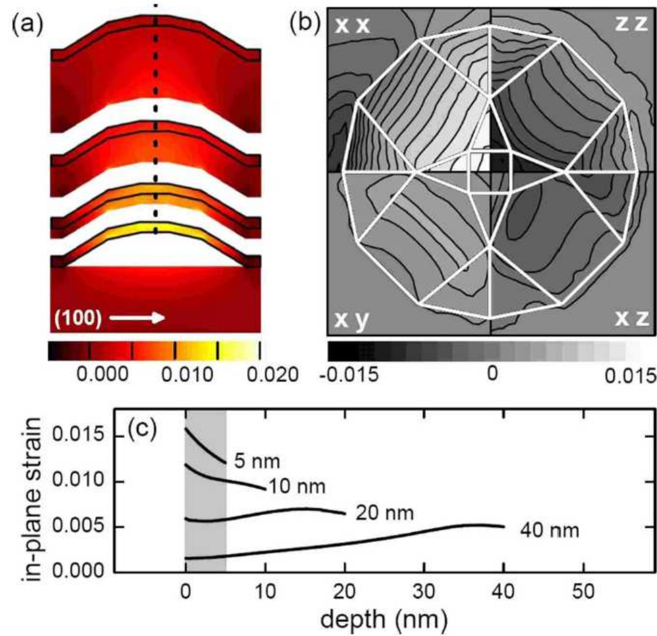

Figure 4.22: Panel (a): FEM simulation of the strain in the Si cap for several values of the thickness. The black line evidences the region of the top layer probed by UV Raman, while the island is not shown for clarity. The composition inhomogeneity in the island was neglected, setting the alloy composition to an average value $x_{av} = 0.6$. Panel (b): top view map of the average strain in the 5 nm Si cap: the four independent components of the strain are plotted. The lower edge is parallel to [100]; the island facets (dome shape) are also reported. Panel (c): plot of $(\varepsilon_{xx} + \varepsilon_{yy})/2$ as a function of the depth in the Si cap. The shaded region evidences the probed portion of the sample. From [76].

(see expression 4.10) will change: consequently, the Raman tensors will be modified according to equation 4.17. Differently from the case of a flat (001) strained plane, not only one phonon is detectable, but also the other two can contribute to the Raman spectrum.

In order to better understand the role played by the complex shape of the islands in the Raman measurements, Finite Element Model (FEM) simulations of the strain in the Si cap (figure 4.22) and of the expected Raman spectrum associated to the simulated strain field (orange lines in figure 4.21, panel (b)) were performed. The details can be found in [76]. Panel (a) in figure 4.22 shows the strain (expressed as $\varepsilon_{xx} + \varepsilon_{yy}$) in cross view for several values of the cap thickness. The black line at the cap surface diplays the thin region of the Si layer probed by

UV Raman. Panel (b) reports the four nonzero components of the strain in the 5 nm thick cap layer, averaged with respect to the thickness, and plotted in top view together with the island facets. Panel (c) shows again the quantity $\varepsilon_{xx} + \varepsilon_{yy}$ as a function of the depth in the cap layer. The strain in the first 5 nm of the cap is progressively released as the cap thickness increases, due to elastic relaxation.

The secular equation 4.10 was then solved considering the calculated strain field. In order to partially simplify the problem, the strain was averaged on each facet and considered biaxial in the plane of the facet. The secular equation was solved, the Raman tensors were obtained for each facet, and the Raman selection rules were applied. In particular, the three phonon eigenvectors are still perpendicular one to each other: two phonon eigenvectors are degenerate and lie in the facet plane (they will be referred to as $\mathbf{P}_1$ and $\mathbf{P}_2$). The third phonon, $\mathbf{P}_\perp$, is perpendicular to the facet plane. The two degenerate eigenvectors can be choosen arbitrarily in the facet plane. It is convenient to take one always perpendicular to the [001] direction. Actually, in a Raman experiment performed in the usual $\mathbf{z}(-,-)\bar{\mathbf{z}}$ configuration, this phonon is always silent (we remind that in this configuration the selection rules make visible only the phonons which have a nonzero component along $\mathbf{z} = [001]$), and only the other two phonons have to be considered. The Raman spectrum of the strained cap was finally simulated by adding several Lorentzian peaks shifted by the amount obtained from the eigenvalues of secular equation and weighted by considering the selection rules. In particular, the intensity related to the out of plane phonon $\mathbf{P}_\perp$ is maximum at the top facet, and progressively decreases on the steeper facets, consistently with the decrease in its z-component. For the in plane visible phonon ($\mathbf{P}_2$, for example) the intensity is higher on the steeper facets, while it is zero at the top. The calculated Raman spectrum, rescaled in intensity in order to be comparable to the experimental data, is plotted as an orange line in panel (b) of figure 4.21.

The agreement between theory and experiment is good, especially for the 5 nm thick cap. Two splitted bands are predicted by the calculation, but only one can be experimentally observed: this is due to the fact that the other band falls within the region of the spectral artifacts (or, equivalently, it is superimposed to the much more intense Si bulk signal). The observable band, more shifted toward low Raman shift, is also relatively more intense: it turns out to be related to the $\mathbf{P}_\perp$ phonon, i.e. the phonon whose intensity is maximum on the top facet of the

island. The second band, on the other hand, is linked to the $\mathbf{P}_2$ phonon. The shift of the $\mathbf{P}_\perp$ band with the increasing cap thickness is nicely reproduced, thus validating the FEM simulations of the strain in the cap and confirming the elastic relaxation mechanism of the strain.

As a result, it is found that a more accurate relationship between the average strain in the facets and the shift of the Raman band can be obtained by considering a modified strain coefficient $b_{island} = 1300$ cm^{-1} rather than the usual value $b =$ 750 cm^{-1} reported in section 3.5. In any case, in the cap with 5 nm thickness the average strain in the cap is still substantial, being about 0.01. These results, obtained in the framework of the dotFET project [65] gave the confirmation of the possibility of fabricating highly stressed Si films on top of $\mathrm{Si_{1-x}Ge_x}$ islands for the fabrication of high mobility MOSFETs.

Chapter 5

Raman analysis of inhomogeneous samples

In this chapter, a novel methodology will be presented for the analysis of inhomogeneous $Si_{1-x}Ge_x$ nanostructures, with two aims: the first consists in individuating which values of the alloy composition are present in the sample, and how much they contribute to the Raman spectrum; the second consists in finding the composition profile inside the nanostructures. In the next sections, the numerical procedure will be outlined. Then, it will be applied to a calibrated inhomogeneous sample, namely a stack of $Si_{1-x}Ge_x$ layers with different composition and well controlled thickness, in order to check the reliability of the method. Finally, the numerical method will be used in order to study the $Si_{1-x}Ge_x$ islands presented in the previous chapter. Remarks about the limitations and the domain of applicability of the method will be given in the end.

5.1 Spectrum analysis

The starting point is given by the observation that the Raman spectrum of an inhomogeneous $Si_{1-x}Ge_x$ structure can be imagined as the superposition of spectra originating from several regions of the sample, each one characterized by a different value of the alloy composition. In most cases the different spectra constituting the total Raman spectrum cannot be resolved individually, in particular when a smooth variation of the alloy composition is present in the volume probed by

Raman spectroscopy: in this case, a broadening of the Raman peaks is observed, more or less extended depending on the variation of the composition in the probed volume of the sample. However, if the shape of the spectra related to all the different values of the composition were known *a priori*, it could be possible to find a weighted sum of spectra which is able to approximate the experimental result. This would give information about which values of the alloy composition are present in the probed volume, and how much they contribute to the spectrum.

A wide set of Raman spectra, each one related to a different value of the alloy composition, is provided directly by the same experiment carried out for the measurement of the $Si_{1-x}Ge_x$ Raman efficiency. Our basic assumption, then, is that any experimental Raman spectrum $\Phi(\omega)$ of an inhomogeneous $Si_{1-x}Ge_x$ sample can be written as linear combination of these spectra. In particular, we choose 21 spectra $\phi_x(\omega)$, $x = 0, 0.05, 0.1, ..., 1$, and we normalize them in arbitrary units according to the relation:

$$\int_R \phi(\omega) d\omega = 1 \tag{5.1}$$

where R is a spectral range including all the Raman peaks. We also include a normalized flat spectrum $\phi_o = 1/R$ in order to take account of offsets in the experimental spectra. Then, we write:

$$\Phi(\omega) \approx \sum_{x=0}^{x=1} a_x \phi_x(\omega) + a_o \phi_o \tag{5.2}$$

where the a_x and a_o are real and positive coefficients. We also define an integral inner product between any two spectra ξ and ψ defined on R:

$$\langle \xi | \psi \rangle_{R'} = \int_{R'} \xi(\omega) \psi(\omega) d\omega \tag{5.3}$$

where $R' \subseteq R$. Then, we take the inner product of both the terms in equation 5.2 with all the ϕ_x and ϕ_o functions (indexed by a single index k or l):

$$\langle \phi_l | \Phi \rangle_{R'} \approx \sum_k a_k \langle \phi_l | \phi_k \rangle_{R'} \tag{5.4}$$

obtaining an equation with the form:

$$b_l \approx S_{lk} a_k \tag{5.5}$$

in which $b_l = \langle \phi_l | \Phi \rangle_{R'}$, and the matrix S_{lk} is given by $\langle \phi_l | \phi_k \rangle_{R'}$. In practice, these terms can be calculated easily by applying equation 5.3 to the experimental spectra. In equation 5.3, the integration domain can be restricted to a range R' in order to analyze a particular region of the spectrum. The best approximation of Φ as a sum of the functions ϕ is found by looking for the set of coefficients a_k which minimize the euclidean distance between the vectors b_l and $S_{lk}a_k$, under the constraint $a_k \geq 0 \forall k$. This step can be achieved by using the solving algorithms for the solution of the so-called "Non Negative Least Squares problem"(NNLS) [152]: an implementation is available in MatLab.

The quality of the result of the spectral decomposition can be checked directly by comparing the original spectrum $\Phi(\omega)$ with the reconstructed spectrum $\sum a_k \phi_k(\omega)$.

The procedure outlined in this section is able to translate an experimental spectrum into a set of 21 (plus the offset) coefficients, each one related to a different value of the alloy composition. This is already a source of useful information: actually, from the intensity of each component, it is possible to have a first picture about the extension of the composition inhomogeneity inside the probed volume, an information which is not straightforwardly accessible by looking directly to the total spectrum. The typical results of the application of this numerical tool to several experimental spectra of $Si_{1-x}Ge_x$ hetero and nanostructures will be shown in the next sections. From the normalization condition of equation 5.1, it follows that the intensity of the experimental spectrum, integrated on the spectral range R, is given by:

$$I = \int_R \Phi(\omega) d\omega \approx \sum_{x=0}^{x=1} a_x + a_o \tag{5.6}$$

5.2 Composition profiling

Our aim is now to use the information of equation 5.6 to reconstruct a profile of the composition in the nanostructure investigated. We take into consideration again equation 4.23, and write the intensity of the Raman signal given by a homogeneous sample with thickness D:

$$I = \eta \cdot I_0 \cdot \left[S \cdot \frac{\left(1 - e^{-2D/L}\right)}{2} L \cdot T^2 \right] \tag{5.7}$$

where S and L are the Raman efficiency and the penetration depth of the light in the material, respectively, I_0 is the intensity of the light impinging on the sample, and η is the efficiency of the collecting optical system.

In the following, we are going to develop a method which approximates the nanostructures as they were formed by layers with homogeneous composition; we will show later that this approximation can be successfully applied, for example, to $Si_{1-x}Ge_x$ islands. An inhomogeneous $Si_{1-x}Ge_x$ structure can therefore be considered as a stack of n layers with different alloy composition x_j and thickness D_j. We choose to count the index j starting from the topmost layers. The intensity of the Raman spectrum will be given by the sum of the intensities of each layer:

$$I = I_1 + I_2 + \ldots + I_n \tag{5.8}$$

For the j-th layer, the formula given in 5.7 must be corrected for the attenuation of the light given by the layers above. This is achieved simply by the substitution of the quantity I_0 with the attenuated intensity I_{j0} given by:

$$I_{j0} = I_0 \cdot \sum_{k=1}^{j-1} e^{-2D_k/L_k} \tag{5.9}$$

where the D_k and the L_k are the thickness and the penetration depth of the light in the first $j-1$ topmost layers. In general, also the reflections at the interfaces between the layers should be considered; however, for two adjacent $Si_{1-x}Ge_x$ layers, the trasmission coefficient is very close to 1 for any couple of values of the alloy composition in the optical-UV range (for a Si/Ge interface, $T \geq 0.95$ for any wavelenght between 633 and 364 nm, as can be calculated from the values of the optical functions [146]): therefore, the contribution of the internal reflections can be discarded. The total intensity of the Raman spectrum is given by a sum of terms of the form:

$$I_j = \eta \cdot I_0 T^2 \cdot \sum_{k=1}^{j-1} e^{-2D_k/L_k} \cdot \left[S_j \cdot \frac{\left(1 - exp(-2D_j/L_j)\right)}{2} L_j \right] \tag{5.10}$$

where T refers to the trasmissivity of the air-sample interface. The terms in the sum can be grouped according to the value of the layers composition. The compositional range can be divided in intervals, for example with steps equal to 0.05:

$$I = \sum_j [I_j]_{x_j=0} + \sum_k [I_k]_{x_k=0.05} + \ldots + \sum_l [I_l]_{x_l=1} =$$
$$= I_{x=0} + I_{x=0.05} + \ldots + I_{x=1} \tag{5.11}$$

The expression above can be easily calculated once that the values of alloy composition and thickness are assigned to each layer: this equivals to specifying the composition profile in the stack. Moreover, the Raman spectrum of the stack can be simulated by summing the normalized Raman spectra $\phi_x(\omega)$ of $Si_{1-x}Ge_x$ introduced in section 5.1, each one weighted for the respective coefficient I_x. In the calculation of the coefficients I_x, the values of the Raman cross section S obtained with the approximated data elaboration (see section 4.4.2) must be used: actually, we remind that the approximated procedure relies on the same normalization condition on the Raman spectra of $Si_{1-x}Ge_x$ which is used in the decomposition of the experimental spectrum (see sections 4.3.5 and 5.1). The simulation of the spectrum can give useful hints, for example, in choosing the parameters of a Raman experiment, or in the discussion of the results.

However, our ultimate aim is to go the inverse path, and obtain the composition profile from the experimental Raman spectrum of the sample. The problem can be solved by finding a composition profile (x_j, D_j) for which the calculated coefficients I_x are equal to the coefficients a_k given by the spectral analysis described in section 5.1. Actually, expression 5.2 can be compared directly to equation 5.6, with $I_x \leftrightarrow a_x$. The offset term a_o can be discarded since it represents only a rigid vertical traslation of the spectrum, which does not change its shape. It is convenient to get independent from the experimental parameters I_0 and η (see expression 5.10), which are simply overall multiplicative constants, by considering the normalized quantities:

$$a'_k = \frac{a_k}{\sum_l a_l} \tag{5.12}$$

$$I'_x = \frac{I_x}{\sum_{x'} I_{x'}} \tag{5.13}$$

If a composition profile of the stack is able to give $I'_x = a'_x \, \forall x$, it means that the simulated spectrum of the stack reproduces closely the shape of the experimental spectrum.

However, the formulation of the problem is still too general: actually, the solution cannot be univocally determined just by the condition $I'_x = a'_x \, \forall x$, due to the fact that the same values of the I'_x can be obtained from many different composition profiles. Some hypotheses on the structure of the sample are required. For example, for $Si_{1-x}Ge_x$ islands grown by MBE deposition of pure Ge on Si, it will be reasonable to expect a monotonic variation of the composition from Ge-rich to Si-rich values starting from the top of the islands; for $Si_{1-x}Ge_x$ quantum wells, the layers will have a periodical structure, alternating wells and barriers with the same respective thickness. These hypotheses, which can be easily inferred on the basis of the growth process, fix the arrangement of the layers with different composition inside the sample. The values of the composition of the layers are given directly by the results of the spectral analysis; the only free parameters are the thickness values of the layers, which complete the description of the composition profile inside the sample.

From a practical point of view, since equations 5.2 and 5.10 cannot be simply inverted, an iterative approach is required. A starting composition profile (x_j, D_j) is guessed, and the coefficients I'_x are calculated. The euclidean distance between the vectors with coefficients I'_x and a'_x is computed; then the thickness values D_j are iteratively varied in order to minimize the distance between I'_x and a'_x. An additional constraint is required in the optimization: the sum of the thickness values must be equal to the thickness of the probed volume in the sample. If the excitation light completely crosses all the nanostructure, the total thickness is given simply by the total thickness of the structure, which can be obtained from a fast structural characterization, for instance by Atomic Force Microscopy (AFM). This is equivalent to require that for each layer the following condition is fulfilled:

$$D_j < L_j \tag{5.14}$$

which express the obvious fact that a layer must be completely probed if we want to measure it. In order to carry out the numerical optimization, an Interior Point Algorithm (implemented in MatLab) was used.

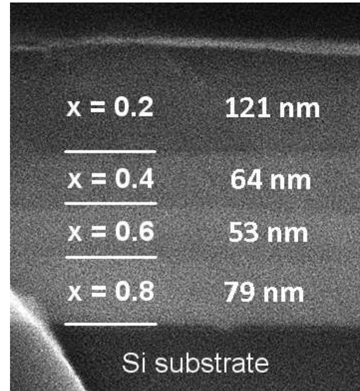

Figure 5.1: SEM image of the calibrated stack of SiGe layers used for the validation of the method for the extraction of the composition profile in SiGe nanostructures. The values of the composition and thickness of each layer are displayed.

5.3 Validation of the method

The methodology was tested with the aid of a calibration sample, i.e. a stack of four $Si_{1-x}Ge_x$ layers with well controlled alloy composition and thickness. The layers were grown by LEPECVD with nominal alloy composition x equal to $0.2, 0.4, 0.6$ and 0.8 (counted from the top of the sample). The thickness of each layer was directly measured by Scanning Electron Microscopy by looking at the sample in cross view: the values of thickness were equal to 121, 64, 53 and 79 nm respectively. Figure 5.1 shows the SEM image of the sample: the difference in the alloy composition is the source of the constrast, which is strong enough to allow individuating the interfaces between the layers.

The alloy composition and the strain in the layers were checked independently by XRD measurements. The measured values of the composition were 0.184, 0.406, 0.619 and 0.802, in agreement with the nominal values within 0.02; respectively, the values of the strain (in-plane) were equal to 0.34%, 0.10%, 0.13% and -0.12%. From the values of the strain, it can be stated that plastic relaxation has occurred almost completely in all the $Si_{1-x}Ge_x$ layers. The value of the strain in the first layer (x = 0.184) is confirmed by the Raman shift value of the respective Si-Si peak (505.8 cm^{-1}): for a composition equal to 0.184, a strain equal to 0.35% $\pm$ 0.20 % is obtained.

The Raman spectrum of the layers stack was taken with 532 nm excitation

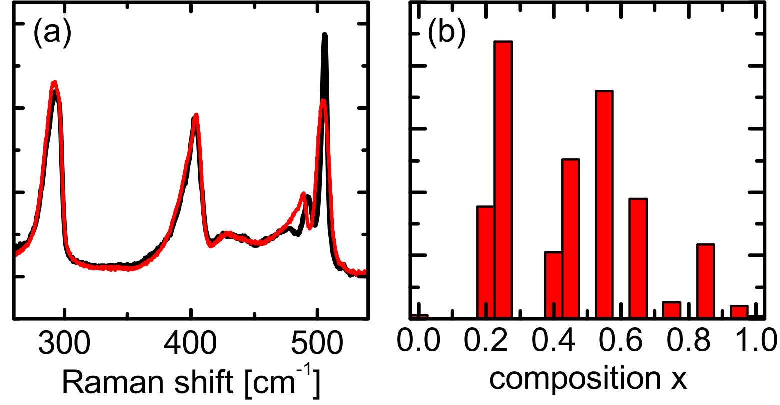

Figure 5.2: Panel (a): experimental (black) and reconstructed (red) spectrum of the layers stack. Panel (b): plot of the spectral contributions for each value of the alloy composition x. The compositional range is divided in intervals with $\Delta x = 0.05$.

light, in $[001]([100],-)[00\bar{1}]$ configuration. As usual, the power of the laser was kept low (0.1 mW in this case) in order to avoid the heating of the sample. Figure 5.2 reports in panel (a) the experimental spectrum (black) of the stack. Four distinct peaks are detected: the two resolved peaks located around 500 cm^{-1} are mostly given by the Si-Si Raman modes of the two layers with $x = 0.2$ and $x = 0.4$. They can be individuated distinctly because of the abrupt variation of the alloy composition in the stack, together with the strong dependence of the Si-Si mode frequency with respect to x (see equations 3.6). Apart from these two contributions, all the others overlap completely and cannot be distinguished. Panel (b) in figure 5.2 displays the spectral contributions obtained through the application of the numerical algorithm described in section 5.1: contributions in the ranges [0.2-0.25], [0.4-0.45], [0.55-0.65], [0.75-0.95] are detected. The reconstructed spectrum, i.e. the quantity $\sum a_x \phi_x(\omega)$ is plotted in red in panel (a) of figure 5.2: as can be seen, the experimental spectrum is well reproduced almost everywhere, except in the range close to 500 cm^{-1} in which the two resolved peaks are followed less closely. The origin of this discrepancy is due to the presence of the residual strain in the first layer, as will be explained later in section 5.5. At this point, we keep this in mind, and continue with the application of the algorithm.

In the sample, the first three layers respect the condition given in equation 5.14, while the fourth does not. As a consequence, the minimization described

in section 5.2 for the determination of the composition profile in the stack was applied to the first three layers: only the spectral contribution with $x \leq 0.65$ were considered in the numerical algorithm, and the constraint on the total thickness was consistently limited to the sum of the first three layers (238 nm), as given by the SEM measurements.

All the results are summarized in figure 5.3, which reports the spectra (experimental and reconstructed), the spectral contributions (in which the discarded contribution above $x = 0.7$ have been plotted in grey) and the composition profile obtained through the application of the numerical tool (red line in panel (c)), compared to the data extracted from the SEM image (shown in the inset). The good correspondence between the two profiles shows the power of this kind of analysis: the information about the composition profile, buried in the experimental Raman spectrum, has been explicited. This same information was not accessible by the direct inspection of the spectrum, for instance by looking directly at the position of the peaks.

5.4 Application to SiGe islands

5.4.1 Measurements at 532 nm

The analysis method, validated through the application to the calibrated sample, was applied to the Raman spectrum of the unetched islands described in section 4.5.1, taken with 532 nm excitation wavelength. Assuming a composition value of the alloy in the islands close to 0.4 (as estimated from the peak positions), it is immediate to see that the structures are completely crossed by the excitation light ($D_{islands} \approx 34$ nm; $L_{532}(0.4) \approx 300$ nm, see figure 4.7). The results of the analysis are displayed in figure 5.4: we refer to this figure in the following. The spectrum of the bulk Si substrate was subtracted from the spectrum of the sample in order to evidence the signal coming from the islands (panel (a)). The deconvolution procedure was then applied to the subtracted spectrum and the spectral contributions were extracted: they are plotted in panel (b). The reconstructed spectrum is plotted as a green line in panel (a): it reproduces closely the experimental data, so the deconvolution is expected to give a good representation of the composition inhomogeneity inside the islands. Spectral contributions in the compositional range

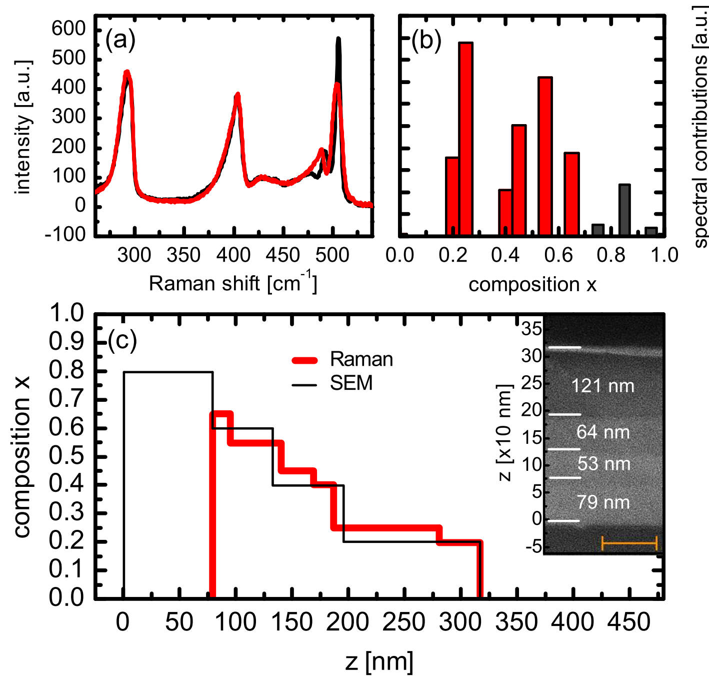

Figure 5.3: Summary of the results of the application of the spectrum analysis algorithm. Panel (a)-(b): as in figure 5.2. The spectral contribution of the fourth layer are discarded from the calculation of the composition profile (see text) and are plotted in grey. Panel (c): composition profiles of the layers stack, as given by SEM (black line) and by the Raman analysis (red line). The SEM image is reported in the inset, with a scale bar equal to 100 nm)

[0.25-0.5] are detected, with two major contributions at $x = 0.45$ and $x = 0.35$.

For the composition profiling routine, an approximated representation of the islands was given, again by modelling the islands as stacks of layers with different composition. The validity of this approximation will be demonstrated by the results. On the basis of the growth process (MBE deposition of pure Ge on Si, followed by intermixing with the atoms of the substrate), the variation of the composition inside the islands was supposed to be monotonical, with the Ge-richer layers at the top of the structure. AFM measurements (reported in the inset in panel (c)) provided the constraint on the total thickness of the islands ($D_{islands} \approx 34$ nm). The resulting composition profile inside the islands is plotted with the green solid line in panel (c). Two other composition profiles, obtained with two independent techniques (AFM tomography and X-Ray diffraction), are plotted as well: the

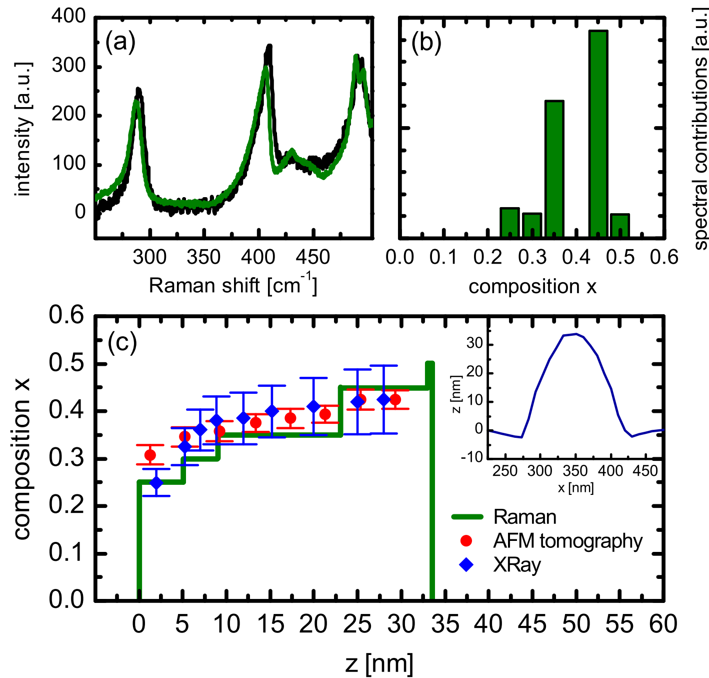

Figure 5.4: Summary of the results given by the analysis of the Raman spectra of SiGe islands measured with 532 nm excitation light. Panel (a): experimental (black) and reconstructed spectra (green). Panel (b); spectral contributions. Panel (c): composition profile inside the islands, as given by the Raman analysis (green solid line), AFM tomography (red points) and XRay diffraction (blue points), from [153]. In the inset of panel (c), AFM profile of one island.

data, related to islands grown with similar parameters and characterized by the same shape and size (barns), were taken from the work of Rastelli et al. (see figure 3(d) in [153]). The agreement between the profiles is fairly good throughout the entire island, despite the approximation on their internal structure.

5.4.2 Measurements at 458 nm

The analysis routine was applied also to the subtracted spectrum of the unetched islands observed under 458 nm excitation light. The penetration depth of the light at 458 nm in a $Si_{1-x}Ge_x$ alloy with composition $x \approx 0.4$ is about 40 nm, which is very close to the total height of the islands: we still consider condition 5.14 to be fulfilled and apply the same procedure as before, with the same constraint

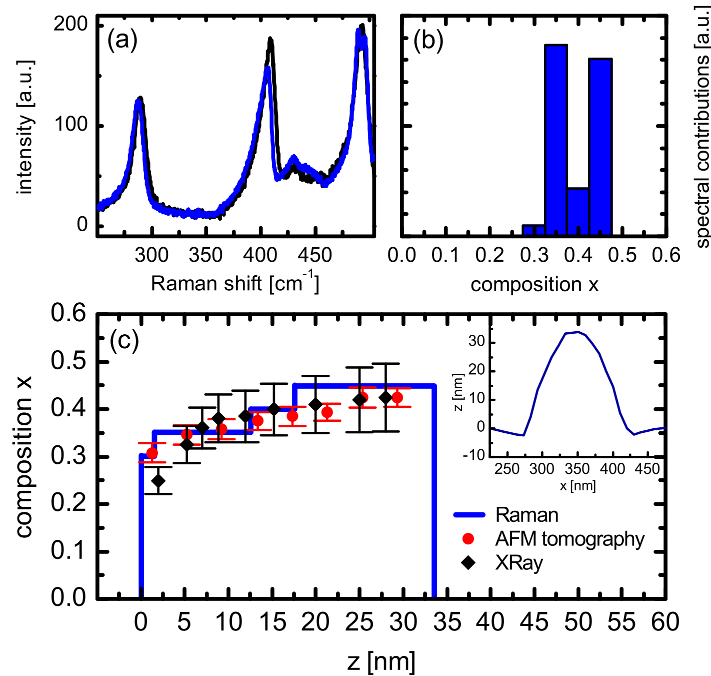

Figure 5.5: Summary of the results given by the analysis of the Raman spectra of SiGe islands measured with 458 nm excitation light. Panel (a): experimental (black) and reconstructed spectra (blue). Panel (b); spectral contributions. Panel (c): composition profile inside the islands, as given by the Raman analysis (blue solid line), AFM tomography (red data) and XRay diffraction (black data), from [153]. In the inset of panel (c), AFM profile of one island.

on the total thickness of the island as given by the AFM profiles. The results are summarized in figure 5.5, with the same scheme given before. In panel (c) of figure 5.5 the composition profile is again compared to the results of the AFM tomography and X-Ray diffraction already reported in figure 5.4. Also in this case a satisfactory agreement is found.

Finally, in figure 5.6 the obtained Raman profiles are compared to the values of composition extracted from the conventional Raman measurements taken on the progressively etched islands (section 4.5.1) with 532 nm (panel (a)) and 458 nm excitation light (panel (b)). It can be seen that the conventional Raman measurements give, for each etching step, an *upper* value of the composition present in the islands. The power of the analysis routine, with respect to the single measurements, lies actually in the capability of analyzing not only the position of the

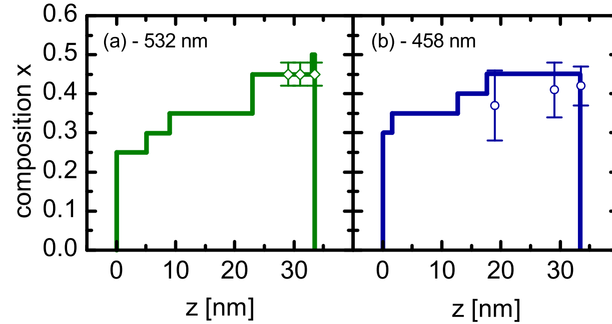

Figure 5.6: Comparison between the composition profiles (solid lines) obtained by Raman and the single Raman measurements taken on the etched islands. Panel (a): 532 nm excitation wavelength; panel (b): 458 nm excitation wavelength.

peaks, but also their linewidth.

These composition profiles are those used for the simulation of the total spectrum of the islands, which were plotted and compared to the experimental data in figure 4.16. The lateral size and the density of the nanostructures on the surface of the substrate were extracted from AFM images of the sample; these two parameters are necessary to calculate the relative intensity of the signal coming from the islands with respect to the Si bulk substrate. Coming back to figure 4.16, it can be seen that the experimental behaviour of the islands signal intensity with respect to the excitation light energy is accurately reproduced by the simulations. The simulated decay rate of the island Raman signal with the etching, on the contrary, is not well described: it results slower than the experimental one. This means that the composition inhomogeneity inside the islands (which leads to a change in the resonance conditions) is not able to explain the origin of the different decay of the island Raman intensity with respect to the island volume.

5.5 Limitations to the method

We now discuss briefly the limits of the numerical method outlined in the previous sections. A first condition on the applicability of the procedure was given by the relation between the total thickness of the probed nanostructure and the penetration depth of the light (see equation 5.14 in section 5.2). However, the major limitations are intrinsic to the method and lie in the fact that, in the spectral

analysis routine (5.1) the variation in the Raman peak positions can be interpreted only in terms of changes in the alloy composition. Actually, the $Si_{1-x}Ge_x$ Raman spectra taken as reference in the spectral analysis are related to different values of the alloy composition, in a relaxed material. Any factor, apart from the alloy composition, which is also able to move or broaden the Raman peaks will be translated by the spectral analysis into a compositional inhomogeneity.

The principal sources of errors in the interpretation of the Raman spectra can be individuated in strain or phonon confinement. The strain can shift the frequencies of the $Si_{1-x}Ge_x$ Raman peaks, as it was explained in sections 3.5 and 4.1.1. Phonon confinement, on the other hand, leads mostly to the broadening of the peaks. This effect occurs in nanostructures with size comparable to the wavelength of the phonons in the material (typically below 5 nm): due to the change in the boundary conditions, the selection rules are relaxed along the direction of the confinement. This allows the scattering of the photons by vibrations which are usually excluded from the photon-phonon interaction in the infinite crystalline solid due to the momentum conservation (equation 4.6): as a consequence, the Raman peaks become broadened toward lower Raman shift (because the optical phonon branches are bent downward). A description of the change in the Raman peak lineshape induced by phonon confinement can be found in [154]. As a consequence, we expect that our spectral analysis routine will not be reliable in presence of very small nanostructures in which phonon confinement occurs: we can also say that for nanostructures with size larger than 10-15 nm the effects of phonon confinement should not affect the results.

Strain represents the main issue: it is often present in $Si_{1-x}Ge_x$ nanostructures due to the dependence of the alloy lattice parameter on the alloy composition; in general, it can be expected to be present for all the $Si_{1-x}Ge_x$ structures whose size is below the critical thickness for plastic relaxation. Then, it is worthwhile to better understand how and how much the presence of strain can affect the results of the spectral analysis. In order to investigate this point, we measured the Raman spectra of three $Si_{0.6}Ge_{0.4}$ epilayers, grown pseudomorphically by LEPECVD on three graded $Si_{1-x}Ge_x$ buffers. The alloy composition in the graded buffers started from $x = 0$ and varied linearly with respect to the thickness up to $x = 0.2$, 0.4 and 0.6, in order to obtain a different state of strain in the epilayers grown on top. The thickness of the epilayers was obviously kept below the critical value for

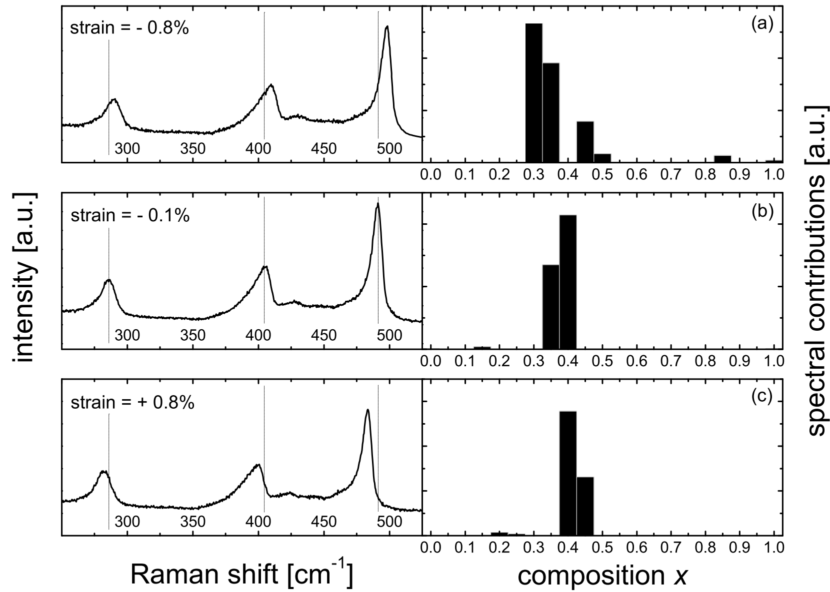

Figure 5.7: Effect of the strain on the spectral analysis of $Si_{0.6}Ge_{0.4}$ alloy. Left (from the top): spectra of the compressively strained, relaxed and tensily strained alloy. The value of the strain is reported in the panels. The dotted lines, marking the position of the Raman peaks in the relaxed alloy, put into evidence the shifts given by the strain. Panels (a)-(c): composition contributions detected by the spectral analysis routine outlined in section 5.1. Spurious spectral contributions appear, mostly for the compressively strained alloy.

plastic relaxation. The strain, measured by X-Ray diffraction (Reciprocal Space Mapping) was equal to -0.8%, -0.1% and 0.8% in the three epilayers respectively. After the measurement of the Raman spectra, we applied the spectral analysis routine, and obtained the results displayed in figure 5.7.

Figure 5.7 demonstrates the effect of the presence of strain on the output of the spectral analysis routine. In the first case, shown in panel (a), compressive strain shifts all the Raman peaks towards higher Raman shift values. The routine reads the shift of the Si-Si peak as the presence of layers with lower composition ($x \approx 0.3$), and the shift of the Ge-Ge peaks in terms of contributions at higher composition (note the small contribution at $x = 0.8$). In the second case, panel (b), in which the strain is very small (-0.1%), the composition is read correctly within 0.05: two contributions are seen in the range [0.35-0.4]. In the last case, panel (c), the Raman peaks move toward lower Raman shift due to tensile strain. In this case, the composition contributions are slightly shifted towards Ge-richer

values [0.4-0.45].

Going back to the analysis of the calibrated layers stack (section 5.3), it can be noted that the small tensile strain in the first layer (0.3%) was able to introduce a -2.5 cm^{-1} shift of the Si-Si Raman peak: this was read by the analysis routine as a spectral contribution located at composition $x = 0.25$. For this reason the reconstructed spectrum did not closely fit the experimental one.

Chapter 6

Conclusions

In the last two decades, attention has raised towards $Si_{1-x}Ge_x$ heterostructures and nanostructures, and efforts have been payed in order to understand and characterize their structural, vibrational, electronic and optical properties. The main advantage of $Si_{1-x}Ge_x$ lies in the possibility of tuning its physical properties between those of pure Si and pure Ge by controlling the alloy composition. The continuous variation with the composition of several physical quantities (lattice parameter, electronic transitions, thermal conductivity, phonon frequencies, absorption coefficient etc.) has been determined in the past years. In particular, the dependence of the lattice parameter on the composition plays a crucial role in $Si_{1-x}Ge_x$ heteroepitaxy: actually, the lattice mismatch causes the rise of strain fields which represent an important driving force in the growth, and determines together with the alloy composition the electronic, vibrational and optical properties of the system.

However, a number of other physical quantities are still to be characterized as functions of the alloy composition: the Raman cross section of $Si_{1-x}Ge_x$ is one of these. Strong modulation of the Raman cross section with the alloy composition can be expected due to the composition dependent variation of the $Si_{1-x}Ge_x$ direct electronic transitions: when the excitation light used for the Raman experiment matches the energy of the direct transitions, a resonance in the Raman cross section is predicted.

In this work, an experiment has been set up with the aim of measuring the $Si_{1-x}Ge_x$ Raman cross section across the whole compositional range. A novel

and efficient approach has been used in order to collect a large number of data for many different values of the composition. The Raman cross section has been obtained with a resolution in the alloy composition $\Delta x \approx 0.03$, by measuring with a MicroRaman equipment the Raman spectra of a graded $Si_{1-x}Ge_x$ buffer along the growth direction. The measurements have been performed at six different excitation wavelengths, in the visible and UV range. The resonance data taken at different excitation wavelengths were normalized to a Raman efficiency reference (CaF_2) in order to compare directly the results. A resonant behaviour of the Raman cross section was indeed observed: resonance peaks were measured, occurring at different values of the alloy composition in dependence of the used excitation wavelength. The strongest effects are due to the resonance of the excitation light wavelength with the $E_1/E_1+\Delta_1$ direct electronic transitions; also minor resonances due to the $E_0/E_0+\Delta_0$ transitions were detected. The height of the resonance Raman peaks depends also on the excitation wavelength. A theoretical framework linking the Raman cross section to the derivative of the dielectric function with respect to the frequency was used in order to discuss the behaviour of the Raman cross section. Good agreement was found between our data and the results of a semiempirical calculation based on the experimental values of the dielectric function obtained by ellipsometry. The resonant behaviour of the Raman cross section was also analyzed by considering each $Si_{1-x}Ge_x$ Raman mode separately.

This work fills the existing gap in the literature between the Raman efficiency of pure Si and pure Ge, and gives a unified picture of the behaviour of their Raman cross section. However, beyond the characterization of a fundamental property of the alloy, the knowledge of the Raman efficiency is useful in understanding the features of Raman effect in inhomogeneous $Si_{1-x}Ge_x$ samples. In $Si_{1-x}Ge_x$ systems where a compositional distribution is present, the Raman cross section changes from point to point, enhancing the signal coming from different parts of the sample depending on the used excitation wavelength. This is particularly true in $Si_{1-x}Ge_x$ nanostructures, where one of the mechanisms for the relaxation of the strain is given by inhomogeneous alloying. Changes in the intensity and shape of the Raman spectra of $Si_{1-x}Ge_x$ nanostructures have been reported in the literature, but the knowledge of the $Si_{1-x}Ge_x$ Raman cross section enables the experimenter to have better insight into this phenomenon. In this work, several

Raman experiments of $Si_{1-x}Ge_x$ islands have been reported and discussed on the basis of the Raman resonance.

Finally, in this work a numerical tool has been presented, which is aimed at extracting quantitative information about the composition inhomogeneity in the sample from the broadening of the $Si_{1-x}Ge_x$ Raman modes. The Raman spectrum of the system is written as a weighted sum of $Si_{1-x}Ge_x$ Raman spectra at different alloy composition: a self consistent routine finds the combination of spectra which is able to best match the experimental spectrum. When the structure of the sample is qualitatively known, also a compositional profile can be extracted by means of a second self consistent routine which takes into account the Raman cross section of the alloy. The method was validated on a sample with known compositional profile, and applied to $Si_{1-x}Ge_x$ islands: the results are compatible with the data obtained by independent techniques. The accuracy of the analysis is limited by the presence of other factors which can influence the lineshape, namely phonon confinement and strain. However, for strain values below 1%, we estimate the deviations in our compositional profiles to be within 0.1 in the values of the alloy composition.

In conclusion, we demonstrated that it is possible to obtain information about the compositional inhomogeneity inside $Si_{1-x}Ge_x$ nanostructures through Raman spectroscopy, extending its capabilities beyond the estimation of the average value of the alloy composition in the structures. The knowledge of the Raman cross section allows interpreting the results of a Raman measurements on inhomogeneous $Si_{1-x}Ge_x$ in deeper detail, and helps finding the optimal excitation conditions for their characterization.

Acknowledgements

I would like to thank D. Chrastina and G. Isella (*LNESS - Laboratory for Epitaxial Nanostructures on Silicon and Spintronics - Como, Italy*) for the fabrication of the sample used for the measurement of the $Si_{1-x}Ge_x$ Raman efficiency. I acknowledge again G. Isella and F. Isa (*LNESS*) for the growth of the calibrated $Si_{1-x}Ge_x$ sample studied in section 5.3. S. Cecchi (*LNESS*) provided the X-Ray characterization of the sample, and C.V. Falub (*ETH Zurich, Switzerland*) performed the SEM inspection in cross view. F. Pezzoli (*Universit degli Studi di Milano - Bicocca, Italy*) is acknowledged for the growth of the island samples studied in this work. I would like also to thank M. Giarola and G. Mariotto (*Universit degli Studi di Verona, Italy*) for the collaboration to the measurement of the $Si_{1-x}Ge_x$ Raman efficiency. I would like also to acknowledge all the students which helped me in the development of this work.

Good Physicists Have Studied
Under Very Fine Teachers

Mnemonic rule
Thermodynamics

I would like to express all my gratitude to all the people I worked and lived with during these three years of PhD, first of all the colleagues in my research group (LaSSem - Laboratory of Semiconductor Spectroscopy) at the University of Milano - Bicocca.

A special thank is for dr. Emiliano Bonera, for his careful and stimulating supervision of my work: these three years represented an opportunity not only of interesting and enjoyable work, but also of friendship and personal growth.

Another special thank is for prof. Mario Guzzi, whose presence was important for me from the beginning of my academic experience: I consider him as an example from many points of view.

I thank prof. Emanuele Grilli, especially for all the enjoyable discussions in the lab and at his desk: his technical knowledge and inexhaustible resources are always matter of admiration for me and all the other students.

I am grateful to my PhD-mate and colleague Eleonora Gatti: her presence is always able to bring brightness, cheerfulness (and order!) to all the group. I want to acknowledge F. Pezzoli, the first PhD student I worked with, and all the students I met and/or supervisioned as a PhD student myself during these years. Thanks also to prof. Sanguinetti for his precious advices, and to the directors of the PhD school, prof. Leo Miglio and prof. Gianfranco Pacchioni.

This group is renowned for its capability of providing an environment in which students and workers can grow in their professional skills and experience a unique atmosphere of friendship and collaboration. I have always done my best in order to give a contribution compliant with the scope and the spirit which animate this group: I would be glad to continue to collaborate also in the future, with the hope of opening even more opportunities to the people which take part to this great experience.

Another research group of which I will always feel to be part is the INT-PAC/REMO group in IMEC Leuven (Belgium), in which I spent six unforgettable months with unforgettable people.

I am totally grateful to prof. Ingrid De Wolf, for giving me the opportunity of working and living there: that experience left a deep trace in me. A special thanks to all the colleagues and friends in Leuven: I keep a very nice memory of them all, and hope to see them soon again.

Finally, I want to thank my parents, my brother Alberto, all my family and the people and friends which have always been close to me.

As it is not really possible to express my gratitude with words, I hope I will have many opportunities to put my skills at service of many others: this is the best way to be grateful, as I was taught by so many good teachers.

Bibliography

[1] D.J. Paul. *Semicond. Sci. Technol.*, 19:R75, 2004.

[2] R.T. Carline, D.J. Robbins, M.B. Stanaway, and W.Y. Leong. *Appl. Phys. Lett.*, 68:544, 1996.

[3] G. Dehlinger, L. Diehl, U. Gennser, H. Sigg, J. Faist, K. Ensslin, D. Grützmacher, and E. Müller. *Science*, 290:2277, 2000.

[4] J.P. Dismukes, L. Ekstrom, and R.J. Paff. *J. Phys. Chem.*, 68:3021, 1964.

[5] E. Kasper, A. Schuh, G. Bauer, B. Holländer, and H.K. Kibbel. *J. Crystal Growth*, 157:68, 1995.

[6] E. Kasper and K. Lyutovich, editors. *Properties of Silicon Germanium and SiGe:Carbon*. EMIS Datareviews, 1999.

[7] J.F. Nye. *Physical properties of crystals*, volume 7. Oxford University Press, 1957.

[8] L.D. Landau and E.M. Lifshitz. *Theory of elasticity*, volume 7. Oxford University Press, 3 edition, 1986.

[9] Schäffler F. *Properties of Advanced SemiconductorMaterials GaN, AlN, InN, BN, SiC, SiGe*. John Wiley and Sons Inc. New York, 2001.

[10] R. Braunstein. *Phys. Rev.*, 130:869, 1963.

[11] F. Schäffler. *Semicond. Sci. Technol.*, 12:1515, 1997.

[12] J. Weber and M.I. Alonso. *Phys. Rev. B*, 40:5683, 1989.

[13] J.B. Chelikowsky and M.L. Cohen. *Phys. Rev. Lett.*, 31:1582, 1973.

[14] P. Lautenschlager, P.B. Allen, and M. Cardona. *Phys. Rev. B*, 31:2163, 1985.

[15] J. Humlicek, M. Garriga, M.I. Alonso, and M. Cardona. *J. Appl. Phys.*, 65:2827, 1989.

[16] K. Brunner. *Rep. Prog. Phys.*, 65:27, 2002.

[17] T. Ebner, K. Thonke, R. Sauer, F. Shäffler, and H.J. Herzog. *Phys. Rev. B*, 57:15448, 1998.

[18] U. Schmid, N.E. Christensen, and M. Cardona. *Solid State Comm.*, 75:39, 1990.

[19] V.A. Shchukin and D. Bimberg. *Rev. Mod. Phys.*, 71:1125, 1999.

[20] J.W. Matthews and A.E. Blakeslee. *J. Crystal. Growth*, 27:118, 1974.

[21] J.H. Van der Merve. *Surf. Sci.*, 31:198, 1972.

[22] J.W. Matthews and A.E. Blakeslee. *J. Crystal. Growth*, 29:273, 1975.

[23] J.W. Matthews and A.E. Blakeslee. *J. Crystal. Growth*, 32:265, 1976.

[24] J.C. Bean, L.C. Feldman, A.T. Fiory, S. Nakahara, and I.K. Robinson. *J. Vac. Sci. Technol. A*, 2:436, 1984.

[25] D.C. Houghton, C.J. Gibbings, C.G. Tuppen, M.H. Lyons, and M.A.G. Halliwell. *Appl. Phys. Lett.*, 56:460, 1990.

[26] D.C. Houghton, D.D. Perovic, J.-M. Baribeau, and G.C. Weatherly. *J. Appl. Phys.*, 67:1850, 1990.

[27] J. Stangl, V. Holý, and G. Bauer. *Reviews of modern physics*, 76:725, 2004.

[28] C. Teichert, C. Hofer, K. Lyutovich, M. Bauer, and E. Kasper. *Phys. Rep.*, 365:335, 2002.

[29] A. Vailionis, B. Cho, G. Glass, P. Desjardins, D.G. Cahill, and J.E. Green. *Phys. Rev. Lett.*, 85:3672, 2000.

[30] K.M. Chen, D.E. Jesson, S.J. Pennycook, T. Thundat, and R.J. Warmack. *Phys. Rev. B*, 56:R1700, 1997.

[31] Y.-W. Mo, D.E. Savage, B.S. Swartzentruber, and M.G. Lagally. *Phys. Rev. Lett.*

[32] J.A. Floro, G.A. Lucadamo, E. Chason, L.B. Freund, M. Sinclair, R.D. Twesten, and R.Q. Hwang. *Phys. Rev. Lett.*, 80:4717, 1998.

[33] F.M. Ross, R.M. Tromp, and M.C. Reuter. *Science*, 286:1931, 1999.

[34] G. Medeiros-Ribeiro, A.M. Bratkovski, T.I. Kamins, D.A.A. Ohlberg, and R.S. Williams. *Science*, 279:353, 1998.

[35] E. Sutter, P. Sutter, and J.E. Bernard. *Appl. Phys. Lett.*, 84:2262, 2004.

[36] F.K. LeGoues, M.C. Reuter, J. Tersoff, M. Hammar, and R.M. Tromp. *Phys. Rev. Lett.*, 73:300, 1994.

[37] T. Merdzhanova, S. Kiravittaya, A. Rastelli, M. Stoffel, U. Denker, and O.G. Schmidt. *Phys. Rev. Lett.*, 96:226103, 2006.

[38] M.-I. Richard, T.U. Schülli, G. Renaud, E. Wintersberger, G. Chen, G. Bauer, and V. Holý. *Phys. Rev. B*, 80:045313, 2009.

[39] J.A. Floro, E. Chason, M.B. Sinclair, L.B. Freund, and G.A. Lucadamo. *Appl. Phys. Lett.*, 73:951, 1998.

[40] L. Miglio and F. Montalenti. *Silicon-Germanium (SiGe) Nanostructures*. Woodhead Publishing, 2011.

[41] C. Ratsch and A. Zangwill. *Surf. Sci.*, 293:123, 1993.

[42] S. Cereda and F. Montalenti. *Phys. Rev. B*, 81:125439, 2010.

[43] P. Raiteri, L. Miglio, F. Valentinotti, and M. Celino. *Appl. Phys. Lett.*, 80:3736, 2002.

[44] D.T. Tambe and V.B. Shenoy. *Phys. Rev. B*, 85:1586, 2004.

[45] Y. Tu and J. Tersoff. *Phys. Rev. Lett.*, 98:096103, 2007.

[46] J. Tersoff and F.K. LeGoues. *Phys. Rev. Lett.*, 72:3570, 1994.

[47] G.-H. Lu, M. Cuma, and F. Liu. *Phys. Rev. B*, 72:125415, 2005.

[48] O.E. Shklyaev, M.J. Beck, M. Asta, M.J. Miksis, and P.W. Voorhees. *Phys. Rev. Lett.*, 94:176102, 2005.

[49] M.J. Beck, A. van de Walle, and M. Asta. *Phys. Rev. B*, 70:205337, 2004.

[50] G.-H. Lu and F. Liu. *Phys. Rev. Lett.*, 94:176103, 2005.

[51] D.B. Migas, S. Cereda, F. Montalenti, and L. Miglio. *Surf. Sci.*, 556:121, 2004.

[52] M. Brehm, F. Montalenti, M. Grydlik, G. Vastola, H. Lichtenberger, N. Hrauda, M. J. Beck, T. Fromherz, F. Schäffler, L. Miglio, and G. Bauer. *Phys. Rev. B*, 80:205321, 2009.

[53] A. Rastelli, M. Stoffel, T. Merdzhanova, and O.G. Schmidt. *J. Phys.: Cond. Matter*, 20:454214, 2008.

[54] D. Digiuni, R. Gatti, and F. Montalenti. *Phys. Rev. B*, 80:155436, 2009.

[55] G. Katsaros, G. Costantini, M. Stoffel, R. Esteban, A.M. Bittner, A. Rastelli, U. Denker, O.G. Schmidt, and K. Kern. *Phys. Rev. B*, 72:195320, 2005.

[56] T.U. Schülli, G. Vastola, M.-I. Richard, A. Malachias, G. Renaud, F. Uhlik, F. Montalenti, G. Chen, L. Miglio, F. Schäffler, and G. Bauer. *Phys. Rev. Lett.*, 102:025502, 2009.

[57] M. Grydlik, M. Brehm, F. Hackl, H. Groiss, T. Fromherz, F. Schäffler, and G. Bauer. *New Journal of Physics*, 12:063002, 2010.

[58] Z. Zhong, W. Schwinger, F. Schäffler, G. Bauer G. Vastola, F. Montalenti, and L. Miglio. *Phys. Rev. Lett.*, 98:176102, 2007.

[59] F. Boioli, R. Gatti, M. Grydlik, M. Brehm, F. Montalenti, and L. Miglio. *Appl. Phys. Rev.*, 99:033106, 2011.

[60] C. Dais, G. Mussler, H. Sigg, T. Fromherz, V. Auzelyte, H.H. Solak, and D. Grützmacher. *EPL*, 84:67017, 2008.

[61] J. J. Zhang, M. Stoffel, A. Rastelli, O.G. Schmidt, V. Jovanovic, L.K. Nanver, and G. Bauer. *Appl. Phys. Lett.*, 91:173115, 2007.

[62] J.J. Zhang, A. Rastelli, H. Groiss, J. Tersoff, F. Schäffler, O.G. Schmidt, and G. Bauer. *Appl. Phys. Lett.*, 95:183102, 2009.

[63] O. Kienzle, F. Ernst, M. Ruhle, O.G. Schmidt, and K. Eberl. *Appl. Phys. Rev.*, 74:269, 1999.

[64] Y. Shiraki and N. Usami, editors. *Silicon-Germanium (SiGe) Nanostructures*. Woodhead Publishing, 2011.

[65] V. Jovanovic, C. Biasotto, L.K. Nanver, J. Moers, D. Grützmacher, J. Gerharz, G. Mussler, J. van der Cingel, J.J. Zhang, G. Bauer, O.G. Schmidt, and L. Miglio. *IEEE Elec. Dev. Lett.*, 31:1083, 2010.

[66] M.V. Fischetti and S.E. Laux. *J. Appl. Phys.*, 80:2234, 1996.

[67] J.L. Hoyt, H.M. Nayfeh, S. Eguchi, I. Aberg, G. Xia, T. Drake, E.A. Fitzgerald, and D.A. Antoniadis. Strained silicon mosfet technology. In *IEEE IEDM*, 2002.

[68] K. Rim. Strained si surface channel mosfets for high-performance cmos technology. In *IEEE International Solid-State Circuits Conference*, 2001.

[69] H. Okamoto, A. Hokazono, K. Adachi, N. Yasutake, H. Itokawa, S. Okamoto, M. Kondo, H. Tsujii, T. Ishida, N. Aoki, M. Fujiwara, S. Kawanaka, A. Azuma, and Y. Toyoshima. *Jap. J. Appl. Phys.*, 47:2564, 2008.

[70] R.A. Donaton, D. Chidambarrao, J. Johnson, P. Chang, Y. Liu, W.K. Henson, J. Holt, X. Li, J. Li, A. Domenicucci, A. Madan, K. Rim, and C. Wann. Design and fabrication of mosfets with a reverse embedded sige (rev. e-sige) structure. In *IEEE IEDM*, 2006.

[71] J.G. Fiorenza, J.-S. Park, and A. Lochtefeld. *IEEE Trans. Elec. Dev.*, 55:640, 2008.

[72] G.S. Kar, S. Kiravittaya, U. Denker, B.-Y. Nguyen, and O.G. Schmidt. *Appl. Phys. Lett.*, 88:253108, 2006.

[73] O.G. Schmidt and K. Eberl. *IEEE Trans. Elec. Dev.*, 48:1175, 2001.

[74] G. Vastola, A. Marzegalli, F. Montalenti, and L. Miglio. *Mat. Sci. Eng. B*, 159-160:90, 2009.

[75] N. Hrauda, J.J. Zhang, E. Wintersberger, T. Etzelstorfer, B. Mandl, J. Stangl, D. Carbone, V. Holý, V. Jovanovic, C. Biasotto, L.K. Nanver, J. Moers, D. Grützmacher, and G. Bauer. *Nano Letters*, 11:2875, 2011.

[76] E. Bonera, F. Pezzoli, A. Picco, G. Vastola, M. Stoffel, E. Grilli, M. Guzzi, A. Rastelli, O.G. Schmidt, and L. Miglio. *Phys. Rev. B*, 79:075321, 2009.

[77] L.K. Nanver, V. Jovanovic, C. Biasotto, J. Moers, D. Grützmacher, J.J. Zhang, N. Hrauda, M. Stoffel, F. Pezzoli, O.G. Schmidt, L. Miglio, H. Kosina, A. Marzegalli, G. Vastola, J. Stangl, G. Bauer, J. van der Cingel, and E. Bonera. *Solid State Electronics*, 60:75, 2011.

[78] J. Xia, Y. Takeda, N. Usami, T. Maruizumi, and Y. Shiraki. *Optics Express*, 13:13945, 2010.

[79] G. Pernot, M. Stoffel, I. Savic, F. Pezzoli, P. Chen, G. Savelli, A. Jacquot, J. Schumann, U. Denker, I. Mönch, Ch. Deneke, O.G. Schmidt, J.M. Rampnoux, S. Wang, M. Plissonier, A. Rastelli, S. Dilhaire, and N. Mingo. *Nature Materials*, 9:495, 2010.

[80] M.S. Dresselhaus, G. Chen, M.Y. Tang, R. Yang, H. Lee, D. Wang, Z. Ren, J.-P. Fleurial, and P. Gogna. *Adv. Mater.*, 19:1043, 2007.

[81] J.-M. Baribeau, X. Wu, N.L. Rowell, and D.J. Lockwood. *J. Phys.: Condens. Matter*, 18:R139, 2006.

[82] A. Rastelli, E. Mueller, and H. von Kaenel. *Appl. Phys. Lett.*, 80:1438, 2002.

[83] J.J. Zhang, N. Hrauda, H. Groiss, A. Rastelli, J. Stangl, F. Schäffler, O.G. Schmidt, and G. Bauer. *Appl. Phys. Lett.*, 96:193101, 2010.

[84] B. Voigtlander. *Surf. Sci. Rep.*, 43:127, 2001.

[85] M. Stoffel, A. Malachias, T. Merdzhanova, F. Cavallo, G. Isella, D. Chrastina, H. von Kaenel, A. Rastelli, and O.G. Schmidt. *Semicond. Sci. Technol.*, 23:085021, 2008.

[86] F. Pezzoli, M. Stoffel, T. Merdzhanova, A. Rastelli, and O.G. Schmidt. *Nanoscale Res. Lett.*, 4:1073, 2009.

[87] J.J. Zhang, F. Montalenti, A. Rastelli, N. Hrauda, D. Scopece, H. Groiss, J. Stangl, F. Pezzoli, F. Shäeffler, O.G. Schmidt, L. Miglio, and G. Bauer. *Phys. Rev. Lett.*, 105:166102, 2010.

[88] J.J. Zhang, A. Rastelli, O.G. Schmidt, and G. Bauer. *Semicond. Sci. Technol.*, 26:014028, 2011.

[89] T.U. Schülli. *Semicond. Sci. Technol.*, 26:064003, 2011.

[90] F. Wooten. *Optical Properties of Solids*. Academic Press, 1972.

[91] M.E. Kurdi, S. Sauvage, G. Fishman, and P. Boucaud. *Phys. Rev. B*, 73:195327, 2006.

[92] J. Drucker. *IEEE J. Quant. Elec.*, 38:975, 2002.

[93] L. Tsybeskov, E.-K. Lee, H.-Y. Chang, D.J. Lockwood, J.-M. Baribeau, X. Wu, and T.I. Kamins. *Appl. Phys. A*, 95:1015, 2009.

[94] M. Brehm, M. Grydlik, F. Hackl, E. Lausecker, T. Fromherz, and G. Bauer. *Nanoscale Res. Lett.*, 5:1868, 2010.

[95] D. J. Lockwood, J.-M. Baribeau, B.V. Kamenev, E.-K. Lee, and L. Tsybeskov. *Semicond. Sci. Technol.*, 23:064003, 2008.

[96] M. Brehm, T. Suzuki, Z. Zhong, T. Fromherz, J. Stangl, G. Hesser, S. Birner, F. Schäffler, and G. Bauer. *Microelectronics Journal*, 39:485, 2008.

[97] M. Brehm, T. Suzuki, T. Fromherz, Z. Zhong, N. Hrauda, F. Hackl, J. Stangl, F. Schäffler, and G. Bauer. *New Journal of Physics*, 11:063021, 2009.

[98] R.O. Rezaev, , S. Kiravittaya, V.M. Fomin, A. Rastelli, and O.G. Schmidt. *Phys. Rev. B*, 82:153306, 2010.

[99] M. Brehm, M. Grydlik, H. Groiss, F. Hackl, F. Schäffler, T. Fromherz, and G. Bauer. *J. Appl. Phys.*, 109:123505, 2011.

[100] M.V. Shaleev, A.V. Novikov, A.N. Yablonskiy, Y.N. Drozdov, O.A. Kuznetsov, D.N. Lobanov, and Z.F. Krasilnik. *Thin Solid Films*, 517:385, 2008.

[101] M. Shaleev, A. Novikov, N. Baydakova, A. Yablonskiy, O. Kuznetsov, Y. Drozdov, D. Lobanov, and Z. Krasilnik. *Phys. Status Solidi C*, 8:1055, 2011.

[102] E. Lausecker, M. Brehm, M. Grydlik, F. Hackl, I. Bergmair, M. Mhlberger, T. Fromherz, F. Schäffler, and G. Bauer. *Appl. Phys. Lett.*, 98:143101, 2011.

[103] C. Dais, G. Mussler, H. Sigg, E. Müller, H.H. Solak, and D. Grützmacher. *J. Appl. Phys.*, 105:122405, 2009.

[104] F. Hackl, M. Grydlik, M. Brehm, H. Groiss, F. Schäffler, T. Fromherz, and G. Bauer. *Nanotechnology*, 22:165302, 2011.

[105] J.B. Renucci, M.A. Renucci, and M. Cardona. *Light Scattering in Solids*. Flammarion Sciences, 1971.

[106] W.J. Brya. *Solid State Commun.*, 12:253, 1973.

[107] J.C. Tsang, P.M. Mooney, F. Dacol, and J.O. Chu. *J. Appl. Phys.*, 75:8098, 1994.

[108] M. Franz, K.F. Dombrowski, H. Rucker, B. Dietrich, K. Pressel, A. Barz, U. Kerat, P. Dold, and K.W. Benz. *Phys. Rev. B.*, 59:10614, 1999.

[109] F. Pezzoli. *Raman Spectroscopy of SiGe micro and nanostructures*. PhD thesis, Universit degli Studi di Milano - Bicocca, A.Y. 2006-2007.

[110] J. Menendez, A. Pinczuk, J. Bevk, and J.P. Mannaerts. *J. Vac. Sci. Technol. B*, 6:1306, 1988.

[111] D.J. Lockwood and J-M. Baribeau. *Phys. Rev. B*, 45:8565, 1992.

[112] M.I. Alonso and K. Winer. *Phys. Rev. B*, 39:10056, 1989.

[113] F. Pezzoli, E. Bonera, E. Grilli, M. Guzzi, S. Sanguinetti, D. Chrastina, G. Isella, H. von Kaenel, E. Wintersberger, J. Stangl, and G. Bauer. *Mat. Sci. Semicond. Proc.*, 11:279, 2008.

[114] H. Rucker and M. Methfessel. *Phys. Rev. B*, 52:11059, 1995.

[115] S. Ganesan, A.A. Maradudin, and J. Oitmaa. *Ann. Phys.*, 56:556, 1970.

[116] F. Cerdeira, C.J. Buchenau, M. Cardona, and F.H. Pollak. *Phys. Rev. B*, 5:580, 1972.

[117] I. De Wolf, H.E. Maes, and S.K. Jones. *J. Appl. Phys.*, 79:7148, 1996.

[118] M. Stoehr, D. Aubel, S. Juillaguet, J.L. Bischoff, L. Kubler, D. Bolmont, F. Hamdani, B. Fraisse, and R. Fourcade. *Phys. Rev. B*, 53:6923, 1996.

[119] L.H. Wong, C.C. Wong, J.P. Liu abd D.K. Sohn, L. Chan, L.C Hsia, H. Zang, Z.H. Ni, and Z.X. Shen. *Jap. Journ. Appl. Phys.*, 44:7922, 2005.

[120] J.S. Reparaz, A. Bernardi, A.R. Go ni, P.D. Lacharmoise, M.I. Alonso, M. Garriga, J. Novak, and I. Vavra. *Appl. Phys. Lett.*, 91:081914, 2007.

[121] J.S. Reparaz, A. Bernardi, A.R. Go ni, M.I. Alonso, and M. Garriga. *Appl. Phys. Lett.*, 92:081909, 2008.

[122] J.S. Reparaz, A.R. Go ni, A. Bernardi, M.I. Alonso, and M. Garriga. *Phys. Status Solidi B*, 246:548, 2009.

[123] F. Pezzoli, E. Grilli, M. Guzzi, S. Sanguinetti, D. Chrastina, G. Isella, H. von Kaenel, E. Wintersberger, J. Stangl, and G. Bauer. *Mat. Sci. Semicond. Proc.*, 9:541, 2006.

[124] M. Cazayous, J. Groenen, F. Demangeot, R. Sirvin, M. Caumont, T. Remmele, M. Albrecht, S. Christiansen, M. Becker, H. P. Strunk, and H. Wawra. *J. Appl. Phys.*, 91:6772, 2002.

[125] P.H. Tan, K. Brunner, D. Bougeard, and G. Abstreiter. *Phys. Rev. B*, 68:125302, 2003.

[126] P.H. Tan, D. Bougeard, G. Abstreiter, and K. Brunner. *J. Appl. Phys.*, 98:113517, 2005.

[127] M.I. Alonso, M. de la Calle, J.O. Oss, M. Garriga, and A.R. Go ni. *Phys. Rev. B*, 39:10056, 1989.

[128] A.V. Baranov, A.V. Fedorov, T.S. Perova, R.A. Moore, V. Yam, D. Bouchier, V. Le Thanh, and K. Berwick. *Phys. Rev. B*, 73:075322, 2006.

[129] V.A. Volodin, M.D. Efremov, A.I. Yakimov, G.Y. Mikhalev, A.I. Nikiforov, and A.V. Dvurechenskij. *Semiconductors*, 41:930, 2007.

[130] J. S. Reparaz, A. Bernardi, A. R. Go ni, M.I. Alonso, and M. Garriga. *Phys. Status Solidi B*, 246:482, 2009.

[131] A.V. Kolobov. *J. Appl. Phys.*, 87:2926, 2000.

[132] R. Loudon. *Adv. Phys.*, 13:423, 1964.

[133] E. Anastassakis, A. Pinczuk, E. Burnstein, F. H. Pollak, and M. Cardona. *Solid State Comun.*, 8:133, 1970.

[134] E. Anastassakis, A. Cantarero, and M. Cardona. *Phys. Rev. B*, 41:7529, 1990.

[135] M. Cardona and G. Günterodt, editors. *Light Scattering in Solids II*. Springer-Verlag, 1982.

[136] J.B. Renucci, R.N. Tyte, and M. Cardona. *Phys. Rev. B*, 11:3885, 1975.

[137] F. Cerdeira, W. Dreybrodt, and M. Cardona. *Solid State Comm.*, 10:591, 1971.

[138] J.B. Renucci, M.A. Renucci, and M. Cardona. *Solid State Comm.*, 9:1235, 1971.

[139] F. Cerdeira, M.I. Alonso, D. Niles, M. Garriga, and M. Cardona. *Phys. Rev. B*, 40:1361, 1989.

[140] C. Rosenblad, H.R. Deller, T. Graf, E. Müller, and H. von Känel. *J. Crystal Growth*, 188:125, 1998.

[141] C. Rosenblad, T. Graf, J. Stangl, Y. Zhuang, G. Bauer, J. Schulze, and H. von Känel. *Thin Solid Films*, 336:89, 1998.

[142] M. Kummer, C. Rosenblad, A. Dommann, T. Hackbarth, G. Höck, M. Zeuner, E. Müller, and H. von Känel. *Mat. Sci. Eng. B*, 89:288, 2002.

[143] T. Damen, S.P.S. Porto, and B. Tell. *Phys. Rev.*, 142:570, 1966.

[144] C. Pickering and R.T. Carline. *J. Appl. Phys.*, 75:4642, 1994.

[145] G.E. Jellison, T.E. Haynes, and H.H. Burke. *Optical Materials*, 2:105, 1993.

[146] E.D. Palik, editor. *Handbook of Optical Constants of Solids II*, volume 7. Academic Press, 1998.

[147] E.D. Palik, editor. *Handbook of Optical Constants of Solids III*, volume 7. Academic Press, 1998.

[148] A. Pinczuk and E. Burstein. *Surf. Sci.*, 37:153, 1973.

[149] D.D. Sell and E.O. Kane. *Phys. Rev.*, 185:1103, 1969.

[150] Z. Zhong and G. Bauer. *Appl. Phys. Lett.*, 84:1922, 2004.

[151] A.V. Baranov, A.V. Fedorov, T.S. Perova, R.A. Moore, S. Solosin, V. Yam, D. Bouchier, and V. Le Thanh. *J. Appl. Phys.*, 96:2857, 2004.

[152] C.L. Lawson and R.J. Hanson. *Solving Least Squares Problems*. Classics in Applied Mathematics. SIAM, 1995.

[153] A. Rastelli, M. Stoffel, A. Malachias, T. Merdzhanova G. Katsaros, K. Kern, T.H. Metzger, and O.G. Schmidt. *Nano Lett.*, 8:1404, 2008.

[154] G. Gouadec and P. Colomban. *Progress in Crystal Growth and Characterization of Materials*, 53:1, 2007.